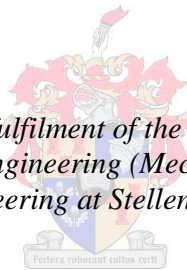


Evaluation of the performance characteristics of a hybrid (dry/wet) induced draft dephlegmator

by
Neil Raymond Anderson

*Thesis presented in partial fulfilment of the requirements for the degree
of Master of Engineering (Mechanical) in the
Faculty of Engineering at Stellenbosch University*



Supervisor: Prof. Hanno Carl Rudolf Reuter

December 2014

Declaration

By submitting this thesis electronically, I declare that the entirety of the work contained therein is my own, original work, that I am the sole author thereof (save to the extent explicitly otherwise stated), that reproduction and publication thereof by Stellenbosch University will not infringe any third party rights and that I have not previously in its entirety or in part submitted it for obtaining any qualification.

Date:

Copyright © 2014 Stellenbosch University

All rights reserved

Abstract

A novel induced draft hybrid (dry/wet) dephlegmator (HDWD) is introduced which can enhance the performance of dry air-cooled condenser systems and a model is developed to simulate its performance. The HDWD consists of two stages of cooling with the steam flow in series and the air flow in parallel through both stages. The first stage consists of downwardly inclined finned tube bundles, similar to conventional air-cooled condenser bundles, and the second stage comprises horizontal bare tube bundles of which the outer surface can selectively be operated dry or wet by spraying it with deluge water. A comparison of the HDWD with other existing and new concepts reveals the significant advantages that this technology has over other technologies. This thesis is a continuation of the work done by Heyns (2008), who introduced a forced draft HDWD and investigated its performance, and Owen (2013), who conducted a parametric investigation on the induced draft HDWD to improve the basic design proposed by Heyns (2008). In his thermo-flow model, Heyns (2008) conducted a thermal analysis assuming equal air flow through both stages and a constant vapor temperature inside the bundles, while Owen (2013) solved the thermal, steam-side pressure drop and draft equations. Both their models make use of empirical correlations by Gaddis & Gnielinski (1985), Zukauskas (1987), Mizushina et al. (1967) and Niitsu et al. (1967) for the performance characteristics. The current model solves the thermal, steam-side pressure drop and draft equations of the HDWD with better accuracy in the steam-side pressure drop calculation. The air-side heat and mass transfer and loss coefficient correlations found in literature were found to deviate significantly from each other resulting in uncertainty regarding their suitability. Based on the recommendations by Owen (2013), a bare tube test bundle with 19 mm outer diameter tubes arranged with a triangular pitch of 38 mm is therefore designed, manufactured and tested to investigate the performance characteristics of the bundle experimentally under dry and wet operating conditions to evaluate the correlations from literature. The experimental data confirmed the applicability of the correlations of Gaddis & Gnielinski (1985) and Zukauskas (1987) to predict the dry HDWD performance, since they deviated by 7% and 5% respectively from the experimental data in the applicable range. The heat transfer during wet operation is slightly over estimated within 5% with the correlations of Mizushina et al. (1967) in the range of application. The air-side pressure drop during wet operation is underestimated by 29 to 39% by Niitsu et al. (1967) and the correlation obtained from the experimental results is therefore used in the current model. Using the current HDWD model indicates significant performance enhancement using tubes with a smaller diameter in the delugeable bundle compared to the larger tubes of Heyns (2008) and agrees very well with the model of Owen (2013).

Opsomming

‘n Hibriede geïnduseerde trek deflegmator is voorgestel wat die werksverrigting van huidige lugverkoelde kondenserstelsels kan verbeter en ‘n model is ontwikkel wat die werksverrigting simuleer. Die deflegmator bestaan uit twee stadiums van verkoeling met die stoomvloei in serie en die lugvloei in parallel deur beide stadia. Die eerste stadium bestaan uit skuins, afwaartse finbuisbundels, soortgelyk aan konvensionele lugverkoelde kondenser-finbuisbundels, en die tweede stadium bestaan uit horisontale kaalbuisbundels waarvan die buite-oppervlak selektief droog of nat bedryf kan word deur dit met verkoelingswater te benat. ‘n Vergelyking tussen die deflegmator en ander huidige en nuwe konsepte toon merkbare voordele wat die tegnologie bo die ander tegnologieë het. Die tesis is ‘n voortsetting van die werk van Heyns (2008), wie ‘n hibriede geforseerde trek deflegmator voorgestel en die werksverrigting daarvan ondersoek het, en Owen (2013) wat ‘n parametriese studie op die hibriede geïnduseerde trek deflegmator gedoen het om die basiese ontwerp voorgestel deur Heyns (2008) te verbeter. In sy termovloei-model, het Heyns (2008) die termiese analise ondersoek met die aanname van gelyke hoeveelhede lugvloei deur beide stadia met ‘n konstante damp-temperatuur binne die bundels, terwyl Owen (2013) die termiese, stoomkant-drukval and trekvergelings opgelos het. Beide hul modelle maak van die empiriese korrelasies van Gaddis & Gnielinski (1985), Zukauskas (1987), Mizushina et al. (1967) en Niitsu et al. (1967) gebruik vir die werkverrigtingskarakteristieke. Die huidige model los die termiese, die stoomkant-drukval asook die trekvergelings van die deflegmator op met verbeterde akkuraatheid van die stoomkant-drukval berekeninge. Die lugkant warmte- en massaoordrag en verlieskoëffisiënt korrelasies wyk baie van mekaar af wat lei tot onsekerhede rakende hul toepasbaarheid. Gebaseer op die voorstelle van Owen (2013) is ‘n kaalbuisbundel met 19 mm buite-diameter buise met ‘n driehoekige steek van 38 mm dus ontwerp, vervaardig en getoets om die werksverrigtingskarakteristieke van die bundel eksperimenteel te ondersoek onder droë en nat toestande om die korrelasies van die literatuur te evalueer. Die eksperimentele data bevestig die toepaslikheid van die korrelasies van Gaddis & Gnielinski (1985) en Zukauskas (1987) om die droë werksverrigting van die deflegmator te voorspel, aangesien hul met 7% en 5% onderskeidelik afwyk van die eksperimentele data in die toepaslike bestek. Die warmteoordrag tydens natwerking is ietwat oorskot binne 5% met die korrelasies van Mizushina et al. (1967) in die bestek van toepassing. Die lugkant-drukval tydens natwerking is onderskat met 29 tot 39% deur Niitsu et al. (1967) en die korrelasie verkry vanaf die eksperimentele resultate is dus gebruik in die huidige model. Deur gebruik te maak van die huidige model van die deflegmator dui merkbare werksverrigting verbetering aan deur van buise met ‘n kleiner diameter in die benatbare bundel te gebruik in vergelyking met die groter buise van Heyns (2008) en stem baie goed ooreen met die model van Owen (2013).

Acknowledgements

I would like to thank the following people for their valuable input and support:

- Prof. Reuter for his continued assistance, patience and guidance.
- ESKOM for the opportunity to enrich and empower myself through higher education.
- EPRI for the funding of the project.
- Mr. CJ Zietsman and his team, especially Juliun Stanfliet for the assistance with the assembly of the tube bundle and installation. All their jokes made the days shorter.
- Neil Fourie for keeping things interesting in the office and his advice and willingness to bounce off ideas.
- Alain Michaels and Jacques du Plessis for their assistance with calibration and testing when more than two hands were necessary.
- My family in particular my parents Ronnie and Tersia Anderson, and friends for their love and support.
- My heavenly Father for His guidance and who has a plan for my life.

Contents

List of tables.....	viii
List of figures.....	ix
Nomenclature.....	xii
1 Introduction	1
1.1 Background	1
1.2 Induced draft hybrid (dry-/wet-) dephlegmator concept.....	5
1.3 Other types of hybrid cooling systems.....	8
1.4 Motivation	11
1.5 Objectives and scope.....	12
1.6 Thesis outline	13
2 Literature study.....	14
2.1 Introduction	14
2.2 Operation of the tube bundle in evaporative mode	14
2.3 Operation of the tube bundle in dry convective mode	19
2.4 Conclusion.....	20
3 Theoretical analysis	23
3.1 Introduction	23
3.2 Tube bundle operated as an evaporative cooler	23
3.2.1 Derivation of the governing equations.....	23
3.2.2 Integral governing equations	28
3.2.3 Evaluation of the heat and mass transfer coefficients from experimental data.....	29
3.2.4 Performance evaluation of the deluged tube bundle.....	31
3.3 Tube bundle operated as a dry air-cooled heat exchanger	32
3.3.1 Derivation of the governing equations.....	32
3.3.2 Integral governing equations	33
3.3.3 Evaluation of the air-side heat transfer coefficient from experimental data	33
3.3.4 Performance evaluation of the convectively cooled dry tube bundle..	34
4 Experimental evaluation of the tube bundle performance.....	37
4.1 Introduction	37

4.2	Description of the experimental apparatus.....	37
4.2.1	Wind tunnel.....	37
4.2.2	Counter-flow test section	38
4.2.3	Tube bundle specifications	39
4.3	Measurement techniques	41
4.3.1	Temperature	41
4.3.2	Pressure	43
4.3.3	Flow rate	44
4.4	Test procedure	45
4.5	Data acquisition and processing.....	46
5	Results and discussions	47
5.1	Introduction	47
5.2	Water distribution and collecting trough system performance characteristics.....	47
5.2.1	Trough pressure drop characteristics for dry operation	47
5.2.2	Spray and trough system transfer and trough pressure drop characteristics for wet operation.....	48
5.3	Tube bundle performance characteristics for wet operation	50
5.3.1	Operating strategy and parameter ranges.....	50
5.3.2	Sensitivity of the transfer characteristics to the mean deluge water temperature	53
5.3.3	Correlation predictions of performance	56
5.3.4	Transfer characteristics from the experimental results	58
5.4	Tube bundle performance characteristics for dry operation	64
5.4.1	Bundle heat transfer characteristics	64
5.4.2	Bundle pressure drop characteristics	67
6	Performance study of the hybrid dephlegmator	70
7	Conclusion.....	80
8	References	81
Appendix A: Correlations for heat and mass transfer and air-side pressure drop.....		A-1
A.1 Dry operation of the tube bundle.....		A-1
A.1.1 Heat transfer correlations.....		A-1
A.1.2 Pressure drop correlations.....		A-1

A.2	Wet operation of the tube bundle.....	A-2
A.2.1	Film heat and mass transfer coefficients.....	A-2
A.2.2	Pressure drop correlations.....	A-3
Appendix B:	Induced draft HDWD model.....	B-1
B.1	Evaluation of the thermal performance of the HDWD with wet operation of the second stage bundles.....	B-1
B.1.1	The first stage (finned tube) section.....	B-1
B.1.2	The second stage (bare tube) section.....	B-7
B.2	Evaluation of the draft equation for the dephlegmator system.....	B-12
B.2.1	The first stage (finned tube) section.....	B-13
B.2.2	The second stage (bare tube) section.....	B-14
B.2.3	The mixed section.....	B-17
B.3	The steam side pressure drop.....	B-19
B.3.1	The first stage (finned tube) section.....	B-19
B.3.2	The second stage (bare tube) section.....	B-24
B.4	Evaluation of the thermal performance of the HDWD with dry operation of the second stage bundles.....	B-30
B.4.1	Thermal analysis of the section stage (bare tube) section.....	B-30
B.4.2	Evaluation of the draft equation for the second stage (bare tube) section.....	B-34
Appendix C:	Calibration.....	C-1
C.1	Thermocouples.....	C-1
C.2	Pressure transducers.....	C-4
C.3	Venturi flow meter.....	C-5
C.4	Process water flow meter.....	C-9

List of tables

Table 2.1: Summary of the bundle characteristics and analysis techniques of various authors	15
Table 5.1: Operating ranges for all the parameters during the wet tests	51
Table 5.2: Wet thermal test 1 order	52
Table 5.3: Wet thermal test 2 order	52
Table 5.4: Wet thermal test 3 order	52
Table 5.5: Operating ranges for all the parameters during the dry thermal tests...	65
Table B.1: Converged static pressures and temperatures for the vapor of tube row 2	B-24
Table B.2: Converged vapor temperature and static pressure at various points in the second stage tube bundle	B-29
Table B.3: Summary of the important parameters for the second stage tube bundle under wet operation	B-30
Table B.4: Converged static pressures and temperatures of the vapor of tube row 1 and 2	B-36
Table B.5: Converged vapor temperatures and static pressures at various points in the second stage tube bundle	B-36
Table B.6: Summary of the important parameters for the second stage tube bundle under dry operation	B-37
Table C.1: Error of the thermocouples with regard to the reference thermocouple prior to calibration	C-1
Table C.2: Six points selected with the readings from the reference and ordinary thermocouples	C-2
Table C.3: The error between the calibrated thermocouple temperatures and the reference thermocouple temperature	C-4

List of figures

Figure 1.1: Schematic of an air-cooled condenser system.....	2
Figure 1.2: Air-cooled condenser street incorporating a conventional dephlegmator (Heyns, 2008).....	2
Figure 1.3: Conventional dephlegmator unit	3
Figure 1.4: First generation of a hybrid dephlegmator (Heyns, 2008)	3
Figure 1.5: Proposed concept of the induced draft HDWD.....	5
Figure 1.6: Delugeable second stage tube bundle layout.....	6
Figure 1.7: Thermosyphon cooler of Johnson Control	8
Figure 1.8: A variation of a dry/wet Heller system	9
Figure 1.9: The Holtec HI-VACC system	10
Figure 1.10: SPX ClearSky® water recovery system (Source: SPX Cooling).....	10
Figure 1.11: Schematic of the Evapco Dual Coil Cooler	11
Figure 2.1: Comparison of the film heat transfer coefficient between three authors	21
Figure 2.2: Comparison of the mass transfer coefficient between three authors...	22
Figure 3.1: Control volume of an evaporative cooler	24
Figure 3.2: Resistance diagram of the control volume for wet operation.....	26
Figure 3.3: Resistance diagram of the control volume for wet operation with the replaced resistance	28
Figure 3.4: Procedure flow chart to determine the wet tube bundle performance.	32
Figure 3.5: Resistance diagram of the control volume for dry operation	33
Figure 3.6: Procedure flow chart to determine the dry tube bundle performance.	35
Figure 4.1: Wind tunnel	37
Figure 4.2: Counter-flow test section (point 7 in Fig. 5.1)	38
Figure 4.3: Test bundle tube layout	40
Figure 4.4: Photo of the tube bundle.....	40
Figure 4.5: Psychrometer	41
Figure 4.6: Thermocouple placement to measure the deluge water film temperature across the height of the tube bundle	42
Figure 4.7: Schematic of the placement of the receptacle for the deluge water thermocouples.....	42
Figure 4.8: Photo of the receptacle for the deluge water thermocouples	43
Figure 4.9: Pressure transducers	43
Figure 4.10: H-tap and H-tap in the experimental setup.....	44
Figure 4.11: Installed Venturi flow meter	44
Figure 4.12: Process water flow meter	45
Figure 4.13: Screen-shot of the data logging software developed in Excel	46
Figure 5.1: Air-side pressure drop over the collecting troughs for dry operation .	47
Figure 5.2: Merkel number of the system without a bundle installed	48
Figure 5.3: Loss coefficient of the collecting troughs without the bundle installed	49
Figure 5.4: Pressure drop over the collecting troughs during wet operation.....	50
Figure 5.5: Energy balances of the tests of the deluge evaporative cooler.....	52

Figure 5.6: The influence of deluge water temperature on the mass and film heat transfer coefficient	54
Figure 5.7: Measured vertical deluge water temperature profiles over the height of the tube bundle with first measuring technique	55
Figure 5.8: Measured vertical deluge water temperature profiles over the height of the tube bundle with second measuring technique	55
Figure 5.9: Deviations between predicted thermal performance using performance characteristics from literature and measured performance for different air- and deluge water flow rates	56
Figure 5.10: Converged mean deluge water temperature obtained from Effectiveness-NTU method and measured mean deluge water temperature	57
Figure 5.11: The influence of deluge water temperature on the bundle performance characteristics	59
Figure 5.12: Mass transfer coefficient as a function of the critical air mass velocity through the bundle	60
Figure 5.13: Deluge film convective heat transfer coefficient as a function of the critical air mass velocity through the bundle	60
Figure 5.14: The heat transfer prediction with the Effectiveness-NTU method by using the obtained correlations for the mass and film heat transfer coefficients...	61
Figure 5.15: Mass transfer coefficient comparison between the current study and Mizushina et al. (1967)	62
Figure 5.16: Film heat transfer coefficient comparison between the current study and Mizushina et al. (1967)	63
Figure 5.17: Air-side loss coefficient for the deluged tube bundle	63
Figure 5.18: Two phase air-side pressure drop over the tube bundle	64
Figure 5.19: Energy balances of the dry thermal tests of the tube bundle.....	65
Figure 5.20: Air-side Nusselt number for dry operation	66
Figure 5.21: Characteristic heat transfer parameter during dry tests	67
Figure 5.22: Dry tube bundle isothermal loss coefficient.....	68
Figure 5.23: Air-side pressure drop over the tube bundle in cross flow.....	68
Figure 5.24: Dry tube bundle thermal loss coefficient based on the mean approach velocity.....	69
Figure 6.1: Induced draft HDWD with numbered locations	70
Figure 6.2: Psychrometric chart with the properties of air at the numbered locations indicated	71
Figure 6.3: Dry operation heat rejection comparison	72
Figure 6.4: Wet operation heat rejection comparison.....	72
Figure 6.5: Dry operation heat rejection comparison for different vapor temperatures.....	73
Figure 6.6: Wet operation heat rejection performance for different vapor temperatures.....	74
Figure 6.7: The effect of deluge water flow rate variation on the performance of the dephlegmator.....	75
Figure 6.8: Comparison of the dry versus wet operation performance at the reference deluge water flow rate.....	75

Figure 6.9: Fan power consumption for dry and wet operation.....	76
Figure 6.10: Dry operation fan power consumption comparison for different vapor temperatures.....	77
Figure 6.11: Wet operation fan power consumption comparison for different vapor temperatures.....	77
Figure 6.12: The predicted evaporation rate at different deluge water flow rates.	78
Figure 6.13: The predicted evaporation rate at different vapor temperatures	79
Figure 6.14: A comparison of the predicted evaporation rates of the three models used.....	79
Figure B.1: Schematic of the dephlegmator with numbered locations for the sample calculation.....	B-1
Figure B.2: Dephlegmator with the flow resistances indicated for the draft equation.....	B-12
Figure B.3: First stage steam-side pressure drop.....	B-20
Figure B.4: Second stage steam-side pressure drop	B-25
Figure C.1: Photo of the calibration of the thermocouples.....	C-1
Figure C.2: The curve fits for four thermocouples	C-3
Figure C.3: Betz micromanometer.....	C-4
Figure C.4: Plots of the calibration curves for the three pressure transducers in Figure 4.9.....	C-5
Figure C.5: Venturi calibration setup	C-6
Figure C.6: Pressure transducer calibration.....	C-7
Figure C.7: Experimental and calculated deluge water flow rate comparison	C-8
Figure C.8: Calibration results of the process water flow meter	C-9

Nomenclature

A	Area	$[\text{m}^2]$
a_i	Interfacial area	$[\text{m}^{-1}]$
B	Breadth	$[\text{m}]$
C_d	Discharge coefficient	
c_p	Specific heat at constant pressure	$[\text{J/kgK}]$
c_v	Specific heat at constant volume	$[\text{J/kgK}]$
d	Diameter	$[\text{m}]$
e	Effectiveness	
F_T	Correction factor	
f	Friction factor	
G	Mass velocity	$[\text{kg/m}^2\text{s}]$
g	Gravitational acceleration	$[\text{m/s}^2]$
H	Height	$[\text{m}]$
h	Convective heat transfer coefficient	$[\text{W/m}^2\text{K}]$
h_d	Mass transfer coefficient	$[\text{kg/m}^2\text{s}]$
i	Enthalpy	$[\text{J/kg}]$
I	Current	$[\text{A}]$
i_{fg}	Latent heat	$[\text{J/kg}]$
K	Coefficient of pressure drop	
k	Thermal conductivity	$[\text{W/mK}]$
L	Length	$[\text{m}]$
m	Mass flow rate	$[\text{kg/s}]$
n	Quantity	
Ny	Characteristic heat transfer parameter, $hA/(kA_{fr}Pr^{0.333})$	$[\text{m}^{-1}]$

P	Pitch	[m]
Q	Heat transfer rate	[W]
Ry	Characteristic flow parameter, $\rho v/\mu$	[m ⁻¹]
T	Temperature	[K] or [°C]
U	Overall heat transfer coefficient	[W/m ² K]
u	Internal energy	[J/kg]
V	Volumetric flow rate or voltage	[m ³ /s] or [V]
v	Velocity	[m/s]
W	Width	[m]
w	Humidity ratio	[kg H ₂ O/kg dry air]
x	Co-ordinate or distance	[m]
Y	Approach velocity factor	
y	Co-ordinate or distance	[m]
z	Co-ordinate or distance	[m]

Greek symbols

α	Kinetic energy correction factor	
Δ	Differential	
ϵ	Surface roughness	
η	Efficiency	
θ	Apex angle of the A-frame	
Γ_m	Deluge water flow rate per unit length	[kg/ms]
μ	Dynamic viscosity	[kg/ms]
ρ	Density	[kg/m ³]
σ	Contraction ratio	
ϕ	Expansion factor or relative humidity	

Dimensionless groups

a	Geometric relation, P_t/d_o
b	Geometric relation, P_l/d_o
K	Loss coefficient, $2\Delta p_{tot}/\rho v^2$
Le_f	Lewis factor, $h_a/c_{pma}h_d$
NTU	Number of transfer units
Nu	Nusselt number, hd/k
Pr	Prandtl number, $\mu c_p/k$
Re	Reynolds number, $\rho v d/\mu$

Subscripts

a	Dry air or based on air side area
av	Mixture of dry air and water vapor
b	Bundle
c	Casing, critical, convection or calibrated
$corr$	Correlation
cv	Control volume
D	Diameter
d	Dynamic or diagonal
db	Dry bulb
de	Drift eliminator
dif	Diffuser
dw	Deluge water
e	Effective
$evap$	Evaporated
ex	Experiment

<i>f</i>	Film, fin, fan or friction
<i>fr</i>	Frontal
<i>g</i>	Gravity
<i>h</i>	Hydraulic or hub
<i>i</i>	Inlet, interface, inside or counter
<i>iso</i>	Isothermal
<i>ke</i>	Kinetic energy
<i>l</i>	Longitudinal
<i>lm</i>	Logarithmic mean
<i>m</i>	Mean, mass, momentum or mixture
<i>min</i>	Minimum
<i>n</i>	Nozzle
<i>o</i>	Outlet or outside
<i>p</i>	Pass
<i>r</i>	Root or row
<i>rec</i>	Recovery
<i>s</i>	Saturation, steam, steel or sump
<i>sz</i>	Spray zone
<i>t</i>	Transversal or tube or total
<i>tb</i>	Tube bundle
<i>tr</i>	Tube row or trough
<i>ts</i>	Tower supports
<i>tus</i>	Wind tunnel upstream section
<i>v</i>	Vapor or static (pressure)
<i>w</i>	Water, wall or wet
<i>wb</i>	Wet bulb

x	Co-ordinate
y	Co-ordinate
z	Co-ordinate

1 Introduction

1.1 Background

Different types of cooling systems exist to reject waste heat from power plants to the environment, which include dry-, wet-, dry-/wet-, wet-/dry- and hybrid cooling systems. Higher cycle efficiencies are obtainable with wet-cooling systems making them traditionally the preferred choice in power generation applications, when water costs are low and/or primary energy prices are high. These systems are bounded by the ambient wet-bulb temperature as they utilize direct contact evaporative cooling of the cooling water for heat rejection, making low turbine backpressures possible. The wet-bulb temperature is lower and generally much more stable than the dry-bulb temperature. The main disadvantage of wet-cooling systems is the high water consumption, which has been addressed by different authors who developed models to determine the optimal wet-cooling tower sizing (Söylemez, 2001; Panjeshahi et al., 2009).

Due to rising cooling water cost, dwindling water supplies and power plants with steam turbines being located in arid regions, air-cooled steam condensers (ACC's) are increasingly being used to reject heat to the environment. The performance of these systems is primarily dependent on their relative size and the ambient conditions. With an increase in the ambient temperature, the steam turbine exhaust pressure increases resulting in a reduction in power plant output and/or efficiency and thus revenues. The size of the ACC is therefore determined by the maximum allowable turbine back pressure at adverse ambient conditions and not optimal ambient conditions, which generally results in higher capital costs. (Wilber & Zammit, 2005)

Figure 1.1 shows the schematic of a direct dry ACC system connected directly to the steam turbine exhaust where the ACC consists of a number of parallel streets as depicted in Figure 1.2. The exhaust steam exits the low pressure (LP) turbine and is fed via a steam duct to the ACC where it enters the primary condensers at the top. The residual steam that exits the primary condensers is condensed in reflux condenser units also known as dephlegmators. The condensate from all the streets is drained by gravity and collected in the condensate tank from where it is pumped back to the boiler after passing through the regenerative feedwater heaters. Another function of the dephlegmator is to extract the non-condensable gases from the system and to vent them to the atmosphere. The dephlegmator is installed in series downstream on the steam-side of the primary condensers (Figure 1.2).

The conventional dephlegmator in Figure 1.2 is shown in more detail in Figure 1.3. The residual steam from the primary condensers and non-condensable gases enter at the bottom of the finned tube bundles and flow counter-current to the condensate flowing downward under gravity. The non-condensable gases and

residual steam are extracted at the top of the bundle by an ejector. Non-condensable gases are found in the water/steam cycle because of air dissolved in the make-up water entering the water/steam cycle to replenish boiler blowdown losses and due to air leaks into the ACC since it operates under vacuum.

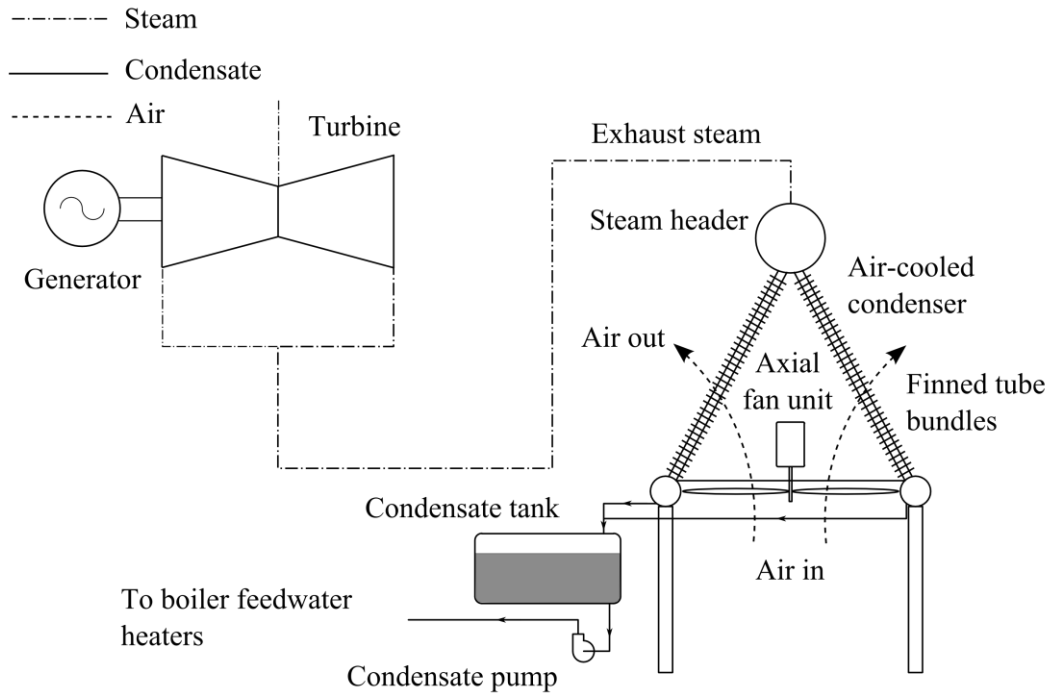


Figure 1.1: Schematic of an air-cooled condenser system

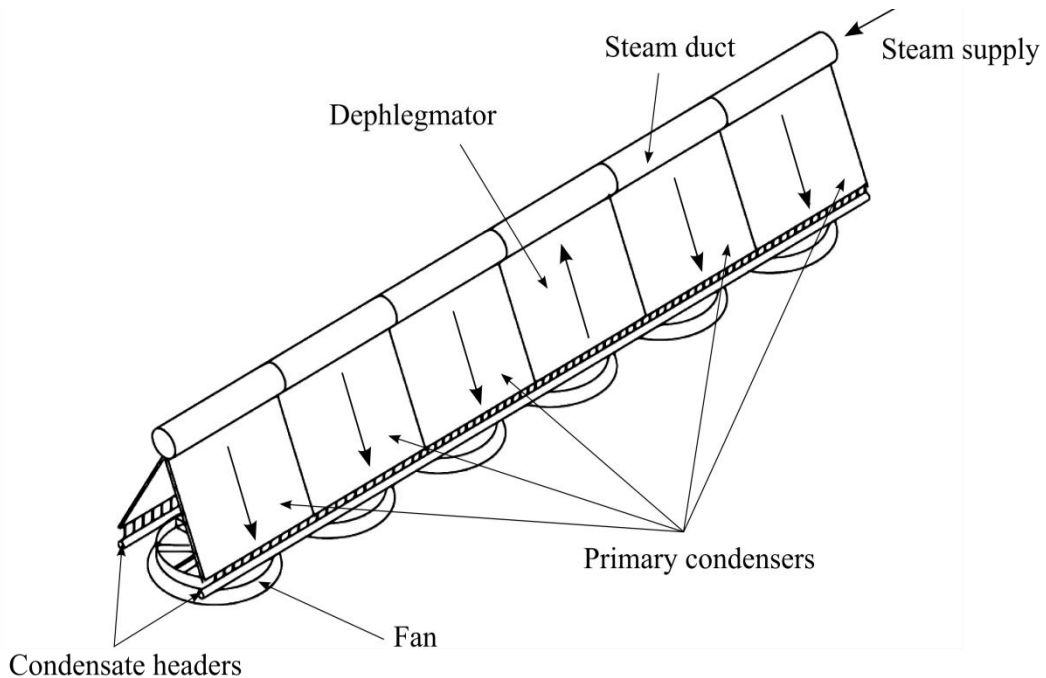


Figure 1.2: Air-cooled condenser street incorporating a conventional dephlegmator (Heyns, 2008)

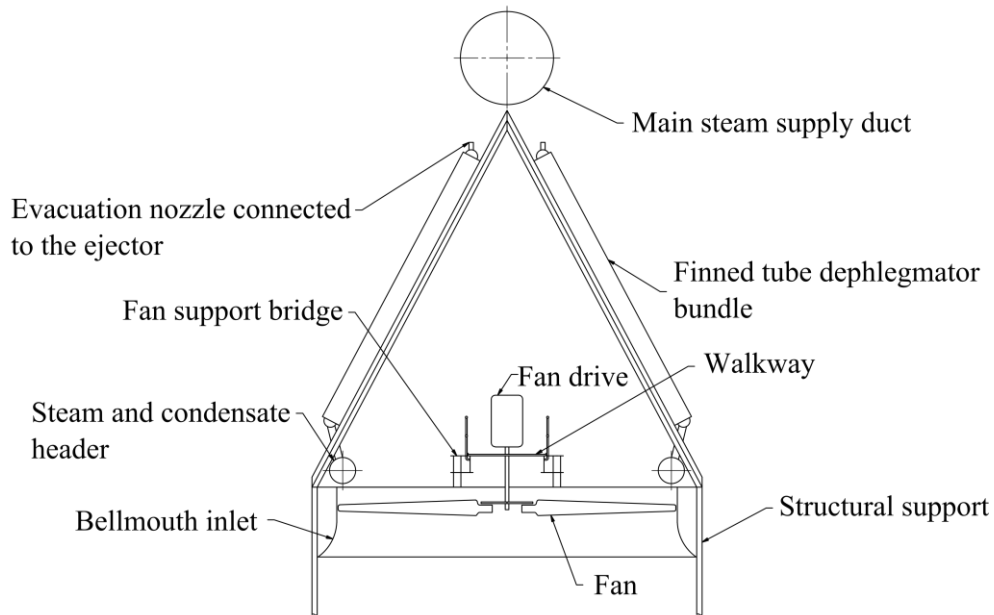


Figure 1.3: Conventional dephlegmator unit

Figure 1.4 depicts the hybrid dry-/wet- dephlegmator (HDWD) design proposed by Heyns (2008). He developed a model to calculate the performance of an ACC incorporating a HDWD. This model does not take steam-side pressure drop into account and there is uncertainty about the air-side pressure drop. Steam-side flooding has also not been evaluated. The air-side heat and mass transfer characteristics of the deluged bare tube heat exchanger bundle were verified experimentally. It was found that the hybrid operation improved the overall performance of an air-cooled condenser by reducing the exhaust pressure of the turbine and thus increasing the power output. A measureable increase in the cooling performance at high ambient temperatures was found.

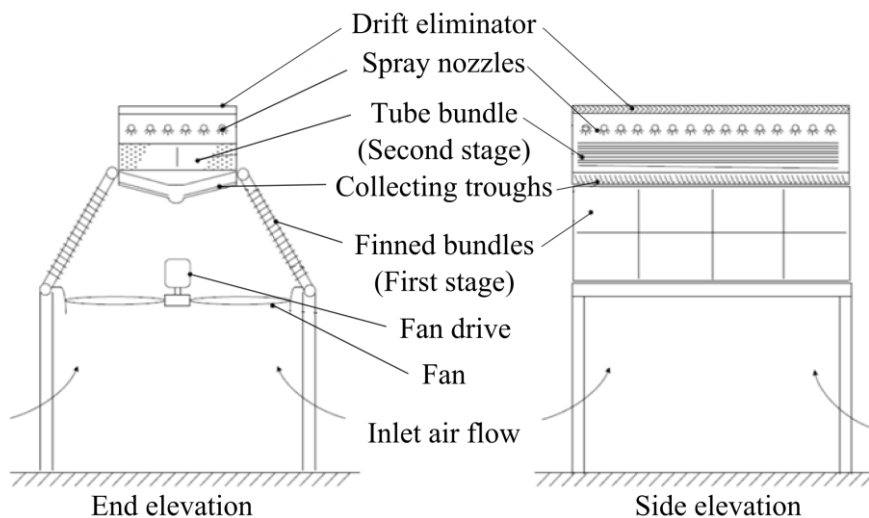


Figure 1.4: First generation of a hybrid dephlegmator (Heyns, 2008)

The configuration has the same inlet header design, fan arrangement and plot plan area as current conventional A-frame forced draft dephlegmator units. The concept consists of two stages of cooling with the steam-side connected in series. The first stage consists of finned tube bundles, similar to those found in current air-cooled condenser applications but are shorter in length. It is inclined upward at 60° to the horizontal with one or multiple tube rows. This stage has direct dry cooling operation with convection heat transfer.

The second stage comprises of corrosion resistant bare tube bundles which are connected to the outlet ends of the first stage finned bundles. The first stage consists of eight finned tube bundles, while the second stage only consists of two bare tube bundles. Each bare tube bundle of the second stage has 10.8 meter long tubes which is also the width of the dephlegmator unit in this case.

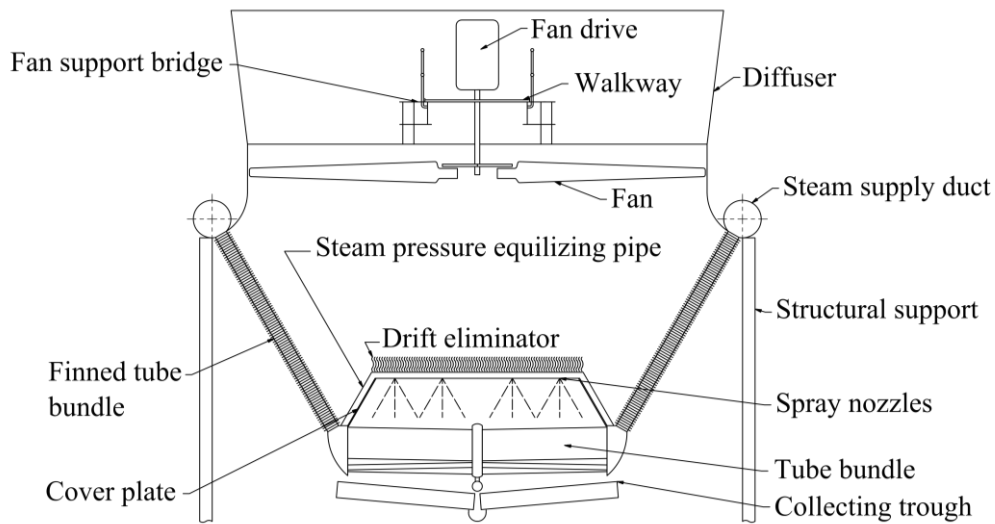
The outer surface of the second stage tube bundle can be operated dry as an air-cooled condenser or wet as an evaporative condenser for performance enhancement. Due to the utilization of the latent heat of water through evaporation, deluging of the tubes result in significant increase in the performance compared with convective heat transfer in dry operation. This enhances the performance of the HDWD and the whole ACC system during periods of high ambient temperatures while using much less water than an all wet system. The HDWD's water usage is also less compared to adiabatic pre-cooling of inlet air of all the units in a street using water sprays and does not have similar fouling and corrosion problems, but still yields similar performance enhancement (Heyns, 2008).

The deluge water is circulated by a pump and sprayed through spray nozzles located above the tube bundles during wet operation. The excess deluge water is collected in collecting troughs located below the tube bundle. The excess deluge water is kept in a storage tank and the evaporation losses are replenished with make-up water. Drift eliminators are located above the spray nozzles to inhibit the loss of the entrained water droplets. A fan is installed in the dephlegmator at the same height as the rest of the fans of the condenser street and blows air through the first and second stage simultaneously and in parallel to minimize the air-side pressure drop and to keep the initial temperature difference high for both stages.

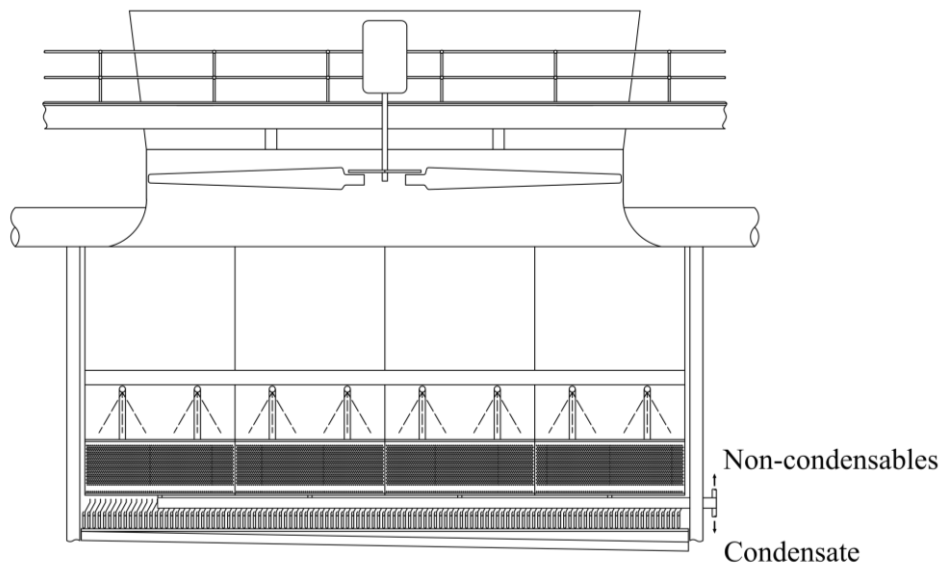
In the first stage bundles, the condensate drains in counterflow with the inlet steam and non-condensable gases. When the second stage bare tube bundle is operated in deluged or wet mode, the higher steam and condensate flow entering and exiting the dephlegmator respectively can cause flooding in the first stage finned tube bundles. The finned tubes should therefore be properly dimensioned to prevent flooding, which blocks the tubes with water resulting in reduced thermal performance due to increased thermal resistance and higher steam-side pressure drop. Another problem with flooding is freezing which may cause the tubes to rupture. The long tubes of the second stage also increase the steam-side pressure drop.

1.2 Induced draft hybrid (dry-/wet-) dephlegmator concept

An alternative induced draft hybrid (dry-/wet-) dephlegmator is proposed as illustrated in Figure 1.5 that addresses the high steam-side pressure drop and flooding found with the previous concept. The induced draft dephlegmator consists of two cooling stages with the steam-side connected in series similar to the concept of Heyns (2008), but each stage has eight bundles with four on each side.



(a) Frontal view



(b) Sectioned side view

Figure 1.5: Proposed concept of the induced draft HDWD

The first stage finned tube bundles are inclined downward at 60° instead of upwards with the horizontal to enable co-current flow of condensate and steam inside the tubes. This eliminates flooding associated with counterflow of steam and condensate. The second stage tube bundle is also located at the outlet end of the finned tube bundle section and can be selectively operated in either dry or wet (deluged) modes.

Spray nozzles, drift eliminators, collecting troughs and a deluge water storage tank are also found in this concept and serve the same purpose as discussed previously. Moreover, the structural support of the drift eliminators and the spray nozzles also serves as a pressure equalizing pipe to ensure similar steam pressures in each of the second stage tube bundles. The dephlegmator fan is installed at the same height as the fans of the other primary condenser units in a street and sucks air through the first and second stage bundles simultaneously. Visible plume abatement is achieved during wet operation by mixing of the moist air from the second stage tube bundles with the hot dry air from the first stage finned tube bundles.

The second stage tube bundle, as presented in Figure 1.6, consists of three passes with twenty tube rows in the first pass, four tube rows in the second pass and one tube row in the final pass. The 19 mm outer diameter tubes are 2.5 m in length in a triangular pitch layout with the transverse pitch equal to two times the outer diameter of the tubes. The tubes are therefore in a staggered arrangement, which yields greater heat transfer than inline tube banks (Khan et al., 2006).

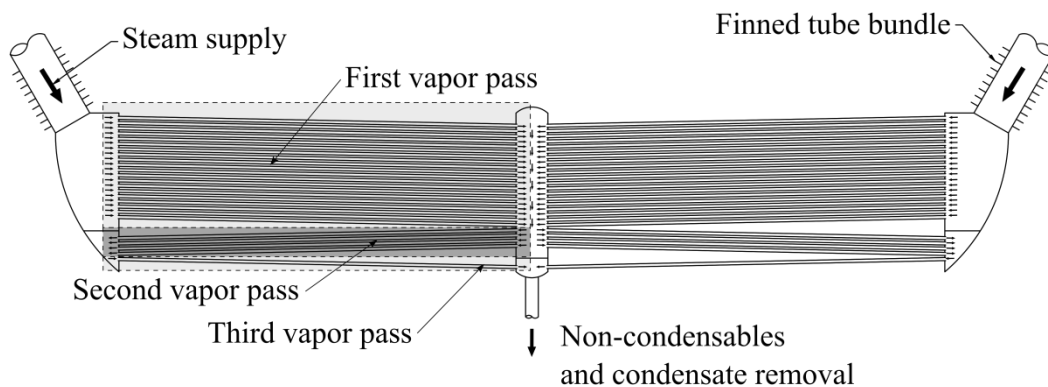


Figure 1.6: Delugeable second stage tube bundle layout

Owen & Kröger (2013) analyzed various configurations of the second stage tube bundles to improve the performance of the bundle of Heyns (2008). A three vapor pass configuration with only a single tube row in the final pass yields the lowest ejector loading by accumulating and concentrating the non-condensable gases towards the outlet end of the final pass. In addition, the tube diameter and the number of tube rows of the second stage tube bundle have respectively been decreased and increased from the bundle of Heyns (2008). This is to increase the

heat transfer area and heat transfer potential, but at the expense of a greater steam-side pressure drop and water consumption. (Owen & Kröger, 2013)

The ejector loading is lowest for this current configuration, because of no row effects such as backflow present in the final pass. Backflow occurs typically in single-pass multi-row systems where all the tubes of the particular pass share common headers and complete condensation occurs in one or multiple tubes. This result in a high steam-side pressure drop for those particular tubes and the steam flow in the adjacent tubes must increase to equalize the pressure. The additional steam flow in the adjacent tubes, not experiencing complete condensation, flows back into the tubes of complete condensation. This creates stagnant zones where non-condensable gases can accumulate. The air-side upstream tubes are more prone to backflow due to the greater temperature difference between the air and the steam (Owen, 2013).

The steam condensing in the final pass consisting of only one tube row ensures a net outflow of steam in the pass before it. To determine the amount of tubes in the second pass, the vapor mass flow exiting the second vapor pass is taken as the same as the vapor condensing in the final pass for ideal operation. The amount of tube rows in the second vapor pass is dictated by the heat transfer of the particular pass that will avoid full condensation. A number of tube rows should be selected without full condensation occurring in any tube row of the vapor pass. The same principle holds in determining the amount of tubes between the first and the second vapor pass. Under actual operating conditions vapor will exit the final pass of the HDWD due to the location of the operating ejector there.

The tubes are slightly inclined at 1° downward to aid in condensate drainage yielding a 50 mm drop over the 2500 mm tube. The condensate is drained by gravity at the outlet end of the finned tube bundle section and at the end of each pass of the second stage tube bundle section. Extracting and mixing the condensate from various points in the HDWD will reduce sub-cooling of the condensate. The low vapor velocities and the short tube lengths keep the steam-side pressure drop low.

Non-condensables are generally denser than the vapor in the ACC system and will naturally want to sink to the lowest point. This makes the non-condensable extraction point at the bottom of the HDWD a better choice compared with the location of the extraction point of conventional dephlegmators (Figure 1.3). Effective evacuation of non-condensable gases reduces the likelihood of condensate sub-cooling which increases the absorption of oxygen with associated increased corrosion. Regenerative heating is needed to heat up the sub-cooled condensate and is best avoided. Without the effective removal of non-condensables from the system, reduced heat transfer, corrosion and even freezing of the condensate at low ambient conditions can be consequences. Condensate freezing can even lead to tube failures but can be avoided by controlling the fan speed.

Finned tube bundles have a bigger risk of corrosion and scaling of the outer surface compared with the bare tube bundles of the deluge system. The use of finned tube bundles also increases the air-side pressure drop and the likelihood of drift losses. Bare tube bundles can be rinsed regularly to minimize fouling. Finlay & Harris (1984) report that keeping the deluge water below 50 °C keeps the fouling soft to be washed off as soon as it forms. Fouling can also be further reduced by keeping the deluge water flow rate high and uniform over the entire tube bank. Deluge water flooding in the bundles should be avoided because as the deluge water is held up in the tube bank, the temperature increases which increases the likelihood of scale deposition. Bare tubes are therefore used for the second stage bundle.

1.3 Other types of hybrid cooling systems

Hybrid cooling systems which consist of both dry and wet components are receiving increased attention as the demand for electricity increases which is in conflict with the protection and conservation of water resources. Five of the latest technologies are described in a recent EPRI report compiled by Maulbetsch & DiFilippo (2012) detailing these concepts.

The first dry/wet cooler is under development by Johnson Controls and consists of a Thermosyphon cooler in series with a wet cooling tower as illustrated in Figure 1.7. The thermosyphon cooler can be sized to take a fraction or the total circulating cooling water (CCW) flow rate. This enables the Thermosyphon cooler to take a fraction or the total heat load.

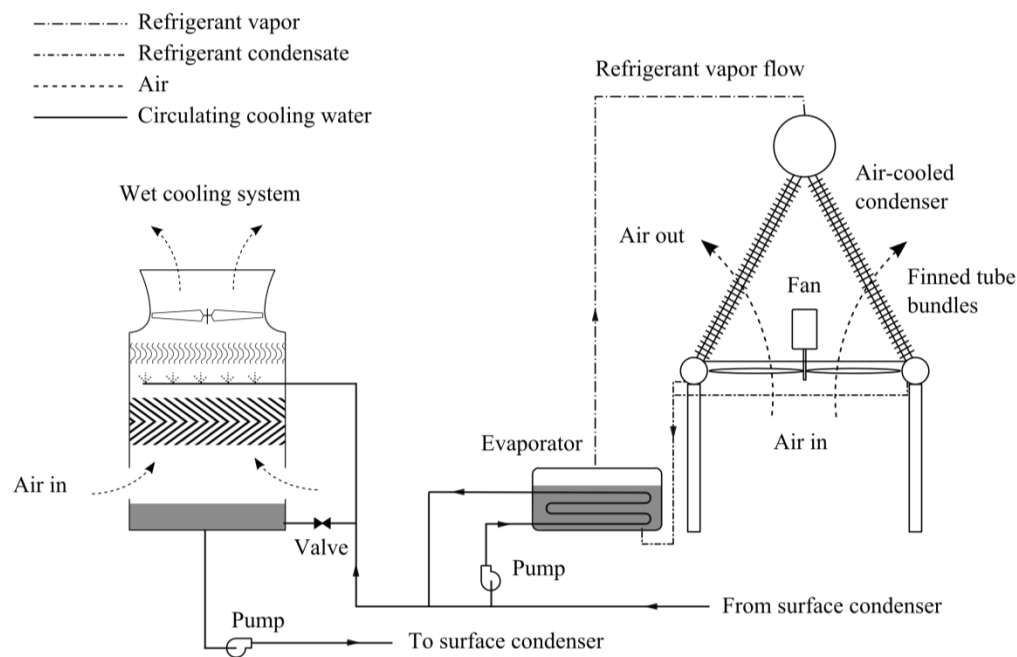


Figure 1.7: Thermosyphon cooler of Johnson Control

The pre-cooled circulating cooling water reduces the load on the wet cooling tower which reduces the evaporation losses. The Thermosyphon cooler consists of a shell and tube heat exchanger as the evaporator, located below an air-cooled condenser with a refrigerant as the working fluid in a secondary circuit. The vapor from the evaporator rises to the air-cooled condenser, condenses and the condensate subsequently flows back down to the evaporator by gravity. With the proper sizing of the two elements in series, water savings of up to 50% are possible but at the expense of increased auxiliary power consumption due to the condenser fans.

A basic Heller system is an indirect natural draft air-cooled condenser system with a direct spray condenser and a recovery turbine to power the pump for the water circulation. Various variations of this system exist which include spray or deluge enhancement of the air-cooled heat exchanger elements using mechanical draft dry cooling towers and pairing of the wet and dry cooling elements in series or parallel. One such variation is depicted in Figure 1.8 with the dry and wet cooling system in parallel and the use of a spray and surface condenser. With these various variations Maulbetsch & DiFilippo (2012) established that water savings of 10 to 90% are possible compared with wet cooling systems.

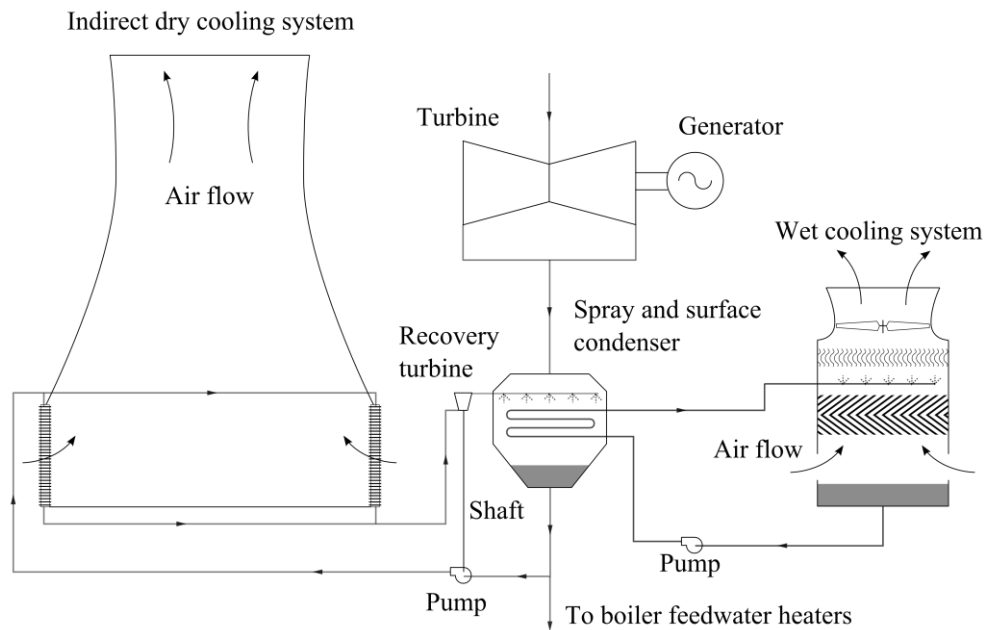


Figure 1.8: A variation of a dry/wet Heller system

Maulbetsch & DiFilippo (2012) reports on another concept developed by Holtec International. The HI-VACC system depicted in Figure 1.9 is an air-cooled condenser system that consists of finned vertical tubes made of stainless steel instead of galvanized steel to eliminate corrosion problems. The angle between the radial fins is 22.5° resulting in 16 fins per tube that run along the whole length of the tube. One fan unit, similar to a conventional air-cooled condenser module, consists of a fan below 24 by 24 vertical tubes that forces air over the complete

length of the finned tubes. Compared with conventional A-frame air-cooled condenser systems, the HI-VACC system uses 3% more fan power, costs 4% more but occupies 30% less space. The system can be enhanced with spray cooling making the condenser smaller with less likelihood of corrosion problems.

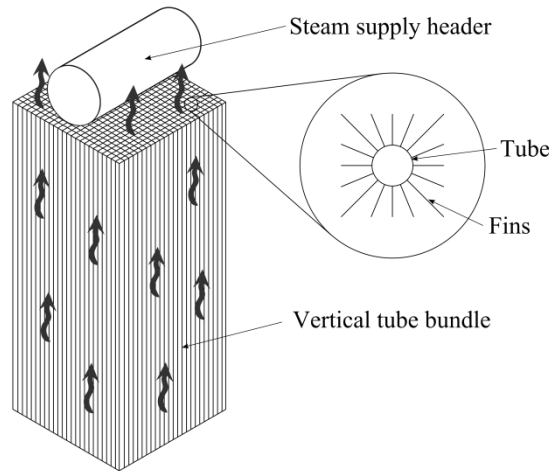
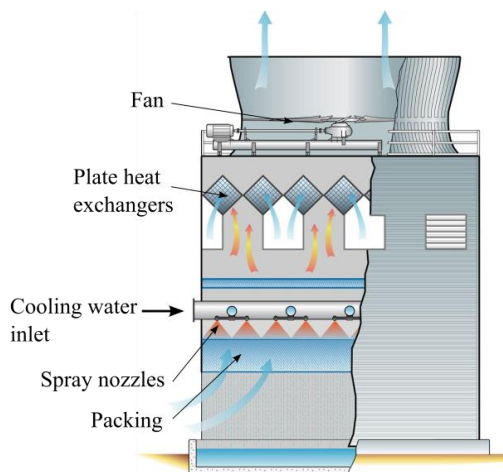
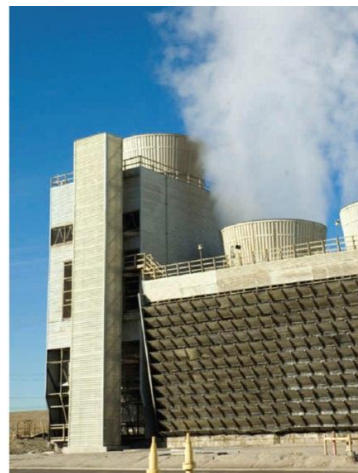


Figure 1.9: The Holtec HI-VACC system

SPX cooling technologies developed ClearSky® to enable some water recovery in all wet systems. As illustrated in Figure 1.10 the system is an all wet cooling system that uses ambient air together with plate heat exchangers to condense some moisture out of the hot saturated outlet air from a wet cooling tower. Plate heat exchangers are located just below the fan and ambient air (indicated with blue arrows) is sucked in at the same height. Condensed water is returned to the cooling loop or can be utilized elsewhere on the plant. Maulbetsch & DiFilippo (2012) report that 15 to 30% water recovery is possible depending on the ambient conditions. Plume abatement is an added bonus but at the cost of 50% higher fan power consumption. The whole system is 2.5 to 3 times more expensive compared to a conventional mechanical draft counterflow wet cooling tower.



(a) Schematic representation



(b) Photo of a pilot plant

Figure 1.10: SPX ClearSky® water recovery system (Source: SPX Cooling)

Evapco developed a Dual-coil cooler depicted in Figure 1.11 of which both or either coils can be operated dry or wet. The two coils are multi-pass finned tube bundles and are connected in series (outlet 1 connected to inlet 2) while the air flows through both in parallel. Widely spaced elliptical tubes are used in the finned tube bundles for high performance and low air-side pressure drop. The spray nozzles used to wet the tubes are located above the bundles and the run-off water is collected in a collection basin. The deluge water and air are in a counterflow arrangement. The drift eliminators are installed above the spray nozzles to prevent air-borne droplet carry-over. The upstream or first stage of cooling is always dry when only one stage is wetted. Maulbetsch & DiFilippo (2012) concludes that the Dual-coil cooler yielded significant reduction in pump power consumption and a 67% reduction in water consumption when compared with a similar size evaporative cooler with similar fan power consumption.

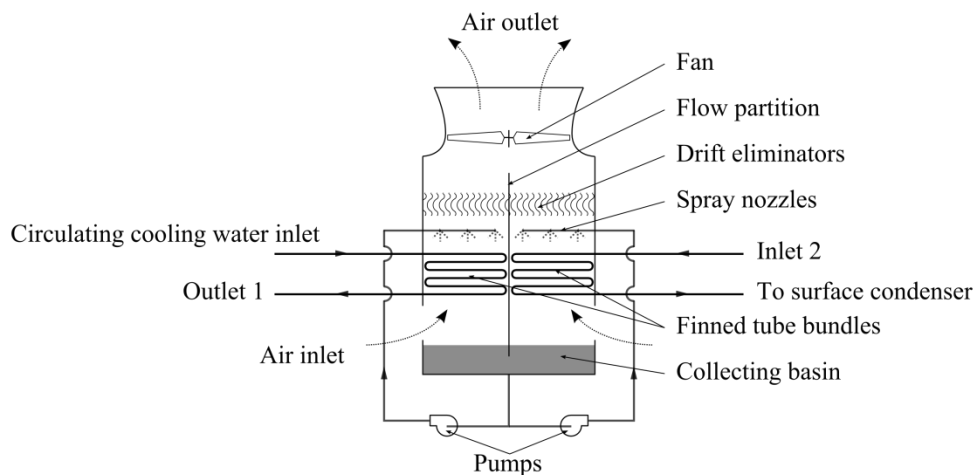


Figure 1.11: Schematic of the Evapco Dual Coil Cooler

Other coolers are also under development that has two finned tube bundles in series on top of one another. The air flows in series through both and enters below the bottom finned tube bundle. The bottom finned tube bundle can be selectively operated dry or wet with the collection basin for the deluge water found at the bottom of the cooler.

1.4 Motivation

Other concepts to save water and improve plant performance compared with an all dry system are available such as those discussed in the previous section. However, all these systems consist of both the wet and dry cooling equipment and are more expensive than the conventional dry or wet cooling systems. The SPX Clearsky® wet cooling system for instance, is 2.5 to 3 times more expensive than a conventional mechanical draft wet cooling tower and the Holtec HI-VACC cooling system cost is reported to be 4% higher than the conventional dry cooling system. In addition, Heyns (2008) investigated adiabatic spray cooling of inlet air

to enhance the cooling capacity of the direct dry cooling systems but found practical issues such as unevaporated droplets accumulating on the finned surfaces of the condensers, undesirable rainback of this water and ground water contamination. These problems will be similar when considering the Holtec HI-VACC spray cooling system. The reported water savings of the SPX Clearsky® wet cooling system is also highly dependent on ambient conditions.

The novel hybrid (dry/wet) induced draft dephlegmator concept deserves further attention, since performance enhancement of dry cooling systems is possible by using only a fraction of the water consumed by all wet cooling systems. For the optimal performance versus operational cost, it is advised that the second stage tube bundle is only operated in wet evaporative mode during high ambient temperatures, windy conditions or both, or in periods of peak demand to reduce the pressure on the grid and avoid the necessity of employing peaking power stations in the power generation portfolio. At lower ambient conditions the second stage bundle is operated dry as an air-cooled condenser. With this operating strategy, the annual operating cost of this system is lower than a dry system with a separate wet system. The plant is able to run more efficiently during hotter periods with increased revenues. The hybrid dephlegmator is only slightly more expensive compared with a conventional dephlegmator and is a practical and cost effective modification to plants utilizing existing air-cooled condenser systems.

1.5 Objectives and scope

The evaluation of the new induced draft HDWD with a delugeable tube bundle is proposed in this research and is a continuation of the research done by Heyns (2008) and Owen (2013). However, the performance characteristics such as the air-side pressure drop and mass- and heat transfer characteristics of the second stage tube bundle are unknown along with the effect of the steam-side pressure drop.

The model of Heyns (2008) does not take flooding and the steam-side pressure drop into account and does not solve a draft equation to determine the air flow distribution through the two stages of cooling. Owen (2013) solved the thermal analysis and a draft equation but used a conservative model to determine the steam-side pressure drop through the induced draft HDWD. The heat and mass transfer correlations of Mizushima et al. (1967) and the steam-side pressure drop of Niitsu et al (1967) are used in these two models. The objectives of this study are therefore:

- a. Design and manufacture of the tube bundle that represents the second stage bare tube bundles of the dephlegmator
- b. Modification of an existing test facility.
- c. Installation of the test bundle into the test facility.
- d. Performance testing of the test bundle to determine the dry and wet performance characteristics for different air - and deluge water flow rates

- e. Verify the applicability of the correlations of Mizushina et al. (1967) and Niitsu et al. (1967) to predict the performance of the second stage tube bundle
- f. Incorporate applicable bundle performance characteristics in a HDWD model to evaluate the performance and the optimal operational parameters. The operational parameters include the water and energy consumption. The HDWD model must include the thermal analysis, draft equations and steam-side pressure drop.

1.6 Thesis outline

Chapter 1 supplies background on cooling systems, describes how air-cooled condensers and dephlegmators work and various dephlegmator designs are discussed. The need for the current research is highlighted in the motivation, the scope is defined in the research objectives and the thesis outline is provided.

A literature review on the performance characteristics of the tube bundle of the dephlegmator is presented in Chapter 2. This includes the search for correlations for the performance of the tube bundle under dry and wet operation and the air-side pressure drop in both cases. Methods of analysis are also studied.

Chapter 3 presents the derivation of the governing equations, the evaluation of the heat and mass transfer coefficients from the experimental results and the performance evaluation of the tube bundle under dry and wet operation. Chapter 4 supplies a brief description of the experimental facilities, together with measuring techniques, test procedures and a description of the program used to monitor the data obtained from the experiments.

The results obtained from the experiments are conveyed in Chapter 5 along with the sought after performance characteristics of the tube bundle. The obtained performance characteristics are implemented in the dephlegmator model yielding the dephlegmator performance and operational parameters as detailed in objective (f) and documented in Chapter 6. The thesis results are summarized with concluding remarks in Chapter 7.

Supplementary material includes an index of all the correlations found for the performance characteristics of a bare tube bundle under dry and wet operation in Appendix A, a complete sample calculation of the performance of the induced draft HDWD in Appendix B, and a summary of the calibration procedures and results in Appendix C.

2 Literature study

2.1 Introduction

This section details the previous work done by other authors to obtain the transfer characteristics of tube banks under dry and wet operation. The methods of analysis are scrutinized and the main findings summarized. All the correlations of the authors are summarized in Appendix A.

2.2 Operation of the tube bundle in evaporative mode

Table 2.1 summarizes the bundle geometries and analysis techniques of some authors who did important experimental work on evaporative coolers or verified the work of others.

Pioneering work in the field of evaporative coolers were conducted by Parker & Treybal (1961) and the bundle tested is summarized in Table 2.1. The governing equations were numerically integrated in their analysis for their evaporative cooler tests. It is confirmed that the deluge water temperature cannot stay constant as the air passes through the tube bundle. It is assumed the saturated enthalpy of the air at the deluge water temperature is a linear function of the deluge water temperature over the small temperature range found within the tube bundle. For the mass transfer coefficient it was customary to use the data from dry heat transfer across tube banks and use the heat and mass transfer analogy to calculate the performance but that yielded unsatisfactory results. The mass transfer from the air-water interface was calculated on the enthalpy difference of the air at the interface and the air stream. A Lewis factor of unity was assumed as well as negligible evaporation losses. These assumptions are known as the Merkel (1925) assumptions.

Niitsu et al. (1967) published useful deluge water film heat transfer coefficients, mass transfer coefficients and pressure drop correlations for bare and finned tube evaporative coolers. They found the mass transfer coefficient is dependent only on the deluge water flow rate above the critical value of $\Gamma_m/d_o = 0.7 \text{ kg/m}^2\text{s}$ and recommends a minimum deluge water flow rate of $\Gamma_m/d_o = 0.8 \text{ kg/m}^2\text{s}$ for uniform wetting of bare tube bundles.

Mizushina et al. (1967) in addition to the bundle geometry summarized in Table 2.1, conducted tests on two other evaporative coolers with tube outer diameters of 12.7 and 40 mm. In the tests the deluge water and air flow rates were varied and the process water flow rate kept constant. It was found satisfactory to assume the deluge water temperature in the cooler constant and the arithmetic average of the deluge water temperatures were taken as the constant temperature for the analysis of the transfer coefficients. A Lewis relation of unity was applied and therefore the enthalpy driving force can be used to calculate the mass transfer coefficient.

The deluge water film convective heat transfer coefficient was calculated with a logarithmic temperature. The spray zone cooling was found negligible.

Table 2.1: Summary of the bundle characteristics and analysis techniques of various authors

	Mizushina et al. (1967)	Niitsu et al. (1967)	Parker & Treybal (1961)	Finlay & Harris (1984)	Hasan & Sirén (2002)	Papaefthimiou et al. (2012)
Inner tube diameter, d_i [m]	0.01605		0.0158	0.0150		0.015
Outer tube diameter, d_o [m]	0.01905	0.016	0.019	0.0191	0.012	0.019
Number of tube rows, n_r	12		10	16	12	16
Number of tubes per row, n_{tr}	6		6	31	19	31
Tube length, L_t [m]	0.5			0.913	1.2	0.913
Transverse pitch, P_t	0.0381	0.0375	0.038	0.0285	0.02	0.0285
Longitudinal pitch, P_l		0.0381			0.06	
Tube layout	Triangular		Triangular	Triangular	Staggered	Triangular
Analysis method	ϵ -NTU		Numerical integration	Numerical integration	Numerical integration	Numerical integration

Mizushina et al. (1968) did performance tests on evaporative coolers and presents an iterative design method with the process water cooling range, process water flow rate and inlet air conditions as inputs. The analysis entails integrating the temperature gradients of the three fluids in the evaporative cooler. In accordance with Parker & Treybal (1961), the design method assumes the enthalpy of the deluge water to be a linear function of deluge water temperature over a certain applicable range. The model neglects the thermal resistance of the conduction through the tube and the evaporative losses. In their analysis it is clear that the

mean deluge water temperature is bound by the saturated outlet air temperature and the process water outlet temperature.

Tezuka et al. (1977) conducted extensive tests on evaporative coolers of different configurations by varying the inlet process water temperature, the process water-, air-, and deluge water flow rates. The mass transfer coefficient increased with an increase in all the flow rates independently and decreased with an increase in process water inlet temperature. The pressure loss over the tube bundle is a strong function of the air flow rate and a weak function of the deluge water flow rate. The size of the current bundle does not fall in the range of those tested in the published correlations.

The conventional counter-flow and co-current evaporative cooler were investigated by Finlay & Harris (1984). They based their analysis on the assumption that the system may be solved in one dimension, evaporation losses are negligible and, similar to Parker & Treybal (1961) and Mizushina et al. (1968), assumed the enthalpy of air a linear function of temperature over the small temperature variation found in the deluge water temperature through the height of the heat exchanger. The governing equations were integrated over the height of the tube bundle. The analysis uses the film heat transfer coefficient of Parker & Treybal (1961), the mass transfer coefficient of Mizushina et al. (1967) and the convective heat transfer coefficient to air was calculated from the Lewis equation.

Erens & Dreyer (1993) compared the methods introduced by Poppe & Rögener (1984) in which the Lewis factor is calculated, and Merkel (1925), in which the Lewis factor is assumed to be unity with negligible evaporation loss and solved both methods with numerical integration. They found that the extra effort and computing time for the Poppe method did not justify the small increase in accuracy over the Merkel method. This iterative model converges when the in- and outlet deluge water temperatures converges. The conclusion drawn is that a constant deluge water temperature may be assumed together with the Merkel method of analysis, since the deluge water temperature varies little through the tube bundle. This enables the differential equations to be integrated and integral equations are solved for the performance analysis.

Zalewski & Gryglaszewski (1997) presented a complex mathematical analysis of an evaporative cooler and derived four differential equations to relate the change in air humidity, air-, deluge water- and process water temperature through the height of the tube bundle. The model takes the convective heat transfer coefficient of a film flowing over the tube into account and assumes a Lewis factor of 0.865. The model is based on the heat transfer area of the air-water interface and not the outer surface area of the tube bundle. The experimental apparatus had tubes with an outer diameter of 25 mm and arranged in a staggered pattern with $P_l = 52$ mm and $P_t = 50$ mm. The model correlated well with their experimental results.

The performance of an evaporative condenser was investigated by Ettouney et al. (2001) in which the evaporative condenser condensed process steam in counter-

flow wetted finned tubes. The effect of various ratios of water-to-air mass flow rates on the cooling performance of the condenser was investigated. It was found that the condenser effectiveness increases as the water-to-air mass flow rate ratio decreases and also if the inlet steam temperature increases. A comparison was made between the performance of the condenser in wet operation and dry as an air-cooled condenser. The effectiveness of the condenser in dry operation was found to be lower than wet operation. The evaporative condenser could handle a 60% higher thermal load compared to the air-cooled condenser.

Hasan & Sirén (2002) conducted experiments with an evaporative cooler to determine the transfer coefficients and present a model similar to the Poppe & Rögener (1984) method of analysis and employ the Merkel (1925) assumptions which are also defined in Erens & Dreyer (1993) and Kröger (2004). The model does not account for evaporation losses. The bundle geometry and method of analysis is summarized in Table 2.1. A mass transfer coefficient for the bundle is obtained by using the film heat transfer coefficient of Parker & Treybal (1961) and is supplied in Appendix A. The author claims that the mass transfer coefficient should be independent of the process water inlet temperature which is contradicted by Tezuka et al. (1977), as stated earlier.

In a follow up study, Hasan & Sirén (2003) investigated the performance increase of using finned tube evaporatively cooled bundles compared to plain tube bundles. The tubes had an outer tube diameter of 10 mm. A performance increase of 92 – 140% for air velocities from 1.66 – 3.57 m/s were noted for the finned tube compared to the plain tube bundles. The authors utilized the Effectiveness-NTU method for the analysis of the plain tube bundle and used the measured and stabilized inlet deluge water temperature as the mean deluge water temperature, contrary to the arithmetic mean deluge water temperature used by Mizushina et al. (1967) and Heyns (2008). Merkel's assumptions were employed in the analysis. Large amount of scatter of the deluge water film convective heat transfer coefficient was attributed to sensitivity to the deluge water temperature. The authors found a dependency of the mass transfer coefficient on the inlet process water temperature and the film convective heat transfer coefficient on the air mass flow rate. A relation for the mass transfer coefficient was found but supplied as a function of the air mass flow rate with no applicable range, making it very bundle geometry specific; therefore, not quoted here. The inlet air wet-bulb temperature is theoretically the lowest temperature to which the process medium can be cooled. As expected they found the pressure drop over the bundle greater for the finned tubes compared to the plain tubes with a slight increase for wet operation in both cases.

Stabat & Marchio (2004) developed a simplified model to analyze the performance of evaporative coolers which is based on Merkel (1925). The model introduces two parameters, the air-side and water-side heat transfer coefficients which can be identified from manufacturers' catalogs. This model is advantageous when a comparison of the performance of evaporative coolers from different

suppliers over a range of operating conditions is desired. The model has been verified against data supplied by Baltimore Aircoil Company.

Sarker et al. (2008) investigated the performance characteristics of a hybrid closed circuit cooling tower with plain tubes. They reported that tube pitch, air inlet temperature and - velocity have a significant impact on the air-side pressure drop over the bundle. A finer tube pitch increases the pressure drop and the thermal performance. A coarser tube pitch yields a lower pressure drop with the disadvantage of higher initial material cost for a bigger bundle. The pressure drop seems to increase exponentially with an increase in air inlet velocity. The effect of the air inlet velocity on the cooling capacity was not investigated in this study. The author did not publish the pressure drop and transfer characteristic correlations but reported that the inlet wet-bulb temperature controls the deluge water temperature.

In addition, Sarker et al. (2009) looked at ways to improve the performance of the hybrid closed circuit cooling tower. Wet operation of the finned tubes yield 22% increase in cooling performance compared to wet operation of bare tubes while dry operation of the finned tubes yield 260% increase in cooling performance compared to dry bare tubes. However, the pressure drop over the finned tube bundle is nearly two times the pressure drop over the bundle of bare tubes.

The sensitivity of the thermal performance of an evaporative cooler to the inlet air conditions was investigated by Papaefthimiou et al. (2012). The bundle geometry is summarized in Table 2.1. The analysis entailed solving five governing equations of air dry-bulb-, deluge water- and process water temperature, air humidity and the deluge water mass flow rate through the height of the tube bundle. The film convective heat transfer coefficient was obtained from Parker & Treybal (1961) and the mass transfer coefficient from Mizushina et al. (1967) together with an assumed Lewis factor of unity but took the evaporation losses into account. The model results compared well with the experimental results obtained from Finlay & Harris (1984). The greatest heat transfer was observed at the lowest inlet wet-bulb temperature with the evaporation losses also being the highest.

The method of analysis of Poppe & Rögener (1984) as presented by Kröger (2004) was implemented by Zheng et al. (2012) to investigate the performance of an evaporative cooler with oval tubes under both unsaturated and supersaturated air conditions. The results from the governing equations were solved by discretization and were compared to experimental results from a previous study. Little difference was noted in heat transfer rate between the models based on unsaturated and supersaturated conditions. The heat and mass transfer coefficients were also found to be the same for supersaturated and unsaturated air. Supersaturation is likely to occur at lower inlet air temperature.

2.3 Operation of the tube bundle in dry convective mode

Along with the evaporative cooler tests, Parker & Treybal (1961) also did tests on a dry surface tube bundle to obtain the air-side convective heat transfer coefficient as documented in Appendix A with a Reynolds number range applicable to the current study. Zukauskas & Ulinskas (1983) collected pressure drop data from various sources and published various correlations for the loss coefficients over finned and plain tube bundles of inline and staggered arrangement. In addition, pressure drop corrections for smaller tube bundles, fluid property variation and yawed banks are published.

Zukauskas (1987) presented a thorough exposition of convective heat transfer in cross flow of single tubes and spheres, and smooth, rough and finned tube bundles. Details of the pressure drop over smooth, rough and finned tube bundles were also presented. The hydraulic drag or pressure drop over smooth and yawed bundles is explained by referring to fluid dynamic principles over a single tube row. The hydraulic drag comprises friction and pressure drag and the pressure drag for inner tube rows for a staggered arrangement are found to decrease from $1000 < Re < 1 \times 10^4$. The friction drag has a much smaller contribution in this range. The pressure drop over tube banks are not influenced by thermal conditions from $Re > 1000$. After examining the effect of yawed banks, the 1° slope of the tubes in the current bundle has a negligible effect on the heat transfer or pressure drop of the tube bundle. After various fluids with $1 < Pr < 10^4$ and $1 < Re < 2 \times 10^6$ were considered, a generic equation for the Nusselt number for tube banks in cross flow is suggested by Zukauskas (1987). The equation is applicable to subcritical flow ($Re < 2 \times 10^5$) and supercritical flows ($Re > 6 \times 10^5$).

A Prandtl number ratio is incorporated to account for heat flux direction. All thermo-physical properties are evaluated at the bulk mean temperature of the fluid and Pr_{avto} (the denominator) is evaluated at the mean outer tube wall temperature. A power of 0.25 is suggested for the ratio for low Prandtl number fluids such as gases for heat transfer from the wall to the fluid. It is reported in the subcritical flow regime for staggered arrangements that the heat transfer increases with a decrease in longitudinal pitch of the tubes and to a lesser extent with decreasing transverse pitch. In addition, the turbulence intensity of the air and the surface roughness of the tubes have an enhancing effect on the heat transfer. The surface roughness augments the heat transfer due to quicker onset of the critical flow regime but at the expense of higher pressure drop because of earlier turbulent boundary layer separation creating a bigger wake region behind the tube. However, these effects are only apparent at $Re > 1 \times 10^4$. The applicable Nusselt number correlation is supplied in Appendix A.

Gaddis & Gnielinski (1985) did a comprehensive study on the pressure drop over banks of tubes in cross flow and proposed a general equation which is applicable over a wide range of Reynolds numbers. They report that the coefficient of

pressure drop is a minimum at $Re_D \geq 2 \times 10^5$ and this value is dependent on the relative spacing and the relative roughness of the tubes presumably due to the displacement of the point of separation. Beyond the critical Reynolds number the coefficient of pressure drop approaches a constant value. However, this minimum value is highly dependent on the bundle geometry.

Khan et al. (2006) presented an analytical model for the analysis of heat transfer in tube banks and verified the model against other authors including Zukauskas & Ulinskas (1983). The model is based on an isothermal boundary condition for the tubes throughout the heat exchanger and a uniform velocity profile between the tubes. It was found that the model constantly overestimated the heat transfer obtained from experimental results.

2.4 Conclusion

It is common practice to numerically integrate the governing equations in order to obtain the transfer coefficients of the tube bundle as was done by Parker & Treybal (1961), Mizushina et al. (1968), Finlay & Harris (1984), Zalewski & Gryglaszewski (1997), Hasan & Sirén (2002), Papaefthimiou et al. (2012) and Zheng et al. (2012). This is referred to as the Poppe & Rögener (1984) method of analysis. Mizushina et al. (1967), Hasan & Sirén (2003) and Heyns (2008) used a constant deluge water temperature and based the analysis on the logarithmic temperature and enthalpy differences similar to the Effectiveness-NTU method. Mizushina et al. (1967) and Heyns (2008) used the arithmetic average of the deluge water temperatures throughout the height of the bundle as the constant deluge water temperature, while Hasan & Sirén (2003) used the stabilized in- and outlet deluge water temperatures. The Merkel (1925) assumptions were employed by Parker & Treybal (1961), Mizushina et al. (1967), Finlay & Harris (1984), Hasan & Sirén (2002), Hasan & Sirén (2003) and Stabat & Marchio (2004). Erens & Dreyer (1993) investigated the sensitivity of the results by analyzing on a constant deluge water temperature and employing the Merkel assumptions and secondly by numerically integrating the governing equations (Poppe analysis). They concluded that the rigorous Poppe method did not justify the loss in accuracy compared to the Merkel analysis with constant deluge water temperature. The assumption of saturated outlet air is deemed sufficient, since Zheng et al. (2012) proved the heat and mass transfer coefficients is the same for the saturated and supersaturated cases.

From this literature study it is determined that only Parker & Treybal (1961) and Mizushina et al. (1967) tested tube bundles with 19 mm tubes to obtain new transfer characteristics. Air-side pressure drop correlations are very scarce in literature and the only useful correlation is published by Niitsu et al. (1967). As mentioned earlier, the pressure drop correlation of Niitsu et al. (1967) and the heat and mass transfer correlations of Mizushina et al. (1967) were used in the dephlegmator models of Heyns (2008) and Owen (2013).

In addition to the pressure drop correlation, Niitsu et al. (1967) also published heat and mass transfer correlations and Figure 2.1 and 2.2 shows how these correlations and those of Parker & Treybal (1961) and Mizushina et al. (1967) deviate from each other over the selected flow rate range. This deviation between the correlations is a source of uncertainty in the applicability of these correlations; hence one of the objectives of this project is to conduct experiments on a representative tube bundle and to compare these correlations with the experimentally obtained results. In order to make the comparison as close as possible, the Effectiveness-NTU method is used in the current analysis based on the Merkel assumptions, as was done by Heyns (2008) and Owen (2013).

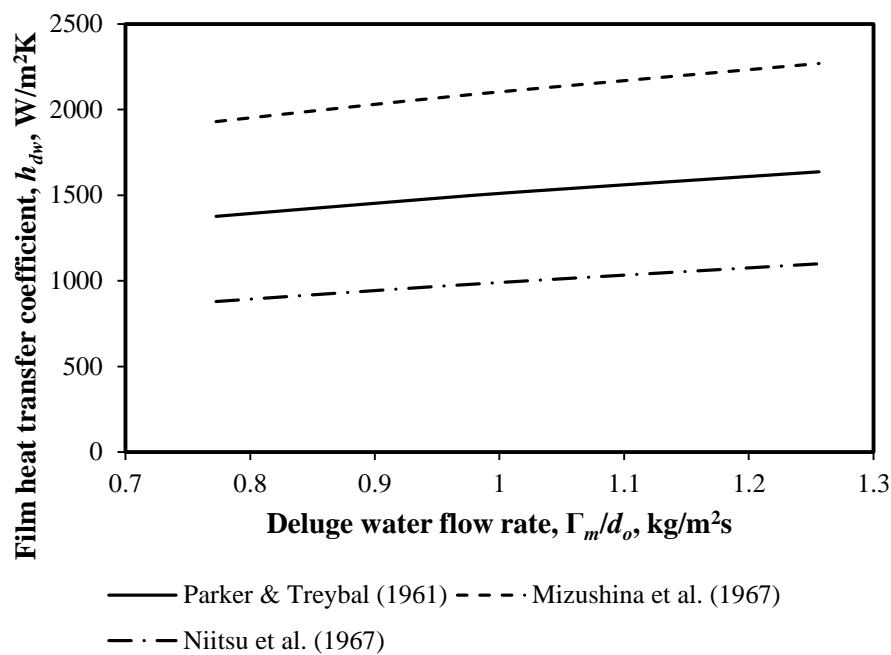


Figure 2.1: Comparison of the film heat transfer coefficient between three authors

Ample work has been done on dry-cooled bare tube bundles. Pressure drop correlations such as those published by Gaddis & Gnielinski (1985) and Zukauskas & Ulinskas (1983) are very generic with wide applicable ranges. The convective heat transfer coefficient correlation of Parker & Treybal (1961) is applicable specifically to 19 mm outer diameter tubes with a similar Reynolds number range. Zukauskas (1987) supplied many Nusselt number correlations for various ranges of Reynolds and Prandtl numbers and the applicable correlation is used, while the Nusselt number correlation of Khan et al. (2006) is based on an analytical analysis of the heat transfer. These correlations for the pressure drop and the Nusselt number with applicable ranges can be used to verify the accuracy of the experimental data.

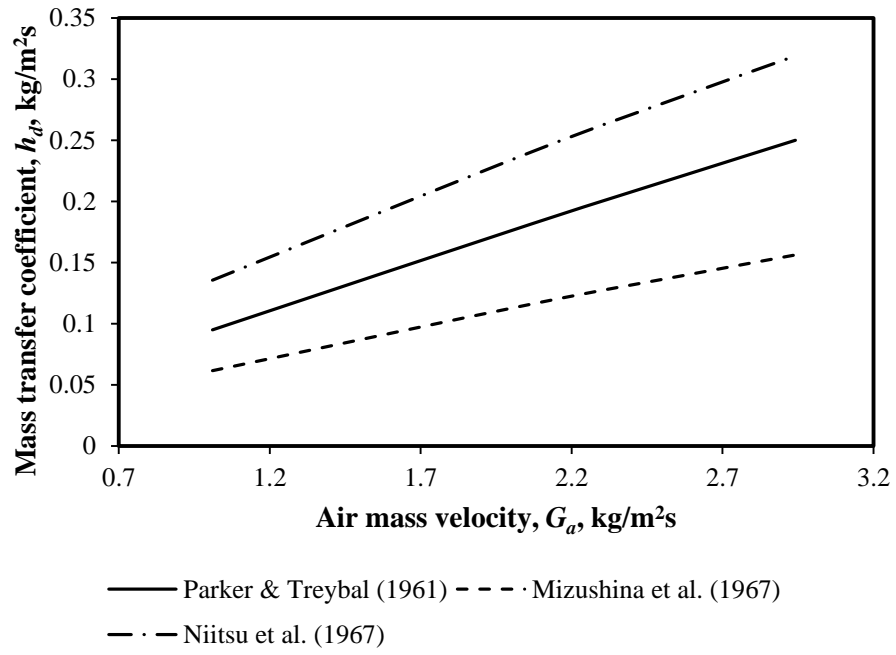


Figure 2.2: Comparison of the mass transfer coefficient between three authors

3 Theoretical analysis

3.1 Introduction

In this chapter, theory is developed to evaluate the performance of horizontal air-cooled heat exchanger bundles with water or steam as the process fluid, operating under deluged (wet) and dry conditions.

3.2 Tube bundle operated as an evaporative cooler

3.2.1 Derivation of the governing equations

Figure 3.1 is an illustration of a control volume of a horizontal heat exchanger tube used to derive and manipulate the governing equations for wet operation. A hot process fluid flows inside the tube, the outer surface of the tube is deluged with water falling vertically downwards under gravity and air flows vertically upwards. This method of analysis is based on the method presented by Bourillot (1983) and Poppe & Rögener (1984) as cited in Erens & Dreyer (1993), Kröger (2004) and Heyns (2008). The analysis of the heat transfer from the deluge water surface to the air stream is similar to that generally applied to evaporative systems.

Assumptions that are made in this analysis:

- It is a steady state process.
- The operating temperatures are low and radiation heat transfer is not taken into account.
- The temperature and the humidity of the air at the air-water interface correspond with the temperature and humidity of a saturated air-vapor mixture at the mean deluge water temperature.
- The air, deluge water and process fluid flow distributions are uniform throughout the bundle with uniform wetting of the tubes permitting this analysis to be carried out in one dimension.

A dry air mass balance of the control volume yields,

$$(G_{a,z} - G_{a,z+\Delta z})\Delta x\Delta y = 0 \quad (3.1)$$

Dividing Eq. (3.1) with the volume $\Delta x\Delta y\Delta z = 0$ yields,

$$\frac{(G_{a,z} - G_{a,z+\Delta z})}{\Delta z} = 0 \quad (3.2)$$

A water mass balance of the control volume after noting that $G_{w,y} = G_{w,y+\Delta y}$ is written as,

$$(G_{dw,z+\Delta z} - G_{dw,z})\Delta x\Delta y = (G_{a,z+\Delta z}w_{a,z+\Delta z} - G_{a,z}w_{a,z})\Delta x\Delta y \quad (3.3)$$

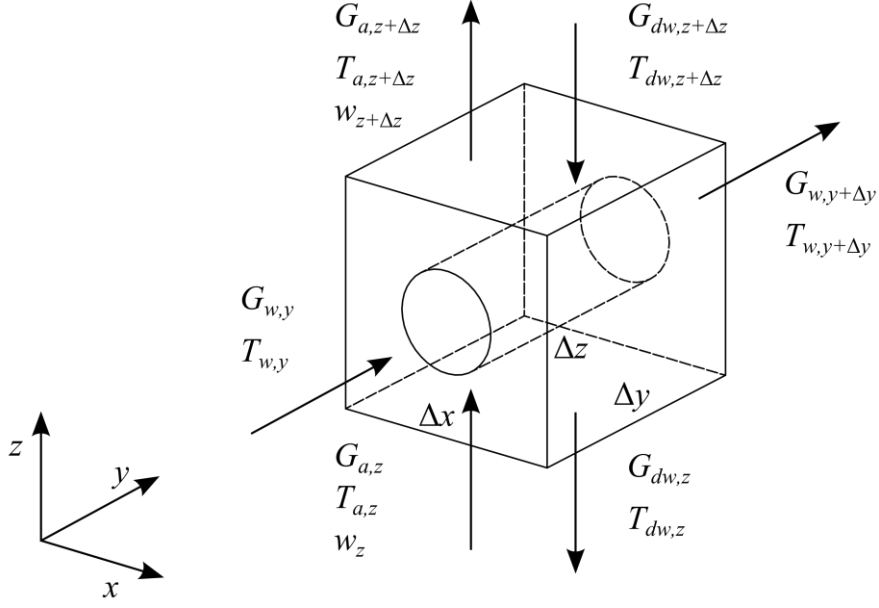


Figure 3.1: Control volume of an evaporative cooler

Divide Eq. (3.3) with the volume $\Delta x\Delta y\Delta z = 0$ to obtain,

$$\frac{(G_{dw,z+\Delta z} - G_{dw,z})}{\Delta z} = \frac{(G_{a,z+\Delta z}w_{a,z+\Delta z} - G_{a,z}w_{a,z})}{\Delta z} \quad (3.4)$$

From the first law of thermodynamics

$$\delta Q_w + \delta Q_a + \delta Q_{dw} = 0 \quad (3.5)$$

The heat transfer from the process fluid is

$$\delta Q_w = G_w c_{pw} (T_{w,y} - T_{w,y+\Delta y}) \Delta x \Delta z \quad (3.6)$$

The air-side heat transfer is

$$\delta Q_a = G_a (i_{ma,z+\Delta z} - i_{ma,z}) \Delta x \Delta y \quad (3.7)$$

where $i_{ma,z}$ denotes the mean enthalpy of air per kg of dry air and defined as

$$i_{ma,z} = c_{pa} T_{a,z} + w (i_{fgw0} + c_{pv} T_{a,z}) \quad (3.8)$$

where i_{fgw0} is the latent heat of evaporation at 0 °C and the specific heat of air and vapor are evaluated at $T_{a,z}/2 + 273.15$ K. The heat transfer rate to the deluge water is

$$\delta Q_{dw} = [c_{pdw} (G_{dw,z} T_{dw,z} - G_{dw,z+\Delta z} T_{dw,z+\Delta z})] \Delta x \Delta y \quad (3.9)$$

Substituting Eqs. (3.6), (3.7) and (3.9) into (3.5) and dividing with the volume $\Delta x \Delta y \Delta z$ yields,

$$\begin{aligned} \frac{G_w c_{pw} (T_{w,y} - T_{w,y+\Delta y})}{\Delta y} &= \frac{G_a (i_{ma,z+\Delta z} - i_{ma,z})}{\Delta z} \\ &+ \frac{[c_{pdw} (G_{dw,z} T_{dw,z} - G_{dw,z+\Delta z} T_{dw,z+\Delta z})]}{\Delta z} \end{aligned} \quad (3.10)$$

where the deluge water temperature T_{dw} and the process fluid T_w are in °C. Employing a shorthand of the temperature and enthalpy differences over the control volume indicated with a Δ , applying the product rule and noting that this equation can be solved in one dimension, simplifies to

$$G_a \Delta i_{ma} = -G_w c_{pw} \Delta T_w + c_{pdw} (\Delta G_{dw} T_{dw} + G_{dw} \Delta T_{dw}) \quad (3.11)$$

Rearranging to get the change in deluge water, ΔT_{dw} , as the subject yields

$$\Delta T_{dw} = \frac{1}{c_{pdw} G_{dw}} (G_a \Delta i_{ma} + G_w c_{pw} \Delta T_w - c_{pdw} \Delta G_{dw} T_{dw}) \quad (3.12)$$

Figure 3.2 illustrates the heat transfer equations and an overview of the thermal resistance circuit with all the applicable temperatures and fluid streams. Depending on state of the process fluid, sensible or latent heat is transferred from the hot process fluid inside the horizontal tube to the lateral vertical air-stream by means of convection between the process fluid and the inner tube wall, conduction through the tube wall, convection between the outer tube wall and the deluge water film and convection and mass transfer between the deluge water surface and the air-stream.

At the air-water interface the heat transfer takes place in the form of convective heat transfer and mass transfer,

$$\delta Q = \delta Q_c + \delta Q_m \quad (3.13)$$

where the subscripts c and m refer to convective heat transfer and mass transfer. The convective heat transfer rate is expressed by

$$\delta Q_c = h_a (T_{dw} - T_a) \delta A \quad (3.14)$$

The enthalpy of the saturated air evaluated at the mean deluge water temperature

$$i_{masdw} = c_{pa} T_{dw} + w_{sdw} (i_{fgwo} + c_{pv} T_{dw}) \quad (3.15)$$

The enthalpy of the air vapor at the bulk deluge water temperature with c_{pv} evaluated at $T_{dw}/2 + 273.15$ K is

$$i_v = i_{fgwo} + c_{pv}T_{dw} \quad (3.16)$$

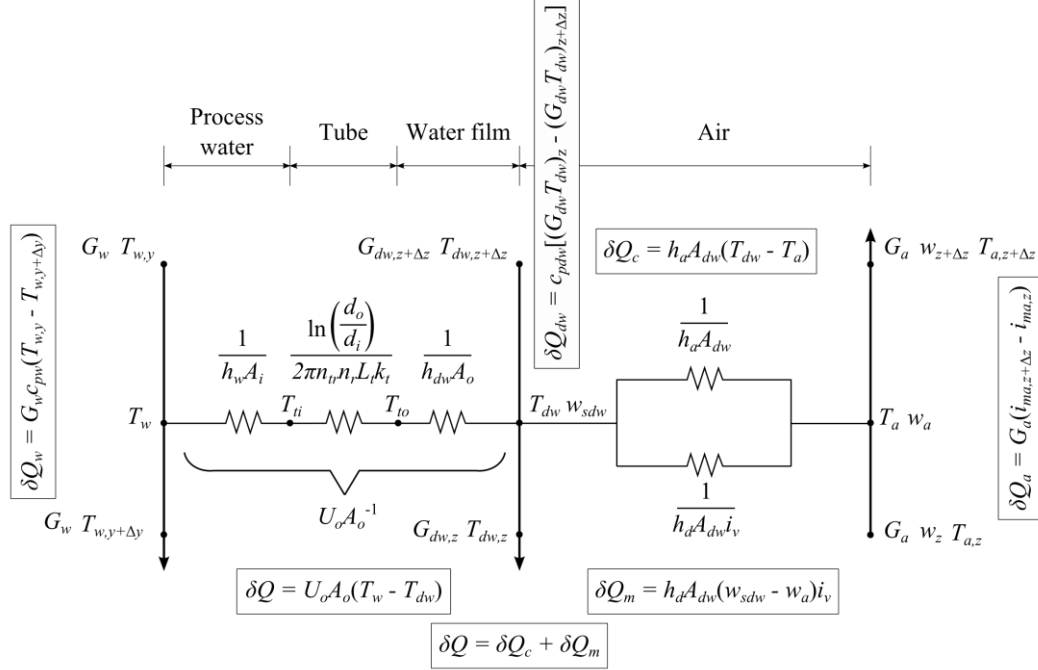


Figure 3.2: Resistance diagram of the control volume for wet operation

Substituting Eq. (3.16) into (3.15) and rewriting it as

$$i_{masdw} = c_{pa}T_{dw} + wi_v + (w_{sdw} - w)i_v \quad (3.17)$$

c_{pa} is evaluated at $T_{dw}/2 + 273.15$ K and subtracting the enthalpy of air

$$i_{masdw} - i_{ma} = c_{pa}T_{dw} + wi_v + (w_{sdw} - w)i_v - [c_{pa}T_a + w(i_{fgwo} + c_{pv}T_a)] \quad (3.18)$$

Substituting Eq. (3.16) into (3.18) and neglecting the small differences in the specific heats, it can be reduced to

$$i_{masdw} - i_{ma} \approx (c_{pa} + wc_{pv})(T_{dw} - T_a) + (w_{sdw} - w)i_v \quad (3.19)$$

Rearranging and noting that $c_{pma} = c_{pa} + wc_{pv}$ we find

$$T_{dw} - T_a = \frac{i_{masdw} - i_{ma} - (w_{sdw} - w)i_v}{c_{pma}} \quad (3.20)$$

The mass transfer at the air-water interface is given by,

$$(G_{dw,z+\Delta z} - G_{dw,z})\Delta x\Delta y = h_d(w_{sdw} - w)\delta A \quad (3.21)$$

where w_{sdw} is the saturated humidity of air at the bulk mean deluge water temperature T_{dw} . The enthalpy transfer due to mass transfer is

$$\delta Q_m = i_v(G_{dw,z+\Delta z} - G_{dw,z})\Delta x\Delta y = i_v h_d(w_{sdw} - w)\delta A \quad (3.22)$$

Substituting Eqs. (3.14), (3.20) and (3.22) into (3.13) to find

$$\begin{aligned} \delta Q = \frac{h_a}{c_{pma}}(i_{masdw} - i_{ma} - (w_{sdw} - w)i_v)\delta A \\ + i_v h_d(w_{sdw} - w)\delta A \end{aligned} \quad (3.23)$$

After rearranging the terms

$$\begin{aligned} \delta Q = h_d \left[\frac{h_a}{c_{pma}h_d}(i_{masw} - i_{ma}) \right. \\ \left. + \left(1 - \frac{h_a}{c_{pma}h_d}\right)i_v(w_{sw} - w) \right] \delta A \end{aligned} \quad (3.24)$$

where $h_a/(c_{pma}h_d) = Le_f$, which is the Lewis factor and relates the rate of heat and mass transfer in an evaporative process. Finlay & Harris (1984) did not group the convection and mass transfer at the air-water interface but kept the terms separate as indicated in Figure 3.2 with a Lewis factor of unity. Substituting the Lewis factor and noting that $\Delta i_{ma} = \delta Q/G_a$, Eq. (3.24) becomes

$$\Delta i_{ma} = \frac{h_a \delta A}{G_a} [Le_f(i_{masdw} - i_{ma}) + (1 - Le_f)i_v(w_{sw} - w)] \quad (3.25)$$

Noting that $\delta A = \delta A_o$ implies that h_d is not based on the air-water interfacial area but on the outer surface area of the tube bundle, A_o , and is referred to as h_{de} . Eq. (3.25) can reduce to

$$\Delta i_{ma} = \frac{h_{de} \delta A_o}{G_a} [Le_f(i_{masdw} - i_{ma}) + (1 - Le_f)i_v(w_{sdw} - w)] \quad (3.26)$$

Employing the Merkel (1925) assumptions of negligible evaporation ($\Delta G_{dw} = 0$) and the Lewis factor of unity, that corresponds to an equal heat transfer rate between sensible heat and mass transfer, reduce Eqs. (3.12) and (3.26) to

$$\Delta T_{dw} = \frac{1}{c_{pdw}G_{dw}} (G_a \Delta i_{ma} + G_w c_{pw} \Delta T_w) \quad (3.27)$$

and

$$\Delta i_{ma} = \frac{h_{de} \delta A_o}{G_a} (i_{masdw} - i_{ma}) \quad (3.28)$$

The parallel resistances for convection and mass transfer from the deluge water surface as illustrated in Figure 3.2 has been replaced with an equivalent single resistance through the covered analysis and is shown in Figure 3.3.

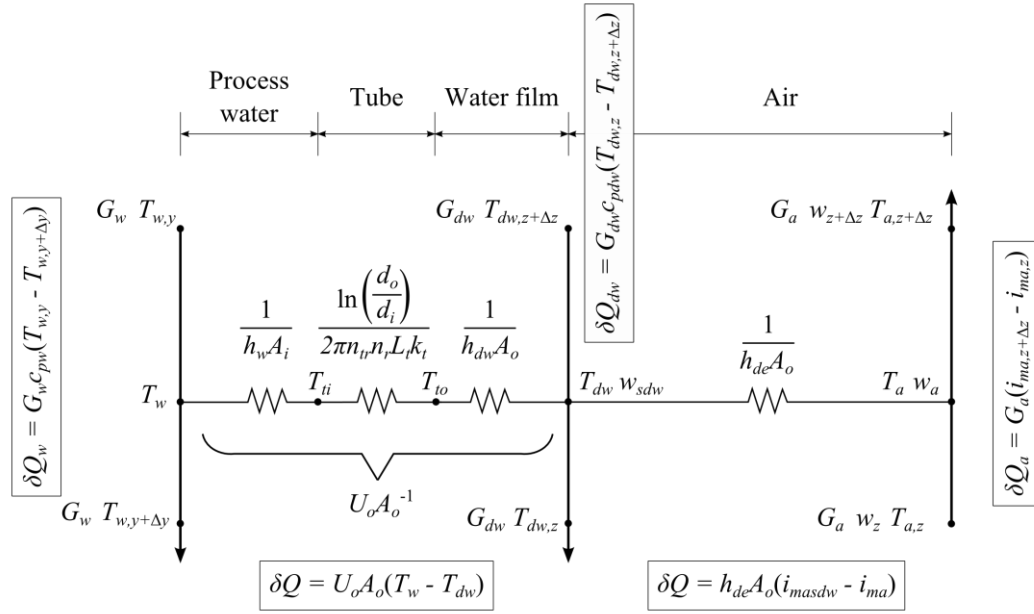


Figure 3.3: Resistance diagram of the control volume for wet operation with the replaced resistance

3.2.2 Integral governing equations

The above two equations are often applied in the performance evaluation of evaporation systems and is referred to as the Merkel type method of analysis. These equations can be solved numerically by employing the Chebyshev integration technique over the deluge water temperature, but with the inlet and outlet deluge water temperature being equal, the numerical integration is trivial (Heyns & Kröger, 2010). Kröger (2004) suggest the use of the Effectiveness-NTU method of analysis for evaporative cooler/condensers. This method includes the variation of temperature of the process fluid and the enthalpy of air throughout the heat exchanger and is based on a constant mean deluge water temperature ($\Delta T_{dw} = 0$).

The transfer characteristics are determined from this mean deluge water temperature which is an arithmetic average of the temperatures measured throughout the height of the bundle. Mizushima et al. (1967) and Heyns (2008) found the maximum deviation from the average temperature is < 3 °C. The saturated air enthalpy at the surface of the deluge water, i_{masdw} , is calculated at this mean temperature. The integral heat transfer equation can be obtained from Eq. (3.27) by integrating over the whole tube bundle flow area and applying $\Delta T_{dw} = 0$ to arrive at,

$$Q = m_a(i_{mao} - i_{mai}) = m_w c_{pw}(T_{wi} - T_{wo}) \quad (3.29)$$

The enthalpy of the air at the outlet is determined from Eq. (3.29). By letting $\Delta i_{ma}, \delta A_o \rightarrow 0$ of Eq. (3.28), yields a differential equation that is integrated between i_{mao} and i_{mai} and over the whole tube bundle flow area to obtain,

$$i_{mao} = i_{masdwm} - (i_{masdwm} - i_{mai})e^{-NTU_a} \quad (3.30)$$

with $NTU_a = h_{de}A_o/m_a$.

An examination of the heat transfer from the process fluid to the deluge water is needed to obtain an equation which governs the third parameter, ΔT_w , the process fluid temperature difference over the tube bundle and is

$$m_w c_{pw} \Delta T_w = U_o (T_w - T_{dwm}) \delta A_o \quad (3.31)$$

By letting $\Delta T_w, \delta A_o \rightarrow 0$ of Eq. (3.31), yields a differential equation that can be integrated between T_{wi} and T_{wo} and over the whole tube bundle flow area. Substituting the mean deluge water temperature yields,

$$T_{wo} = T_{dwm} + (T_{wi} - T_{dwm}) e^{-NTU_w} \quad (3.32)$$

where $NTU_w = U_o A_o / m_w c_{pw}$ and U_o is the overall heat transfer coefficient for the tube bundle which is expressed as

$$U_o = \left[\frac{d_o}{h_w d_i} + \frac{d_o \ln \left(\frac{d_o}{d_i} \right)}{2k_t} + \frac{1}{h_{dw}} \right]^{-1} \quad (3.33)$$

3.2.3 Evaluation of the heat and mass transfer coefficients from experimental data

During the experimental performance evaluation of the tube bundle the process fluid used is water instead of steam. The forced convection heat transfer coefficient for water is similar in the order of magnitude as the heat transfer coefficient for condensing steam. In steady state conditions the in- and outlet deluge water temperature is the same because it is recirculated with a deluge water pump. In addition the following assumptions are made to determine the transfer coefficients:

- The effect of the deluge water pump work on the deluge water temperature may be neglected.
- The outlet air is assumed saturated for all operating conditions.

The deluge and process water and air mass flow rates are determined with the physical properties of the experimental setup and the thermo-physical properties of the fluids as defined in Kröger (2004). Rearrange and aggregate the terms of

Eq. (3.32) to find an expression for the product of the overall heat transfer coefficient and the outer area,

$$U_o A_o = -m_w c_{pw} \ln \left(\frac{T_{wo} - T_{dwm}}{T_{wi} - T_{dwm}} \right) \quad (3.34)$$

The convective heat transfer coefficient for the process water inside the tubes are obtained from the relation developed by Gnielinski as presented in Kröger (2004)

$$Nu_w = \frac{h_w d_i}{k_w} = \frac{\left(\frac{f_D}{8}\right) (Re_w - 1000) Pr_w \left[1 + \left(\frac{d_i}{L_t}\right)^{0.67}\right]}{1 + 12.7 \left(\frac{f_D}{8}\right)^{0.5} (Pr_w^{0.67} - 1)} \quad (3.35)$$

with the friction factor of the tubes defined by Haaland also presented in Kröger (2004),

$$f_D = 0.3086 \left\{ \log \left[\frac{6.9}{Re_w} + \left(\frac{\epsilon_t}{d_i 3.75} \right)^{1.11} \right] \right\}^{-2} \quad (3.36)$$

The surface roughness of the tube is taken as $\epsilon_t = 0.15$ mm which is a typical value used for galvanized steel. Rearranging Eq. (3.33), the deluge water film convective heat transfer coefficient can be determined from Eq. (3.37) after substituting the process water convective heat transfer coefficient from Eq. (3.35) and the result of (3.34),

$$h_{dw} = \frac{1}{A_o} \left[\frac{1}{U_o A_o} - \frac{1}{h_w A_i} - \frac{\ln \left(\frac{d_o}{d_i} \right)}{n_r n_{tr} L_t 2\pi k_t} \right]^{-1} \quad (3.37)$$

The mass transfer coefficient determination starts with rearranging Eq. (3.30) to obtain,

$$NTU_a = -\ln \left[-\frac{i_{mao} - i_{masdwm}}{i_{masdwm} - i_{mai}} \right] \quad (3.38)$$

From Eq. (3.38) a Merkel number is obtained for the experimental setup,

$$Me_{ex} = \frac{NTU_a G_a A_{fr}}{m_{dw}} \quad (3.39)$$

The Merkel number for the tube bundle is determined by subtracting the trough and spray zone Merkel number from the experimental Merkel number. The trough and spray zone location and function will be discussed in Chapter 4 and their contribution to the mass transfer is detailed in Chapter 5.

$$Me_{tb} = Me_{ex} - Me_{tr} \quad (3.40)$$

The bundle mass transfer coefficient is,

$$h_d = \frac{Me_{tb}m_{dw}}{A_o} \quad (3.41)$$

The bundle air-side loss coefficient is obtained from,

$$K_{tb} = 2[\Delta p_{tb} - (\rho_{avo}v_{avo}^2 - \rho_{avi}v_{avi}^2)]\rho_{avm} \left(\frac{A_{fr}}{m_{avm}} \right)^2 \quad (3.42)$$

3.2.4 Performance evaluation of the deluged tube bundle

Figure 3.4 depicts a procedure flow chart to determine the performance of a tube bundle operated as an evaporative cooler. The procedure starts at the top with a chosen outlet process water, mean deluge water and outlet air temperature. The new values of the iteration parameters are calculated with Eqs. (3.32), (3.43) and (3.44). A relaxation factor of 0.1 is used for all three parameters. The system is iterated until the equations converge within a chosen convergence interval.

New outlet air temperature,

$$T_{ao} = \frac{i_{mao} - w_{so}i_{fgwo}}{c_{pao} + w_{so}c_{pvo}} \quad (3.43)$$

The new deluge water temperature,

$$T_{dwm} = T_{wi} - \frac{m_a(i_{masdwm} - i_{mai})[1 - \exp(-NTU_a)]}{m_w c_{pwm}[1 - \exp(-NTU_w)]} \quad (3.44)$$

Pressure drop over the tube bundle

$$\Delta p_{tb} = \frac{K_{tb}m_{avm}^2}{2\rho_{avm}A_{fr}} + \rho_{avo}v_{avo}^2 - \rho_{avi}v_{avi}^2 \quad (3.45)$$

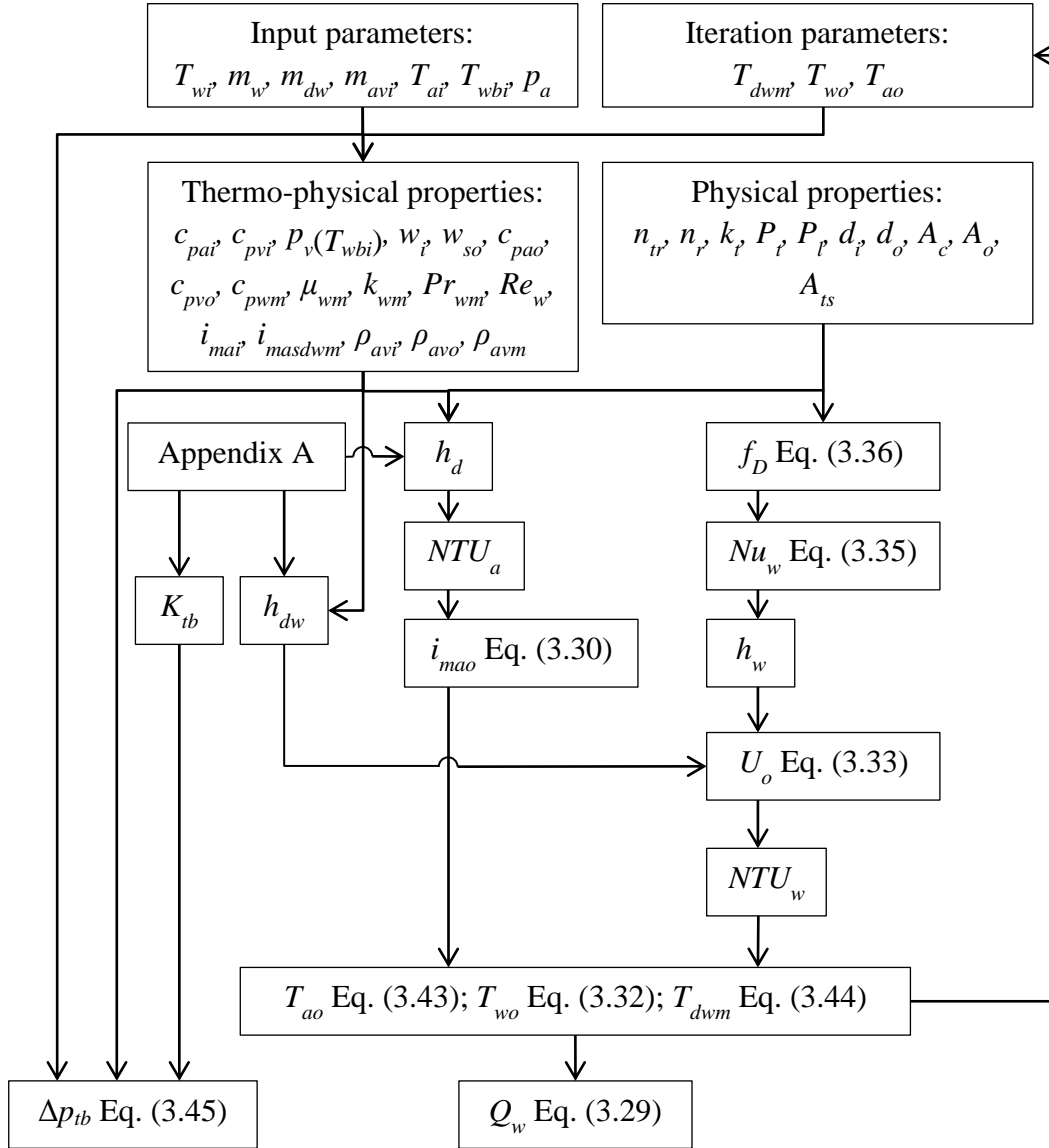


Figure 3.4: Procedure flow chart to determine the wet tube bundle performance

3.3 Tube bundle operated as a dry air-cooled heat exchanger

3.3.1 Derivation of the governing equations

Referring to Figure 3.1 the governing equations for the dry-cooled heat exchanger can be derived by setting $G_{dw} = 0 \text{ kg/m}^2\text{s}$ and following a similar procedure as already discussed. The analysis is simpler with only two fluids present. Figure 3.5 depicts the thermal resistance diagram of the heat flow through the control volume for dry operation.

$$\delta Q = G_w c_{pw} (T_{w,y} - T_{w,y+\Delta y}) = G_{av} c_{pav} (T_{a,z+\Delta z} - T_{a,z}) \quad (3.46)$$

and

$$\delta Q = U_o A_o F_T \Delta T_{lm} \quad (3.47)$$

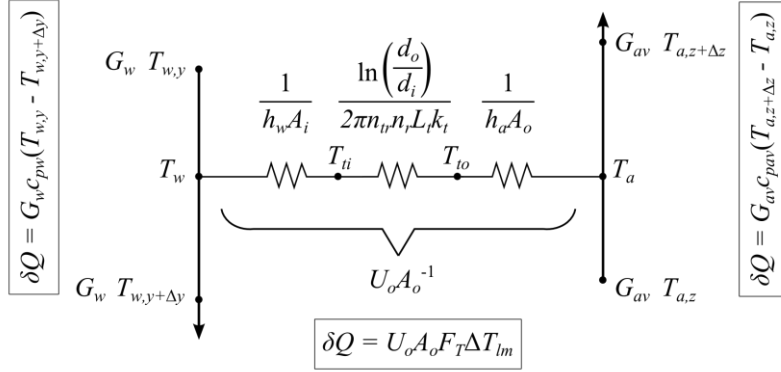


Figure 3.5: Resistance diagram of the control volume for dry operation

3.3.2 Integral governing equations

The integral equations can be obtained by integrating over the total flow area of the tube bundle that leads to

$$Q = m_w c_{pw} (T_{wi} - T_{wo}) = m_{av} c_{pav} (T_{ao} - T_{ai}) \quad (3.48)$$

and

$$Q = U_o A_o F_T \Delta T_{lm} \quad (3.49)$$

with the temperature correction factor for cross-flow heat exchangers with both streams unmixed defined as $F_T \approx 1$.

3.3.3 Evaluation of the air-side heat transfer coefficient from experimental data

After determining all the applicable thermo-physical properties of air and process water, the heat transfer is determined with Eq. (3.48). The internal water flow friction factor and the corresponding Nusselt number are determined with Eqs. (3.36) and (3.35) respectively. The logarithmic temperature difference for the tube bundle in a counterflow arrangement

$$\Delta T_{lm} = \frac{(T_{wo} - T_{ai}) - (T_{wi} - T_{ao})}{\ln \left(\frac{T_{wo} - T_{ai}}{T_{wi} - T_{ao}} \right)} \quad (3.50)$$

The product of the overall heat transfer coefficient and the outer tube area is determined with

$$U_o A_o = \frac{Q_m}{F_T \Delta T_{lm}} \quad (3.51)$$

with $Q_m = 0.5(Q_a + Q_w)$ and $F_T \approx 1$. The air-side convective heat transfer coefficient is

$$h_a = \left\{ A_o \left[\frac{1}{U_o A_o} - \frac{1}{h_w A_i} - \frac{\ln\left(\frac{d_o}{d_i}\right)}{n_r n_{tr} L_t 2\pi k_t} \right] \right\}^{-1} \quad (3.52)$$

and the loss coefficient for the tube bundle under dry operation

$$K_{tb} = \frac{2(\Delta p_{tb} + \rho_{avi} v_{avi}^2 - \rho_{avo} v_{avo}^2)}{\rho_{avm} v_{avm}^2} \quad (3.53)$$

3.3.4 Performance evaluation of the convectively cooled dry tube bundle

The performance of a convectively cooled tube bundle can either be solved with the Logarithmic Temperature Difference or the Effectiveness-NTU method. The procedure to solve the performance of a convectively cooled tube bundle with the former method is depicted in Figure 3.6. The outlet air and process water temperature, T_{ao} and T_{wo} , and outer tube wall temperature, T_{to} , are the unknown parameters. The procedure is followed from the top with first estimates for the mentioned parameters. A relaxation factor of 0.1 would again be sufficient for the iteration parameters. The system converges when these parameters yield the heat transfer from Eqs. (3.48) and (3.49) within a chosen convergence interval.

The air-side convective heat transfer coefficient is determined from the obtained Nusselt number, $h_a = Nu_D k_{avm} / d_o$. The universal heat transfer coefficient is expressed as follows,

$$U_o = \left[\frac{d_o}{h_w d_i} + \frac{d_o \ln\left(\frac{d_o}{d_i}\right)}{2k_t} + \frac{1}{h_a} \right]^{-1} \quad (3.54)$$

It is quite common to determine the air thermo-physical properties at the mean outer surface temperature in order to determine the air-side Nusselt number. The mean outer tube surface temperature

$$T_{to} = T_{wm} - Q \left[\frac{1}{h_w A_i} + \frac{\ln\left(\frac{d_o}{d_i}\right)}{2\pi k_t n_{tr} n_r L_t} \right] \quad (3.55)$$

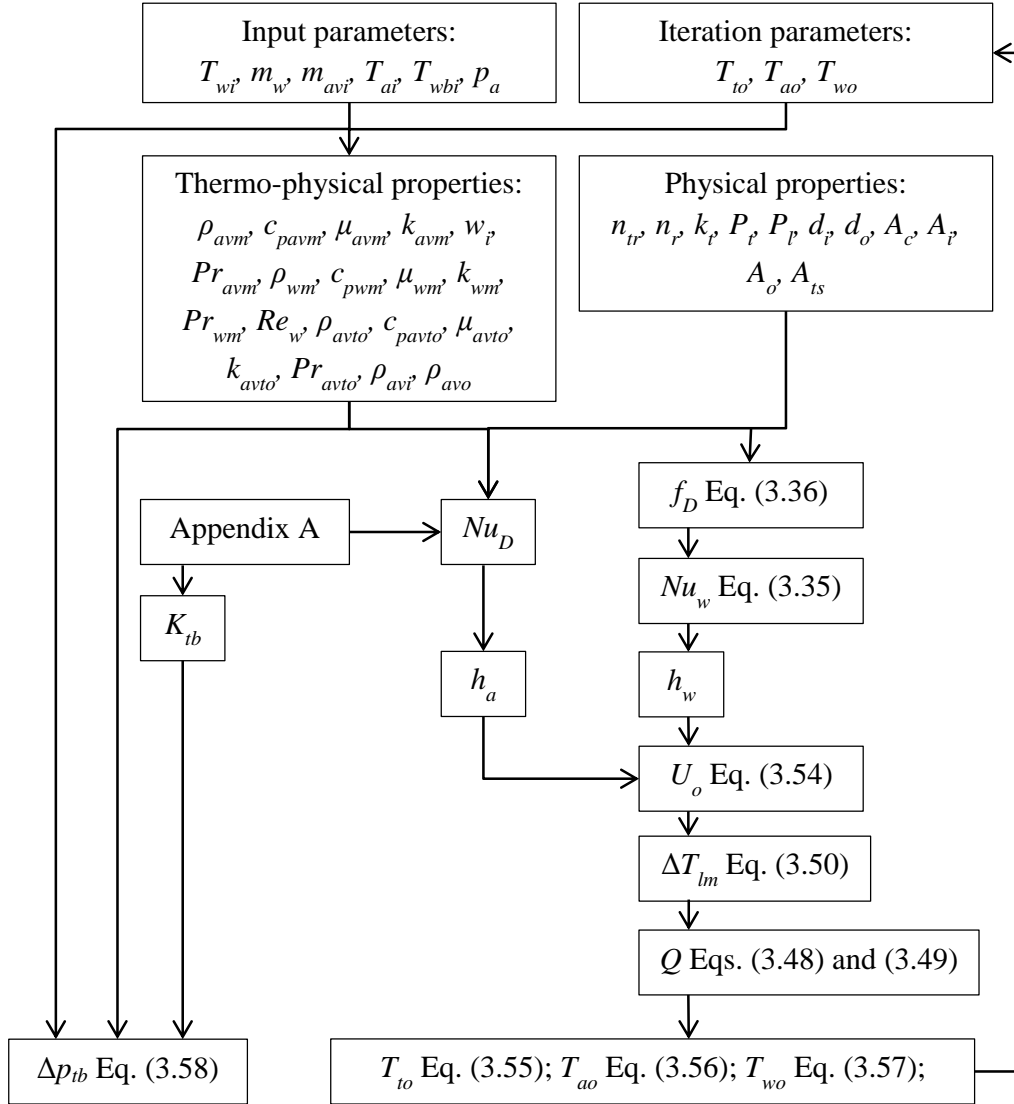


Figure 3.6: Procedure flow chart to determine the dry tube bundle performance

The new outlet air temperature,

$$T_{ao} = T_{ai} + \frac{Q}{m_{avi} c_{pavm}} \quad (3.56)$$

Similarly the outlet water temperature can be determined as

$$T_{wo} = T_{wi} - \frac{Q}{m_w c_{pwm}} \quad (3.57)$$

The pressure drop over the tube bundle is determined by rearranging the terms of Eq. (3.53) and is the same as Eq. (3.45) but represented slightly different,

$$\Delta p_{tb} = \frac{K_{tb} \rho_{avm} v_{avm}^2}{2} + \rho_{avo} v_{avo}^2 - \rho_{avi} v_{avi}^2 \quad (3.58)$$

4 Experimental evaluation of the tube bundle performance

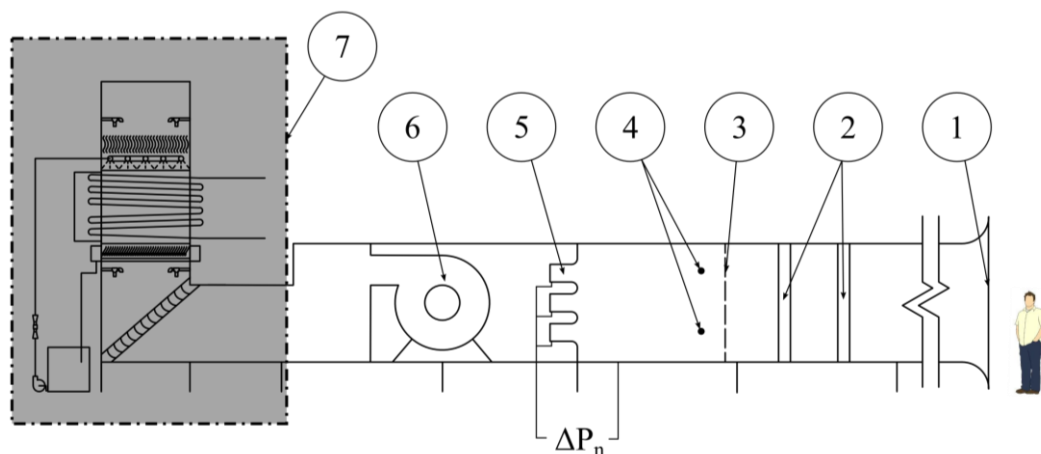
4.1 Introduction

This chapter describes the experimental apparatus, the measurement- and data acquisition techniques and provides a test procedure associated with the experimental evaluation of the tube bundle. The performance characteristics are obtained from the experimental results according to the method of analysis presented in Chapter 4. The calibration of all the measuring equipment in this section is detailed in Appendix C.

4.2 Description of the experimental apparatus

4.2.1 Wind tunnel

Figure 4.1 is a depiction of the wind tunnel. Air is drawn into the wind tunnel by a centrifugal fan (6) through the rounded inlet (1) to obtain a uniform velocity profile. It then continues to two sets of mixing vanes (2) and a flow straightener screen (3) before psychrometers (4) measure the dry- and wet-bulb temperature of the air.



- | | |
|---------------------|--------------------------------|
| 1. Bellmouth inlet | 5. ASHRAE 51 – 75 flow nozzles |
| 2. Mixing vanes | 6. Fan |
| 3. Flow straightner | 7. Counter-flow section |
| 4. Psychrometers | |

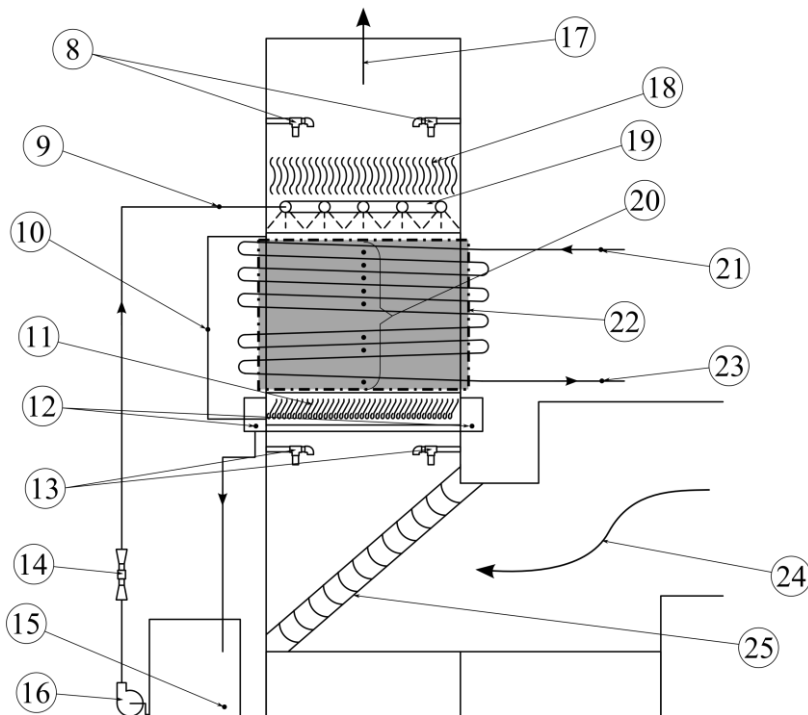
Figure 4.1: Wind tunnel

The two sets of mixing vanes (2) are installed to obtain a uniform air temperature at the psychrometers (4) to reduce the number of thermocouples required to measure the bulk mean temperature. The mean values are used to determine the density of air upstream of the flow nozzles. The air flow rate, m_{avi} , is determined

using this air density and the measured pressure drop across three ASHRAE 51-75 elliptical flow nozzles (5). The air then passes through a centrifugal fan, a number of bends and a set of guide vanes before entering the counter-flow test section (7).

4.2.2 Counter-flow test section

Figure 4.2 presents the counter-flow test section which has a square cross-sectional area of 2.25 m^2 . Hot process water, m_w , is pumped from a 45 000 L storage tank to the test bundle (22) with pumps located at the tank. The water in the tank is heated by circulating it through a 150 kW diesel boiler. Process water enters the bundle at (21) where the inlet water temperature, T_{wi} is measured. There is a pressure gauge in the inlet header of the bundle to ensure a safe operating pressure. The process water exits the bundle at (23) where the outlet water temperature, T_{wo} is measured.



- | | |
|---|--|
| 8. Outlet psychrometers, T_{ao} and T_{wbo} | 17. Air outlet |
| 9. Deluge water inlet temperature, T_{dwi} | 18. Drift eliminator |
| 10. Pressure drop over tube bundle, Δp_{tb} | 19. Spray frame |
| 11. Collecting troughs | 20. Deluge water temperature, T_{dw} |
| 12. Outlet deluge water temperature, T_{dwo} | 21. Water inlet temperature, T_{wi} |
| 13. Inlet psychrometers, T_{ai} and T_{wbi} | 22. Tube bundle |
| 14. Venturi flow meter, m_{dw} | 23. Water outlet temperature, T_{wo} |
| 15. Sump temperature, T_{dws} | 24. Air inlet |
| 16. Deluge water pump | 25. Inlet guide vanes |

Figure 4.2: Counter-flow test section (point 7 in Fig. 5.1)

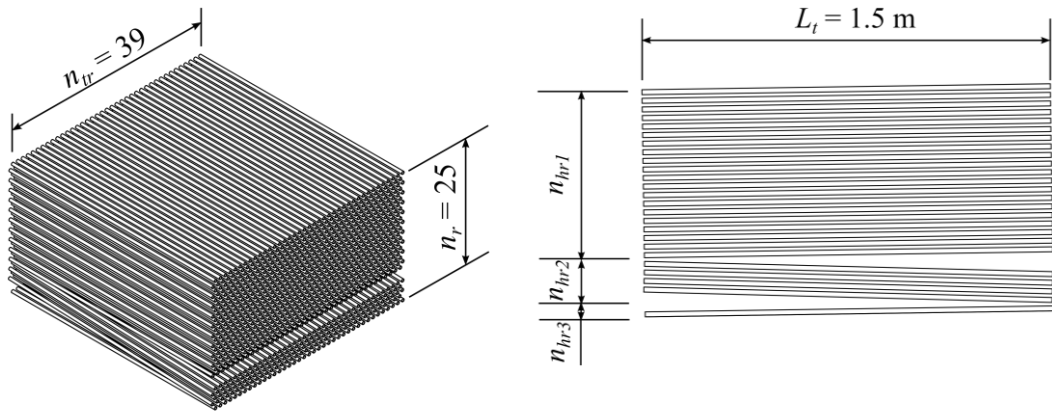
Air enters the counter-flow section at (24), passing through a set of guide vanes (25) and psychrometers (13). The air then flows through the test section that is composed of the deluge water collecting troughs (11), the tube bundle (22), spray frame (19) and a drift eliminator (18) that removes any entrained droplets from the outlet air stream before it reaches the outlet air psychrometers (8). The air then finally exits at the air outlet (17). The air-side pressure drop over the bundle is measured at (10) in order to determine the tube bundle loss coefficient.

The deluge water is supplied by a pump (15) and the flow rate, m_{dw} , is measured with a Venturi flow meter (14). The deluge water inlet temperature, T_{dwi} , is measured at the spray frame inlet (9). The spray frame (19) is designed to uniformly wet the entire cross-sectional area of the counter-flow test section. The deluge water trickles through the tube bundle (22) under gravity before it is collected by a set of collecting troughs (11). The outlet deluge water temperature, T_{dwo} , is measured at (12) before ending up in the sump where the temperature, T_{dws} is again measured (15).

4.2.3 Tube bundle specifications

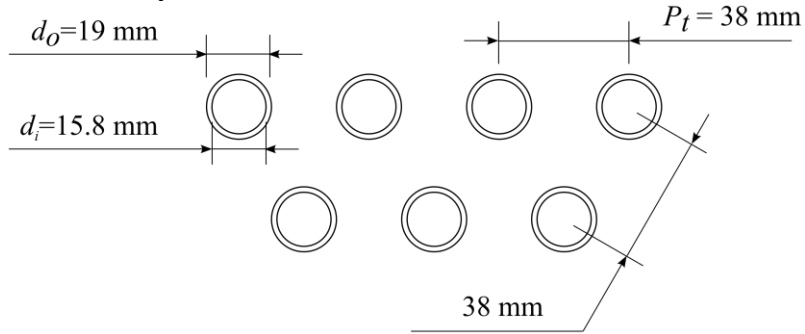
The details of the tube bundle are depicted in Figure 4.3. The tubes have an outer and inner diameter of 19 and 15.8 mm respectively and are arranged in triangular pattern with a pitch of 38 mm as shown in Figure 4.3(c). The bundle has 25 tube rows and 39 tubes per row as illustrated in Figure 4.3(a). These tubes have been externally and internally galvanized and have a length of 1.5 m. Referring to Figure 4.3 (b), the first 20 tubes rows are inclined with a 1° slope, followed by four tube rows with the same slope but in the opposite direction, followed by the final tube row with the slope and direction of the initial 20 tube rows. This is geometrically similar to the second stage tube bundle of the hybrid dephlegmator although the second stage bundles have three passes and the experimental tube bundle has 25 passes. The walls of the experimental bundle are fitted with half tubes made of conduit PVC tubing to ensure minimal edge effects and a uniform air flow during tests.

Figure 4.4 is a photo of the tube bundle with the outlet header in the foreground. Rubber molded U-bends connect the tubes in consecutive tube rows, due to the small pitch of the tubes and the decision to keep all the fluid streams for all 39 tubes per row separate. These rubber U-bends were fastened to the tubes with hose clamps. The white conduit tubing can be seen in the window in the side of the tube bundle.



(a) Isometric view of the tube layout

(b) Side view of the tube layout



(c) Depiction of the tube arrangement

Figure 4.3: Test bundle tube layout

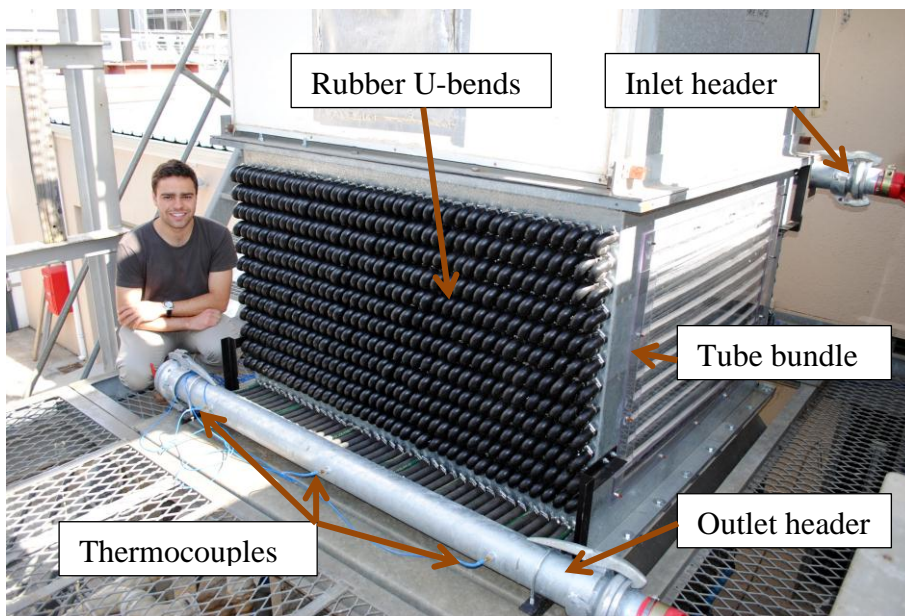


Figure 4.4: Photo of the tube bundle

4.3 Measurement techniques

4.3.1 Temperature

A total of 45 type T (copper-constantan) thermocouples are used to measure temperature. All these thermocouples are calibrated with a FLUKE 9142 Field Metrology Well and a four wire reference Platinum Resistance Temperature Detector (PRTD). Temperature is varied in the hot well of the Fluke Calibrator from 10 – 60 °C in increments of 10 °C and the logged temperatures of the thermocouples are corrected to the readings of the four wire reference PRTD. The following linear relations are obtained for each thermocouple:

$$T_{calibrated} = mT_{raw} + c \quad (4.1)$$

The coefficients m and c are obtained from linear regression between the raw thermocouple readings and the reference PRTD measurement. More details are in Appendix C.

Figure 4.5 is an illustration of a psychrometer to determine the dry- and wet-bulb temperature of air according to the standards documented in ASHRAE 41.1 (2013). Two thermocouples are located in a PVC pipe with air drawn over them at a velocity of between 3 to 5 m/s by means of a centrifugal fan. The wet-bulb thermocouple has a cotton wick pulled over its tip with the one end immersed in water allowing it to absorb water to keep it wet. Evaporation of the water causes the wick to reach wet-bulb temperature which is measured by the thermocouple.

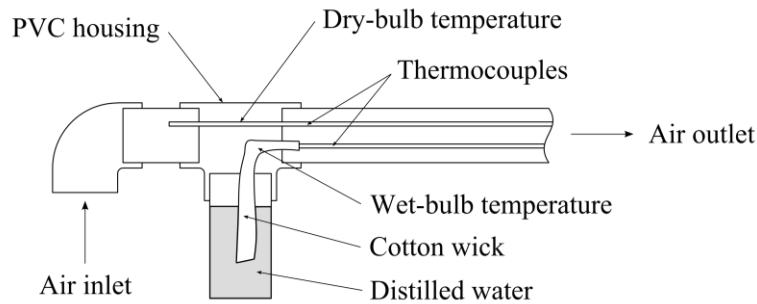


Figure 4.5: Psychrometer

In Figure 4.1 there are four psychrometers located at (4) located in the centers of four quadrant squares in the duct section to determine the average dry- and wet-bulb temperature, T_{an} and T_{wbn} . In Figure 4.2 there are four psychrometers at (13) to measure the average inlet dry- and wet-bulb temperature, T_{ai} and T_{wbi} and at (8) there are only two psychrometers to determine the average outlet dry- and wet-bulb temperature, T_{ao} and T_{wbo} .

For the process water there are three thermocouples installed in both the in- and outlet headers to measure the in- and outlet temperatures, T_{wi} and T_{wo} respectively. The deluge water has three thermocouples at (9) to measure the inlet

deluge water temperature, T_{dwi} , and eight thermocouples measure, $T_{dw,i}$ across the height of the bundle (20) to determine the temperature profile. Finally at (12) there are three thermocouples on the left-hand side deluge water collecting header and two in the right-hand side collecting header. The outlet deluge water temperature T_{dwo} , is the average of these five thermocouples. The mean deluge water temperature, T_{dwm} , is an average of the temperatures at position (20) which is necessary to determine the film convection heat transfer coefficient and the mass transfer coefficient. The sump deluge water temperature (15), T_{dws} , which is an average of three thermocouples, is used to determine the density of the water in the Venturi in order to determine the mass flow rate, m_{dw} . Redundancy is built into the temperature measurement to improve accuracy.

The thermocouples at (20), measuring the deluge water temperature profile, are 500 mm long and inserted in the side of the bundle with the thermocouple end right below the tube in the water film as shown in Figure 4.6.

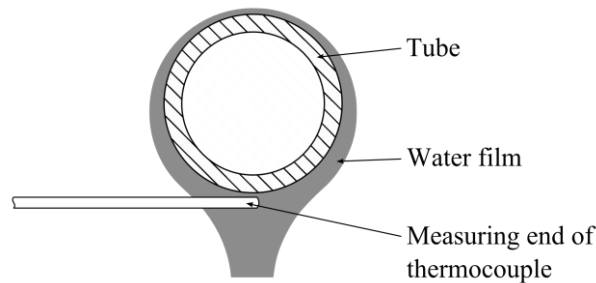


Figure 4.6: Thermocouple placement to measure the deluge water film temperature across the height of the tube bundle

Figure 4.7 shows a second configuration where the measuring technique is changed by slipping a small receptacle over the end of the thermocouple. This ensures that the thermocouple end is inundated by the deluge water thereby making the measurement more reliable. Figure 4.8 is a photo of this small receptacle.

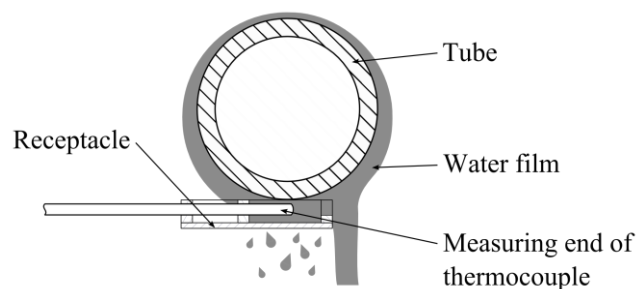


Figure 4.7: Schematic of the placement of the receptacle for the deluge water thermocouples



Figure 4.8: Photo of the receptacle for the deluge water thermocouples

4.3.2 Pressure

Figure 4.9 is a photo of the Endress+Hauser pressure transducers used to conduct the experiments. The three pressure transducers were calibrated with a Betz manometer. The pressure transducer indicated with (A) measures the pressure drop over the flow nozzles as indicated in Figure 4.1. Pressure transducers (B) and (C) both measure the pressure drop over the tube bundle.

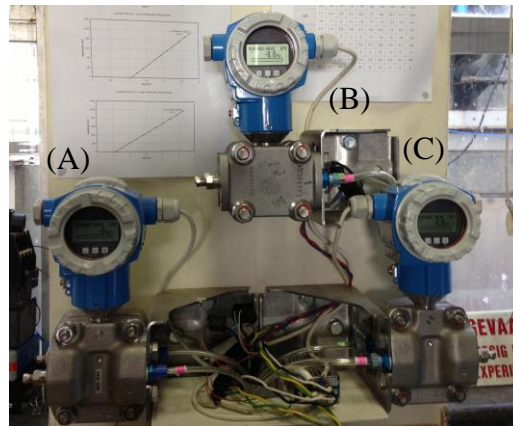
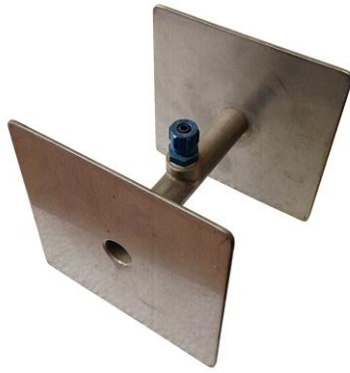


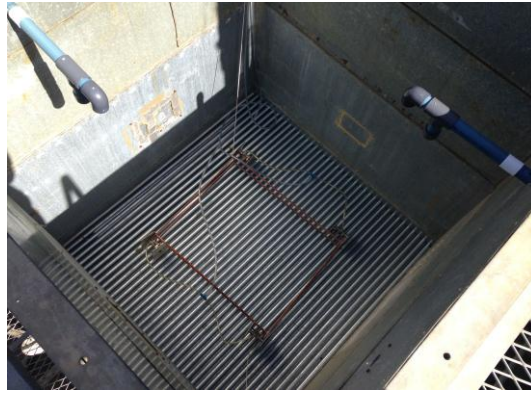
Figure 4.9: Pressure transducers

H-taps, as shown in Figure 4.10(a), are connected to the pressure transducers in Figure 4.9 with clear rubber tubes. These H-taps are used to measure the combined pressure drop over the tube bundle and the collecting troughs as indicated with (10) in Figure 4.2. Four H-taps are installed above the tube bundle and another four below the collecting troughs. A photo of the H-taps above the bundle is shown in Figure 4.10(b). In order to obtain the pressure drop over the tube bundle, the pressure drop over the collecting troughs is subtracted from the measured pressure drop.

Pressure transducers (B) and (C) are both connected to two H-taps above the tube bundle and two below the collecting troughs. Two H-taps are used for a specific pressure point in order to average out any local pressure discrepancies. The redundancy of the tube bundle pressure drop measurement ensures accuracy and helps to identify any measurement discrepancies that may be induced by loose connections of the rubber tubes or liquid in the tubes that connect the H-taps to the pressure transducers.



(a) H-tap



(b) H-taps in experimental setup

Figure 4.10: H-tap and H-tap in the experimental setup

The pressure drop over the Venturi flow measurement instrument is measured with a 4 – 20 mA output Foxboro pressure transducer which is calibrated with a mercury manometer. The atmospheric pressure is measured with a Thies Clima mercury column barometer located at the testing facility.

4.3.3 Flow rate

A Venturi flow meter as shown Figure 4.11 is used to measure the deluge water flow rate, m_{dw} . This Venturi is calibrated in a laboratory by varying the mass flow rate supplied by a pump while measuring the pressure drop over the Venturi and the time it takes to fill a tank of known volume. The discharge coefficient is obtained by correlating the calculated mass flow rate from the elapsed time to fill the tank, with the theoretical mass flow rate obtained from the pressure drop and the Bernoulli equation. The pressure drop is measured from the two pressure taps indicated in Figure 4.11.

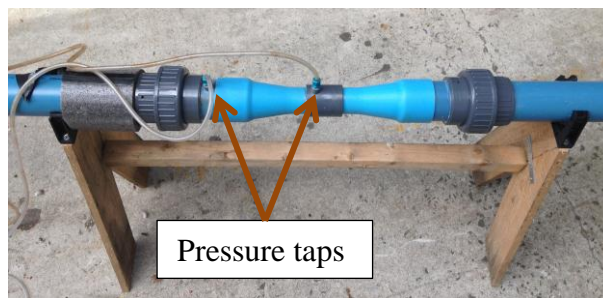


Figure 4.11: Installed Venturi flow meter

The volumetric flow rate of the process water is measured with an Endress+Hauser electromagnetic flow meter shown in Figure 4.12. The 4 – 20 mA output of this instrument is connected to the Agilent data acquisition system discussed in Section 4.5. Bertrand (2011) provides additional information on the equipment used.



(a) Measurement display



(b) Electromagnetic flow meter

Figure 4.12: Process water flow meter

4.4 Test procedure

Preparation starts with the heating of the 45 000 L tank of process water to a temperature of 50 °C. The following procedure is followed for a test.

1. The psychrometer reservoirs are filled with distilled water and the cotton wicks are thoroughly wetted.
2. The wet-bulb temperatures are logged to check for agreement in measurements.
3. The psychrometer fans are switched on to effectuate air flow in the psychrometers. The wet-bulb temperatures are again checked for accuracy. Individual wet-bulb temperature measurements deviating by less than 0.2 °C from the average are deemed satisfactory (Bertrand, 2011).
4. The process water is set to the desired fixed flow rate and kept constant for all the tests.
5. The deluge water pump is switched on to circulate and heat the deluge water.
6. With deluge water temperature approaching the prior calculated stabilization temperature, the fan is switched on to supply air flow to the counter-flow test section.
7. The deluge water flow rate is varied from 1.5 kg/m²s to 3.5 kg/m²s in increments of 0.7 kg/m²s while the air and process water flow rates are kept constant.
8. The data is logged once the inlet and outlet deluge water temperature stabilizes to within ± 0.5 °C at the given set points.
9. The air flow rate is varied between 1 – 2.8 kg/m²s in increments of 0.6 kg/m²s and with each new air flow set point steps 7 to 9 are repeated. This totals to 16 tests.

Tests starts at the highest deluge water and the lowest air flow rates and ends at the lowest deluge water and the highest air flow rates. This order is reversed in

successive tests to determine whether there are any system transients captured in the experimental data.

4.5 Data acquisition and processing

The various thermocouples, pressure transducers and flow meters are connected to an Agilent 34972A LXI Data Acquisition system with three 34901A 20 Channel Multiplexer Cards. The channels of the multiplexers are configured to measure the DC voltage output from the pressure transducers, the current output from the electromagnetic flow meter and the pressure transducer of the Venturi flow meter, and temperature for all the Type T thermocouples.

An Excel VBA program has been written to log all the channel signals obtained from the Agilent Data Acquisition system. Figure 4.13 is a screen-shot of this program. This program directly imports the data into cells in Excel while the experiment is running. This allows calculations of parameters, such as the mass flow rates and energy balances with the use of the thermo-physical properties as defined in Kröger (2004) in real time. These parameters enable the user to verify whether the system has stabilized in steady state or whether the system is still in a transient phase.

The model has been configured to scan all the channels every five seconds for one minute. New data points in the first thirty seconds are logged as an average of the scanned points. After thirty seconds new data points are logged as a moving average of the scanned point and the previous five points. The data is saved after steady state conditions are met. The mass and film heat transfer coefficients along with the air-side loss coefficient can be determined from the data for various air- and deluge water mass flow rates and deluge water temperatures.

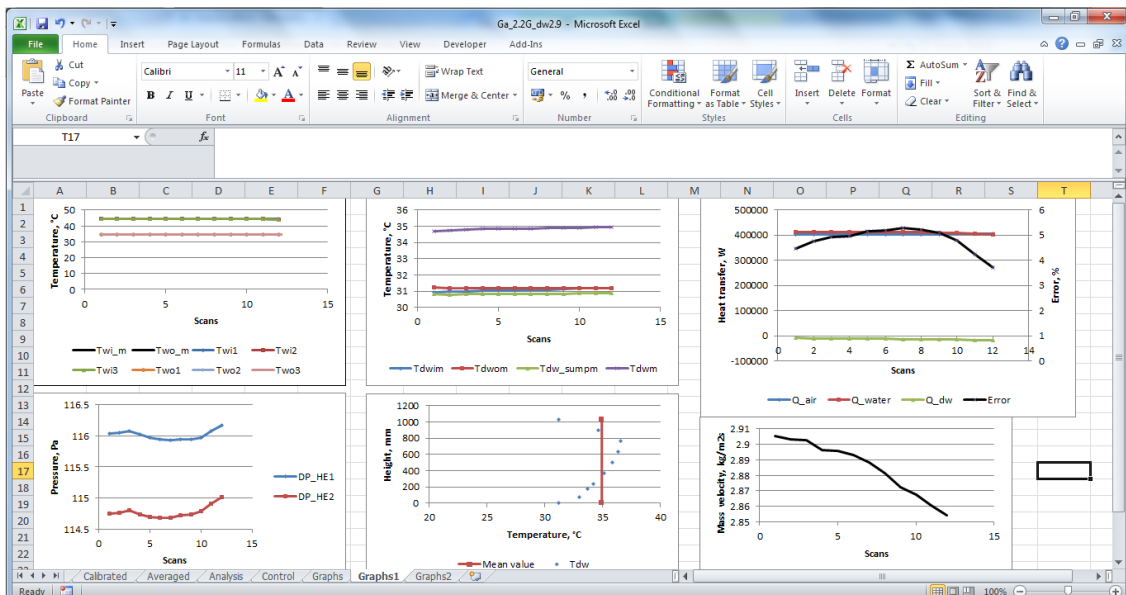


Figure 4.13: Screen-shot of the data logging software developed in Excel

5 Results and discussions

5.1 Introduction

This section details the discussion of results obtained from the tests conducted to obtain the bundle performance characteristics for wet and dry operation.

5.2 Water distribution and collecting trough system performance characteristics

The performance characteristics determined from test data include the effect of the water distribution and collecting trough system. To determine the heat and mass transfer coefficients and pressure drop of only the bundle, the spray and trough transfer characteristics and pressure drop must be subtracted from the experimental values. Tests are therefore conducted to determine the water distribution and collecting system performance characteristics.

5.2.1 Trough pressure drop characteristics for dry operation

Figure 5.1 presents the measured pressure drop across the water collecting troughs for dry operation, plotted as a function of the dry air mass velocity. The data is correlated by Eq. (5.1).

$$\Delta p_{tr} = 2.583G_a^{1.7402} \quad (5.1)$$

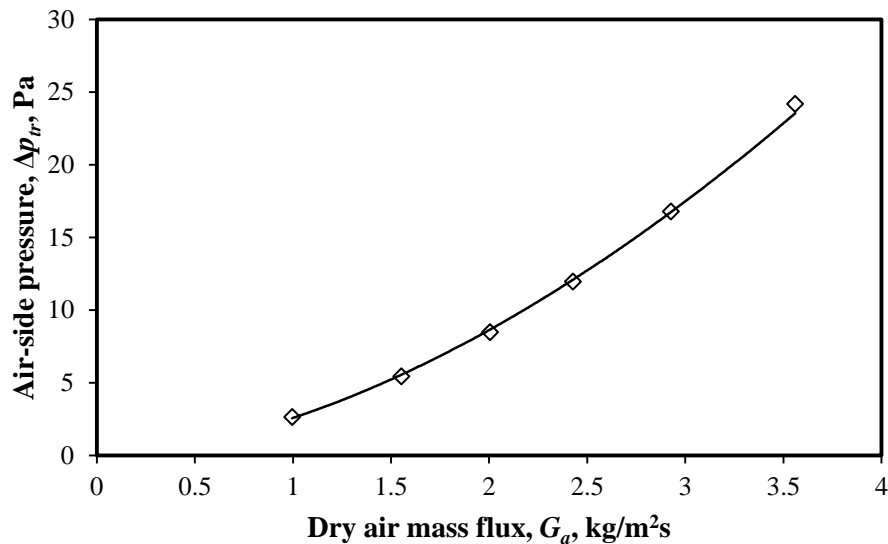
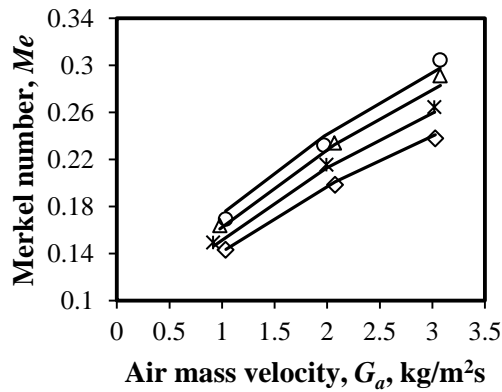


Figure 5.1: Air-side pressure drop over the collecting troughs for dry operation

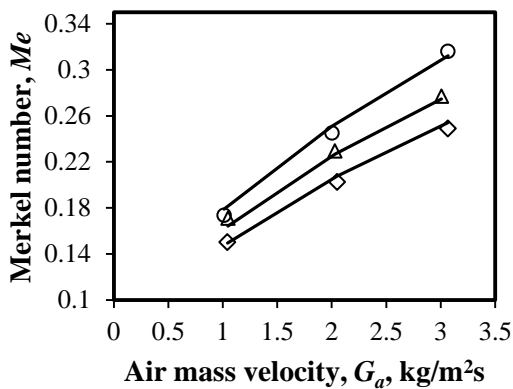
5.2.2 Spray and trough system transfer and trough pressure drop characteristics for wet operation

Tests are conducted without the tube bundle installed to quantify the combined Merkel numbers of the deluge water spray system, rain zone and collecting troughs, since they account for some of the heat and mass transfer and pressure drop when the bundle is installed. The spray frame is set at 350 mm above the collecting troughs which is representative of the combined spray zone and rain zone above and below the tube bundle. A test comprises three air flow rates and four water flow rates and is repeated three times to determine the effect of water inlet temperature. The experimentally determined Merkel numbers are shown for tests 1 to 3 in Figure 5.2(a) to (c).



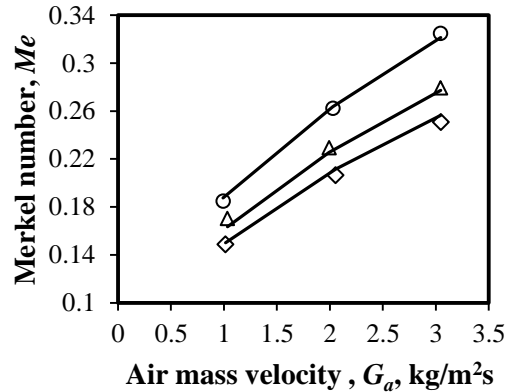
- $G_{dw} = 1.5 \text{ kg/m}^2\text{s}$ △ $G_{dw} = 1.8 \text{ kg/m}^2\text{s}$ ✕ $G_{dw} = 2.1 \text{ kg/m}^2\text{s}$
 ◇ $G_{dw} = 2.5 \text{ kg/m}^2\text{s}$ — Correlation

(a) Thermal trough test 1; $41.1 < T_{wi} < 42.4 \text{ }^\circ\text{C}$



- $G_{dw} = 1.5 \text{ kg/m}^2\text{s}$
 ◇ $G_{dw} = 2.5 \text{ kg/m}^2\text{s}$

(b) Thermal trough test 2; $36.6 < T_{wi} < 40 \text{ }^\circ\text{C}$



- △ $G_{dw} = 2 \text{ kg/m}^2\text{s}$
 — Correlation

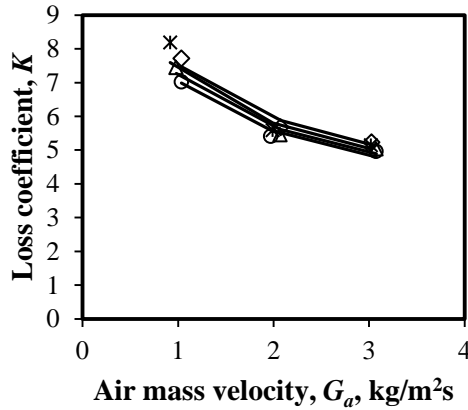
(c) Thermal trough test 3; $35.7 < T_{wi} < 36.5 \text{ }^\circ\text{C}$

Figure 5.2: Merkel number of the system without a bundle installed

The different deluge water mass velocities are indicated in the legend for each test. Equation (5.2) is an empirical relation of the Merkel number obtained by regression of the data.

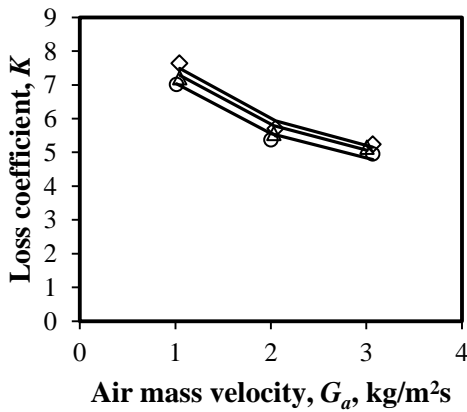
$$Me = 1.2331G_a^{0.4833}G_w^{-0.4468}T_{wi}^{-0.4726} \quad (5.2)$$

Figure 5.2(a) is a representation of Test 1 which was the first of the three tests. This test has four water mass velocity set points at 1.5, 1.8, 2.1 and 2.5 kg/m²s and three air mass velocity set points at 1, 2 and 3 kg/m²s over a water inlet temperature range of 41.1 < T_{wi} < 42.4 °C.



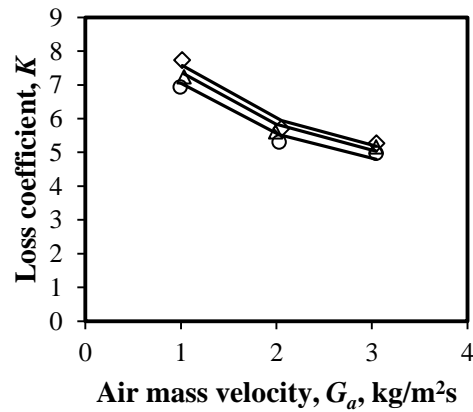
- $G_{dw} = 1.5 \text{ kg/m}^2\text{s}$ △ $G_{dw} = 1.8 \text{ kg/m}^2\text{s}$ ✕ $G_{dw} = 2.1 \text{ kg/m}^2\text{s}$
 ◇ $G_{dw} = 2.5 \text{ kg/m}^2\text{s}$ — Correlation

(a) Thermal trough test 1; 41.1 < T_{wi} < 42.4 °C



- $G_{dw} = 1.5 \text{ kg/m}^2\text{s}$
 ◇ $G_{dw} = 2.5 \text{ kg/m}^2\text{s}$

(b) Thermal trough test 2; 36.6 < T_{wi} < 40 °C



- △ $G_{dw} = 2 \text{ kg/m}^2\text{s}$
 — Correlation

(c) Thermal trough test 3; 35.7 < T_{wi} < 36.5 °C

Figure 5.3: Loss coefficient of the collecting troughs without the bundle installed

Figure 5.2(b) and (c) are the second and third test respectively. The deluge water mass velocities for these two tests were 1.5, 2, 2.5 kg/m²s and 1, 2 and 3 kg/m²s for air. Each curve is for a set deluge water mass velocity. For Test 2 and 3 the water inlet temperature range is 36.6 < T_{wi} < 40 °C and 35.7 < T_{wi} < 36.5 °C respectively. The measured pressure drop over the collecting troughs is presented in the form of a loss coefficient in Eq. (5.3) and depicted in Figure 5.3.

$$K_{tr} = 6.6154G_a^{-0.34563}G_w^{0.150514} \quad (5.3)$$

The following correlation yields the pressure drop over the collecting troughs during wet operation as indicated in Figure 5.4,

$$\Delta p_{tr} = 2.8334G_a^{1.6407}G_{dw}^{0.16439} \quad (5.4)$$

which is valid over the range 0.9 ≤ G_a ≤ 3.1 kg/m²s and 1.5 ≤ G_{dw} ≤ 2.6 kg/m²s.

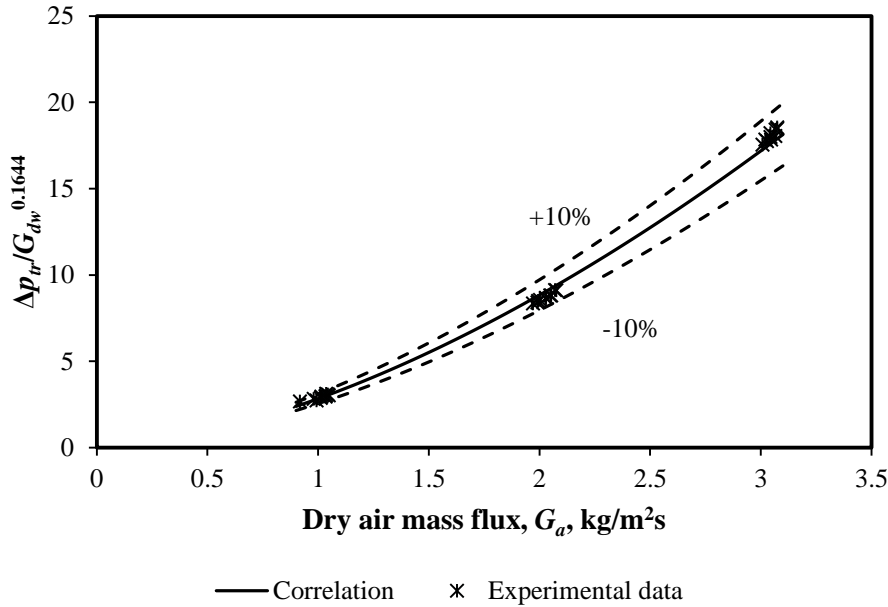


Figure 5.4: Pressure drop over the collecting troughs during wet operation

5.3 Tube bundle performance characteristics for wet operation

5.3.1 Operating strategy and parameter ranges

Table 5.1 displays the operating ranges for all the parameters during the execution of wet experiments. From the first test it was noted that flooding of the tube bundle occurs at G_c = 6.1 kg/m²s with G_c the critical air mass velocity through the bundle based on the minimum flow area. Flooding occurs when the air velocity is sufficient to suspend the deluge water in the bundle. Heyns (2008) reports flooding occurring at G_c = 7.4 kg/m²s. The point of flooding is highly dependent

on the bundle geometry and is best avoided, since the increased residence time of the water in the bundle increases the deluge water temperature which increases the water evaporated and the probability of scaling. The flow rate in the successive tests is adjusted to avoid flooding. The deluge water flow rate range is determined by using the lower limit for uniform wetting of tubes as reported by Niitsu et al. (1967) which is $\Gamma_m/d_o = 0.8 \text{ kg/m}^2\text{s}$ or $G_{dw} = 1.5 \text{ kg/m}^2\text{s}$ and the full capacity of the deluge water pump which was found to be at $G_{dw} = 3.5 \text{ kg/m}^2\text{s}$.

Table 5.1: Operating ranges for all the parameters during the wet tests

Parameter	Symbol	Range	Units
Inlet dry-bulb temperature	T_{ai}	14.9 – 21.4	°C
Inlet wet-bulb temperature	T_{wbi}	12.5 – 17.1	°C
Outlet dry-bulb temperature	T_{ao}	28.6 – 40.5	°C
Outlet wet-bulb temperature	T_{wbo}	28.3 – 40.5	°C
Inlet process water temperature	T_{wi}	37.1 – 48.4	°C
Outlet process water temperature	T_{wo}	29.9 – 41.5	°C
Deluge inlet temperature	T_{dwi}	27.3 – 39.3	°C
Deluge outlet temperature	T_{dwo}	26.7 – 38.7	°C
Deluge sump temperature	T_{dws}	26.8 – 38.5	°C
Mean deluge water temperature	T_{dwm}	29.1 – 40.9	°C
Pressure over the Venturi	Δp_v	3805.3 – 20952.5	Pa
Pressure drop over the nozzles	Δp_n	47.4 – 398	Pa
Pressure drop over the tube bundle	Δp_{tb}	25.1 – 208.5	Pa
Atmospheric pressure	p_a	100100 – 100430	Pa
Process water mass flow rate	m_w	10 – 10.3	kg/s
Air mass flow rater	m_{avi}	2.2 – 6.5	kg/m ² s
Dry air mass flux	G_a	1 – 2.8	kg/m ² s
Critical dry air mass flux	G_c	2 – 5.8	kg/m ² s
Inlet deluge water mass flow rate	m_{dwi}	3.3 – 7.8	kg/s
Deluge water mass flux	G_{dwi}	1.5 – 3.5	kg/m ² s

Figure 5.5 depicts the energy balances of the experiments calculated with Eq. (3.5). The energy balances are acceptably within $\pm 5\%$ except for two tests. The figure also illustrates that the cooling performance of the deluged tube bundle is more than the 150 kW heating capacity of the diesel boiler. A constant process water inlet temperature can therefore not be maintained by means of the boiler alone. A large tank is therefore used as a heat storage device. It is however found that this tank is too small to maintain a constant water temperature resulting in the water temperature dropping steadily during testing. The inlet process water temperature decreased continuously from 48 °C and the data was logged on quasi-equilibrium states. Tests are conducted at different air and deluge water flow rates while keeping the process water flow rate constant. The numbers in Table 5.2 to 5.4 illustrate the order in which different flow rate combinations were tested. To

verify the repeatability of the tests due to changing inlet process water temperature, the order of the flow rate combinations is reversed for test 3.

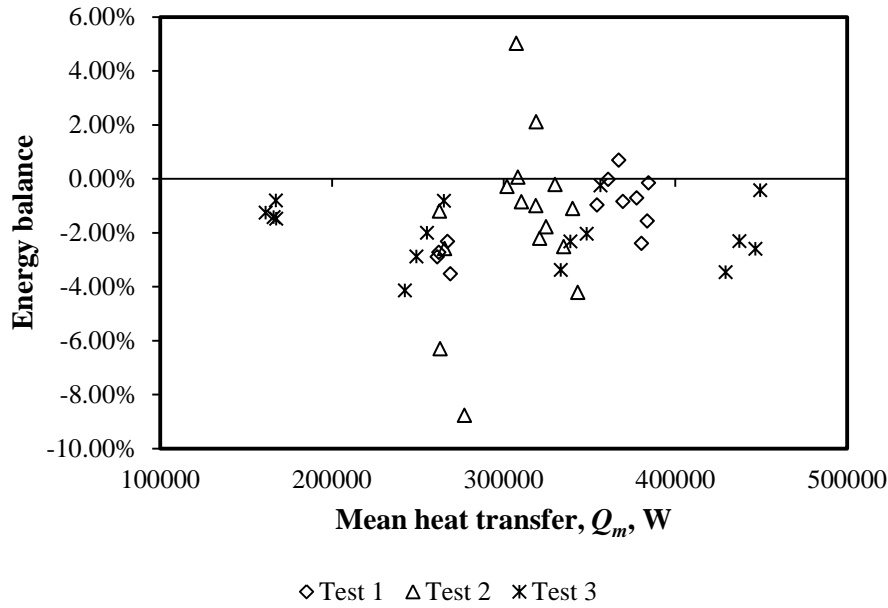


Figure 5.5: Energy balances of the tests of the deluge evaporative cooler

Table 5.2: Wet thermal test 1 order

		G_a		
		1	2	2.5
G_{dw}	1.5	4	8	12
	1.75	3	7	11
	2	2	6	10
	2.5	1	5	9

Table 5.3: Wet thermal test 2 order

		G_a			
		1	1.6	2.2	2.8
G_{dw}	1.5	4	8	12	16
	2.2	3	7	11	15
	2.9	2	6	10	14
	3.5	1	5	9	13

Table 5.4: Wet thermal test 3 order

		G_a			
		1	1.6	2.2	2.8
G_{dw}	1.5	13	9	5	1
	2.2	14	10	6	2
	2.9	15	11	7	3
	3.5	16	12	8	4

From Figure 5.5 it can be observed that the heat transfer range is greater for test 3 compared to tests 1 and 2. This is due to the high inlet water temperature with the high air flow rate yielding high heat transfer rates. As the inlet water temperature decreased during the experiment, the inlet temperature was lower for the lower air flow rates yielding lower heat transfer. However, during tests 1 and 2 there was a

high inlet water temperature for the low air flow rates and a low inlet water temperature for the high air flow rates. This yielded heat transfer more or less in the same order of magnitude as indicated by the distribution of all the data points in Figure 5.5.

5.3.2 Sensitivity of the transfer characteristics to the mean deluge water temperature

In the Effectiveness-NTU method described in Chapter 3, the constant deluge water temperature is asymptotically bound by the saturated outlet air temperature and the outlet process water temperature. If the measured mean deluge water temperature falls outside these asymptotes, the transfer characteristics will be incalculable. This measured mean was greater than the outlet process water temperature for the flooded tube bundle case ($G_a = 3$ or $G_c = 6.1 \text{ kg/m}^2\text{s}$) and yielded unsatisfactory results. This air flow rate is therefore discarded from the analysis and the air flow range is adapted.

This sensitivity of the transfer characteristics to the mean deluge water temperature is investigated by varying only the deluge water temperature for combination 5 in Table 5.2 ($G_a = 2$ and $G_{dw} = 2.5 \text{ kg/m}^2\text{s}$). All other parameters are kept constant. The mass and film heat transfer coefficients are determined for this set point using the method of analysis of Chapter 3 and is compared to the correlations of Niitsu et al. (1967), Mizushina et al. (1967) and Parker & Treybal (1961) given in Appendix A. This set point is chosen because it is the point where all three authors' correlations are within or very close to the specified applicable ranges. The coefficients are plotted with the corresponding calculated mean deluge water temperature in Figure 5.6(a) and (b). These correlations do not fall exactly on the curve because the bundle geometries of the three authors are different to the current bundle and there is uncertainty due to scatter. For comparison, the mass and film heat transfer coefficients of the current analysis are also incorporated in the graphs. Figure 5.6(a) illustrates how the mass transfer coefficient decreases with an increase of the deluge water temperature between the two asymptotes, while Figure 5.6(b) depicts how the deluge water film heat transfer coefficient increases with an increase of the deluge water temperature.

The main focus of this investigation is to note that each correlation predicts a different mean deluge water temperature even though they are still close. This difference in the mean deluge water temperature determines the contribution of the different resistances in series as depicted in Figure 3.3 to the total resistance. Convective resistance must decrease if the mass transfer resistance increases for the same heat transfer to take place and vice versa. This discrepancy in the mean deluge water temperature may lie in the measurement techniques of the various authors and how many thermocouples were used to measure the vertical deluge water temperature profile over the height of the bundle.

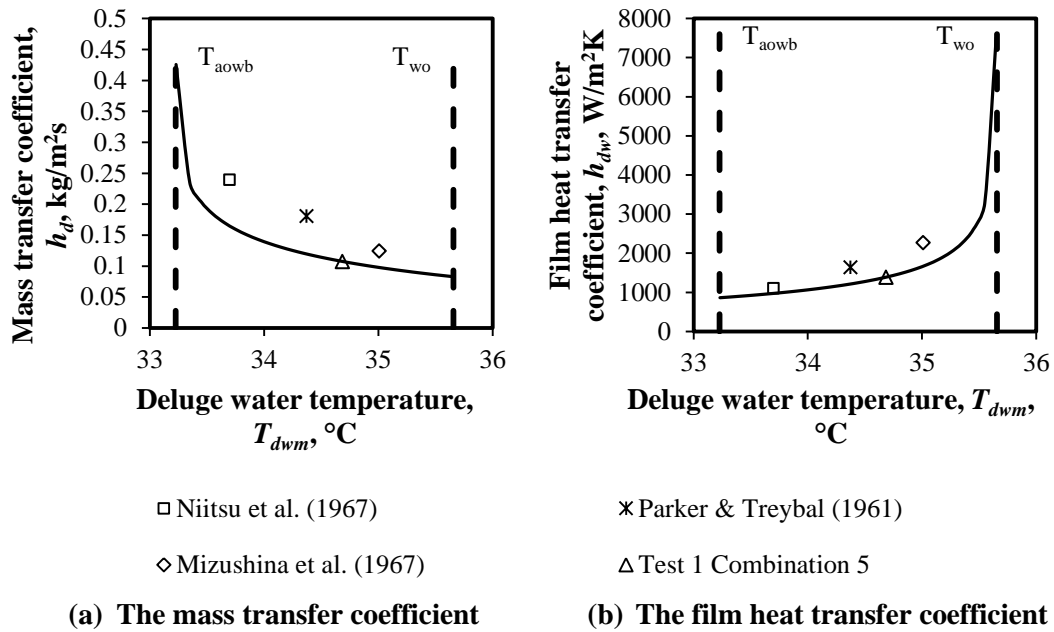


Figure 5.6: The influence of deluge water temperature on the mass and film heat transfer coefficient

Figure 5.7 shows the vertical deluge water temperature profiles over the height of the bundle along with the mean deluge water temperature for three cases representative of the range of flow rates tested. These profiles indicate the main heat transfer processes through the tube bundle. These are the profiles measured with the measuring techniques depicted in Figure 4.6. The cold and unsaturated air enters the tube bundle at the bottom of the bundle and is heated by the warm deluge water to the point of maximum deluge water temperature, above which, latent heat transfer is the main heat transfer mechanism. Due to the unique geometry of the lower part of the heat exchanger, the small rain zones may affect additional cooling of the deluge water and splashing of the deluge water over the tubes may yield these profiles. For all the test cases the maximum deviation from the mean deluge water temperature was always less than 3°C .

Figure 5.8 shows the measured deluge water temperature profile through the height of the bundle with the second measuring technique implemented as illustrated in Figure 4.7. It is clear that the measured profiles do look similar to the profiles shown in Figure 5.7, except for the lower part of the bundle where the small rain zones perhaps did not form a water film over the tubes. These profiles agree closer to the measured profiles of literature with a more uniform parabolic shape. This is therefore the preferred measuring technique to be implemented.

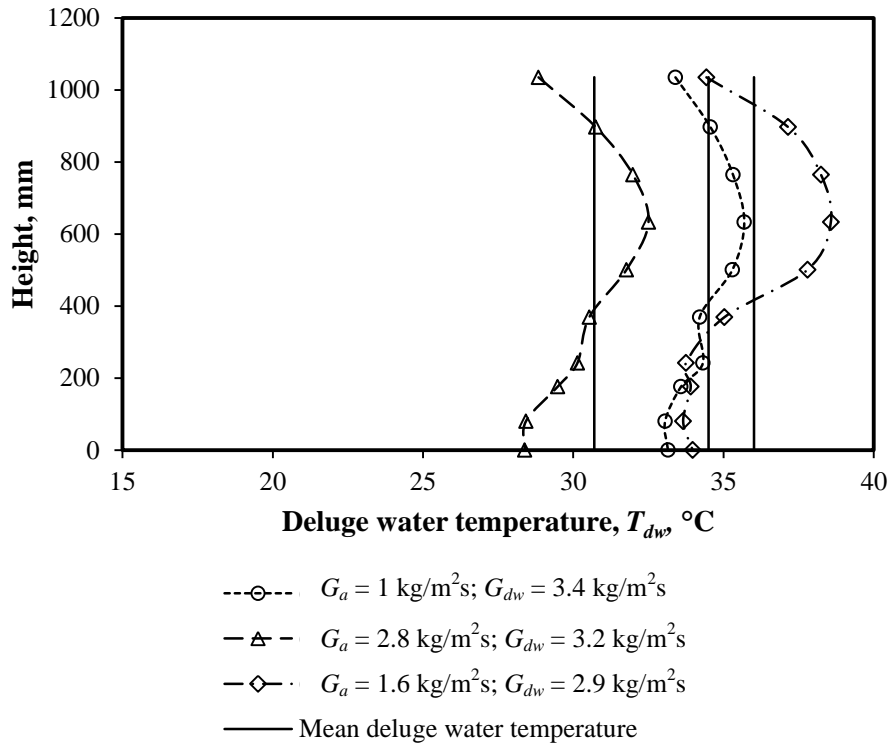


Figure 5.7: Measured vertical deluge water temperature profiles over the height of the tube bundle with first measuring technique

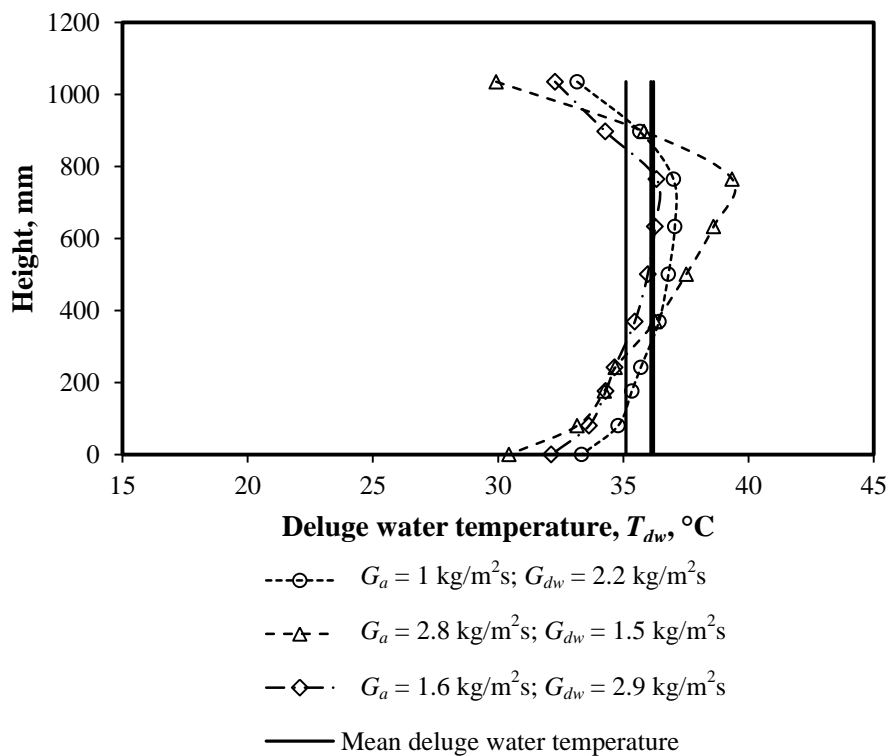


Figure 5.8: Measured vertical deluge water temperature profiles over the height of the tube bundle with second measuring technique

5.3.3 Correlation predictions of performance

The data set of test 1 of the three data sets is used to investigate and compare the measured bundle performance with the performance predicted by using the correlations of Mizushina et al. (1967), Niitsu et al. (1967) and Parker & Treybal (1961). The above correlations are extrapolated if the current air- and deluge water flow rates are outside the ranges tested by the various researchers. In Figure 5.9, the deviation in heat transfer is plotted at various air flow rates and which is defined as:

$$\delta Q = \frac{Q_{corr} - Q_{ex}}{Q_{ex}} \quad (5.5)$$

where Q_{corr} is the heat transfer obtained using the correlation from literature and Q_{ex} is the heat transfer that was calculated from the experimental results.

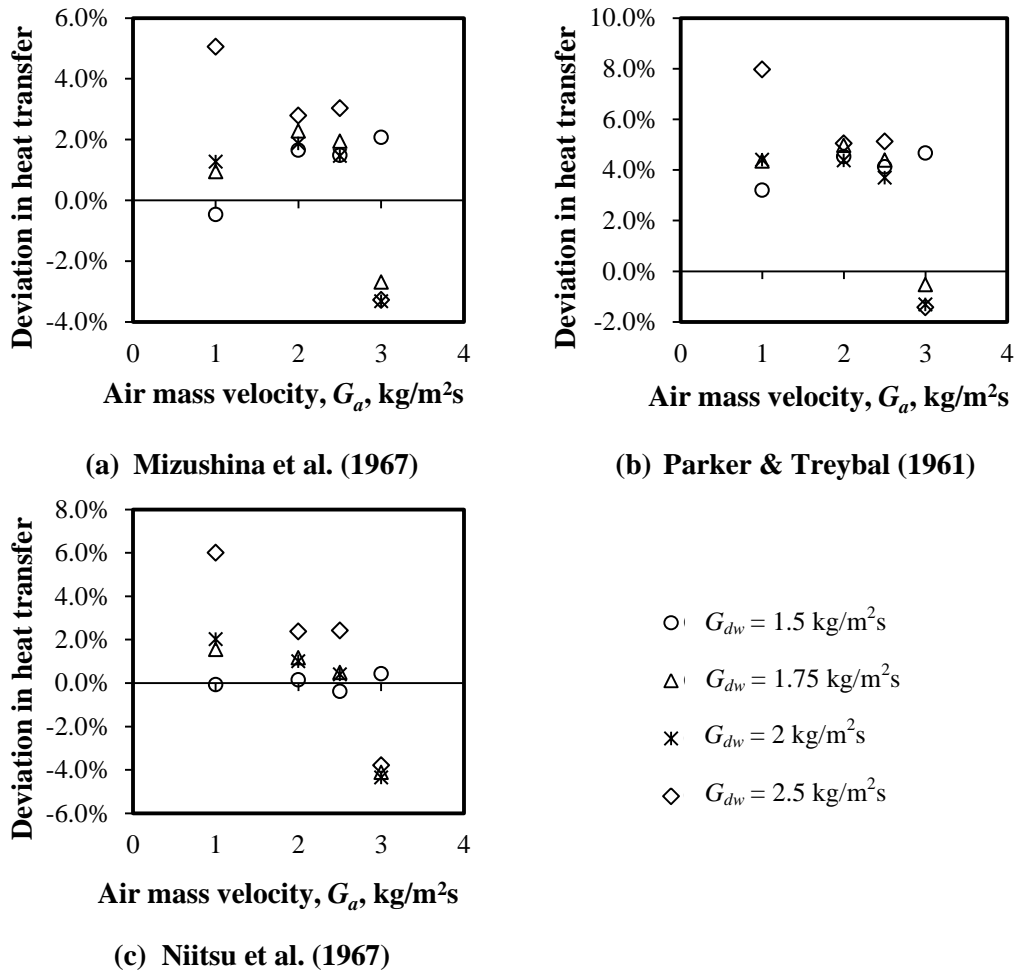


Figure 5.9: Deviations between predicted thermal performance using performance characteristics from literature and measured performance for different air- and deluge water flow rates

The process water heat transfer is used as the reference for the experimental heat transfer. It is clear from the analysis that the performance of the tube bundle can be predicted to within $\pm 5\%$ by using the correlations of these three authors, if their own heat and mass transfer coefficients are used together and not mixed. There is only one case outside this range because the mean deluge water temperature is close to one of the two asymptotes. The heat transfer for the flooding flow rate ($G_a = 3 \text{ kg/m}^2\text{s}$) can even be predicted but is underestimated while the heat transfer is overestimated for all the other flow rates by the correlations. Therefore even though the film heat transfer coefficient may differ by as much as 39.5% and the mass transfer coefficient by 34.7% as indicated in Figure 5.6, all three correlations can be used to predict this specific bundles performance with reasonable accuracy.

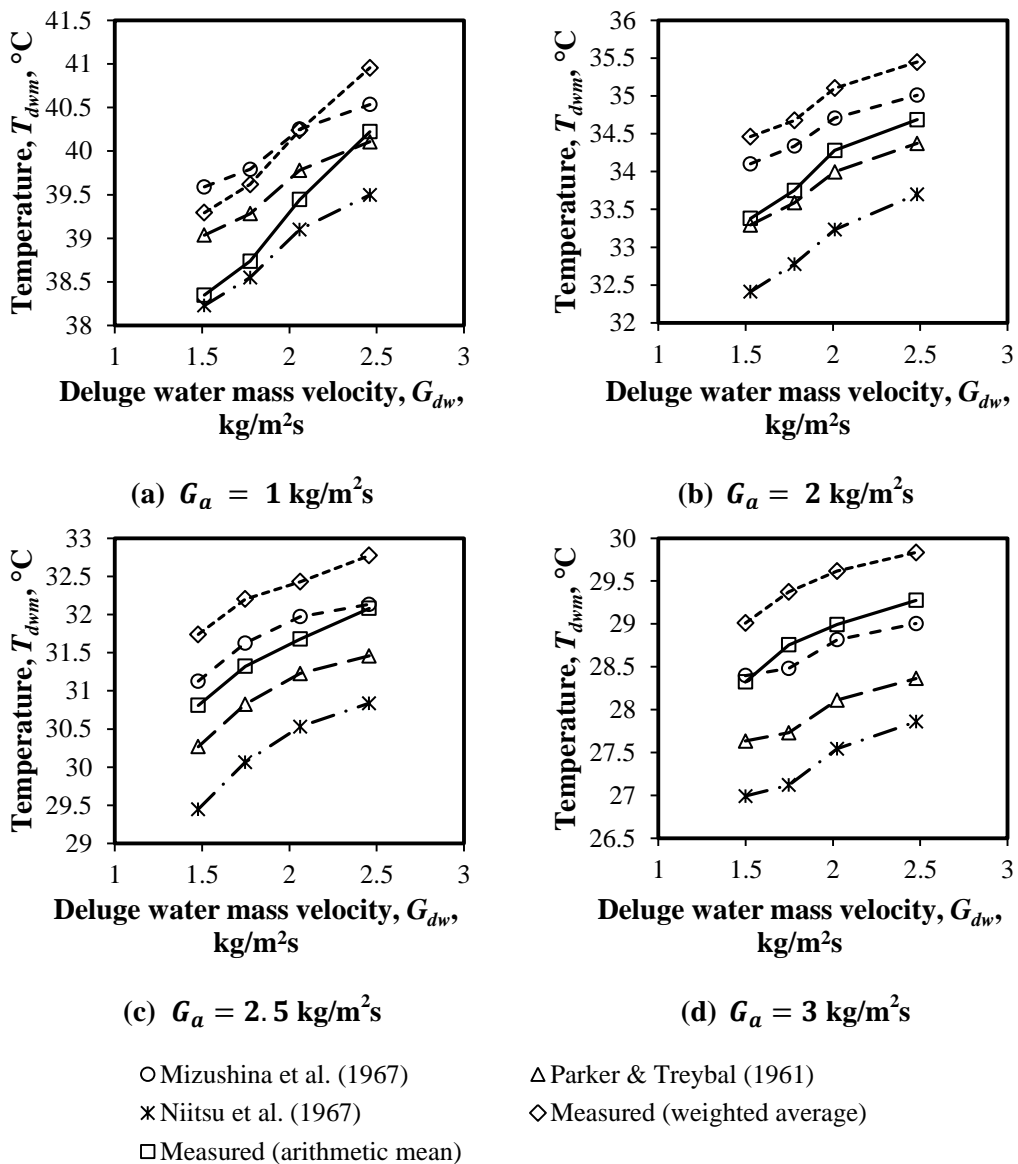


Figure 5.10: Converged mean deluge water temperature obtained from Effectiveness-NTU method and measured mean deluge water temperature

Figure 5.10 illustrates the converged mean deluge temperatures from the correlations and the mean deluge water temperature from the experiments. The use of a weighted mean deluge water temperature was investigated, since the resolution of the deluge water temperature profile may be low. The weighted mean deluge water temperature is defined as the summation of all the temperatures times the amount of tube rows adjacent to the specific thermocouples divided by the total number of tube rows.

$$T_{dwm} = \frac{1}{25} \left(4 \sum_{i=1}^5 T_{dw,i} + 2 \sum_{i=6}^7 T_{dw,i} + T_{dw,8} \right) \quad (5.6)$$

This weighted mean was found to be above the mean deluge water temperature of the other authors. Mizushina et al. (1967) and Heyns (2008) reported using the arithmetic mean deluge water temperature in their analysis and using this in the current analysis did seem to be more consistent with their measured mean deluge water temperature. By taking the stabilized inlet deluge water temperature as the mean deluge water temperature as done by Hasan & Sirén (2003) yielded inconclusive results because the inlet deluge water temperature is not between the two asymptotes that would yield conclusive results.

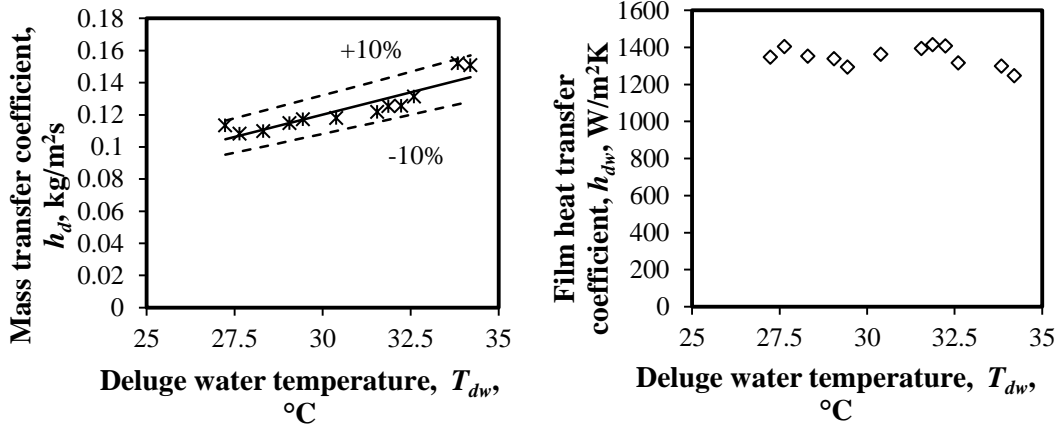
5.3.4 Transfer characteristics from the experimental results

As stated earlier, the process water inlet temperature could not be kept constant during the testing of the tube bundle and was decreasing at slow rate. As the process water temperature is decreasing, the mean deluge water temperature will also decrease. The effect of this on the transfer coefficients is investigated by setting $G_a = 2.5 \text{ kg/m}^2\text{s}$ and $G_{dw} = 1.75 \text{ kg/m}^2\text{s}$. These flow rates are the proposed flow rates for the hybrid dephlegmator.

Figure 5.11 depicts the result of this study and the mass transfer coefficient was found to decrease with a decrease in the mean deluge water temperature with the various flow rates kept constant. The film heat transfer coefficient shows an upward trend with a decreasing deluge water temperature but due to severe scatter no correlation could be drawn from this data set. A linear curve seems to fit the data quite well for the mass transfer coefficient and is,

$$h_d = 5.547 \times 10^{-3} T_{dwm} - 4.623 \times 10^{-2} \quad (5.7)$$

with $R^2 = 0.827$ and T_{dwm} in °C. Niitsu et al. (1967) and Parker & Treybal (1961) found the mass transfer coefficient to be only a function of the air mass flow rate through the minimum flow area. The inlet process water temperature was however kept constant during the tests conducted by Parker & Treybal (1961). The publication of Niitsu et al. (1967) is only available in Japanese making it difficult to verify this information.



(a) Mass transfer coefficient

(b) Film heat transfer coefficient

Figure 5.11: The influence of deluge water temperature on the bundle performance characteristics

After the temperature effect has been isolated a correlation is developed on the three data sets of wet tests. Figure 5.12 is the depiction of the mass transfer correlation which is defined as,

$$h_d = \frac{0.23603(5.547 \times 10^{-3}T_{dwm} - 4.623 \times 10^{-2})G_c^{0.86938}}{\left(\frac{\Gamma_m}{d_o}\right)^{0.41406}} \quad (5.8)$$

with $R^2 = 0.924$. This correlation has a similar shape to Mizushina et al. (1967) except for the additional linear temperature dependence and Mizushina et al. (1967) expressing the flow rates as Reynolds numbers. It may be noted that the scatter for the mass transfer coefficient increases at the lower air mass flow rates because the mean deluge water temperature is approaching the lower asymptote which is the saturated outlet air temperature.

The deluge film heat transfer coefficient was also found from the three data sets of wet tests and the correlation for this data is expressed as,

$$h_{dw} = 615.056 \left(\frac{\Gamma_m}{d_o}\right)^{0.58903} G_c^{0.530042} \quad (5.9)$$

and Figure 5.13 is the representation of the deluge water film heat transfer coefficient and the correlation. The scatter seems to increase at higher air flow rates because the mean deluge water temperature is approaching the upper asymptote which is the outlet process water temperature.

In both the mass and film heat transfer coefficient calculations the source of scatter may also be due to the fact that the system was logged on these quasi-equilibrium states with the deluge water flow rate slowly decreasing, since water is evaporating and the decision was made not to fill the tank up with make-up

water which may be at a different temperature. The process water temperature was also decreasing but this effect was isolated as stated earlier. Finlay & Harris (1984) found that correlations for the heat and mass transfer with scatter of perhaps $\pm 30\%$ are not excessive for two-phase turbulent flow. This was again confirmed by Hasan & Sirén (2002).

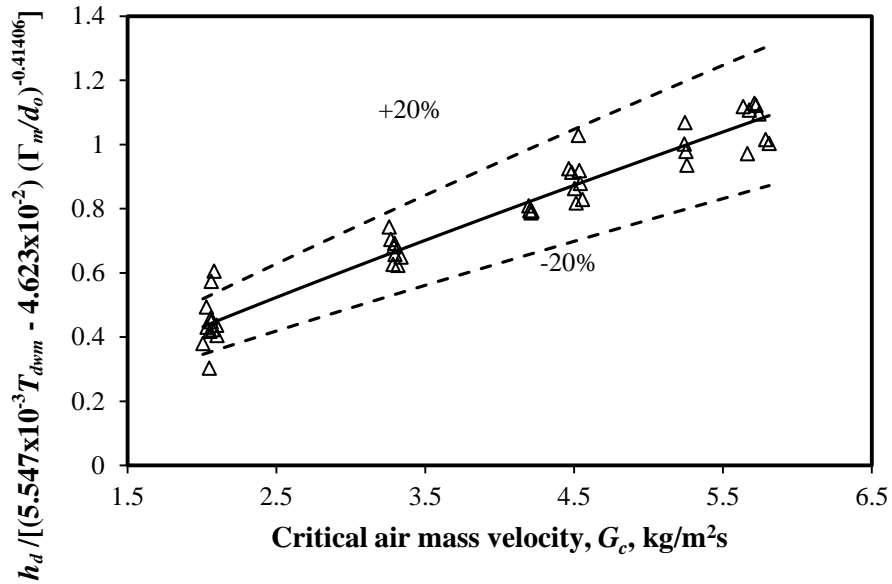


Figure 5.12: Mass transfer coefficient as a function of the critical air mass velocity through the bundle

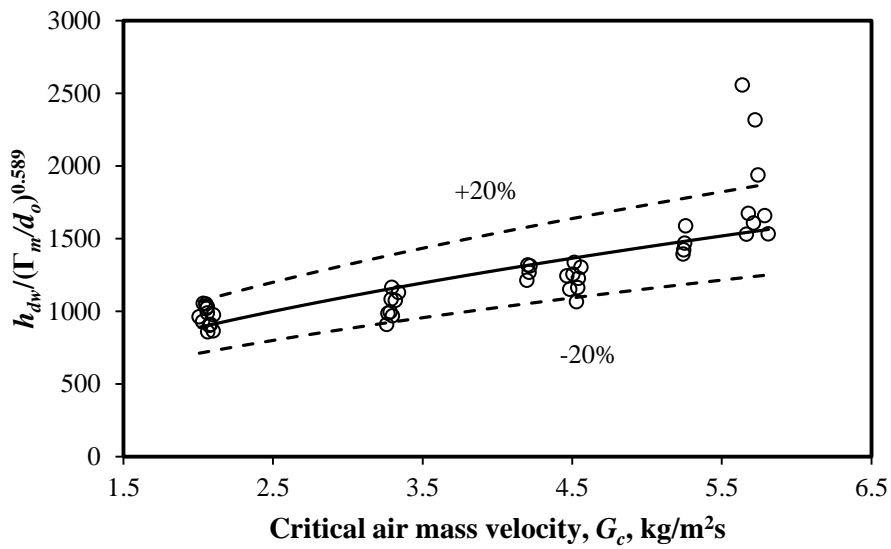


Figure 5.13: Deluge film convective heat transfer coefficient as a function of the critical air mass velocity through the bundle

Figure 5.14 shows the result of implementing Eqs. (5.8) and (5.9) to predict the outlet conditions and the performance of the deluge bundle and the results seem to be within 3% of the measured results which is considered sufficient.

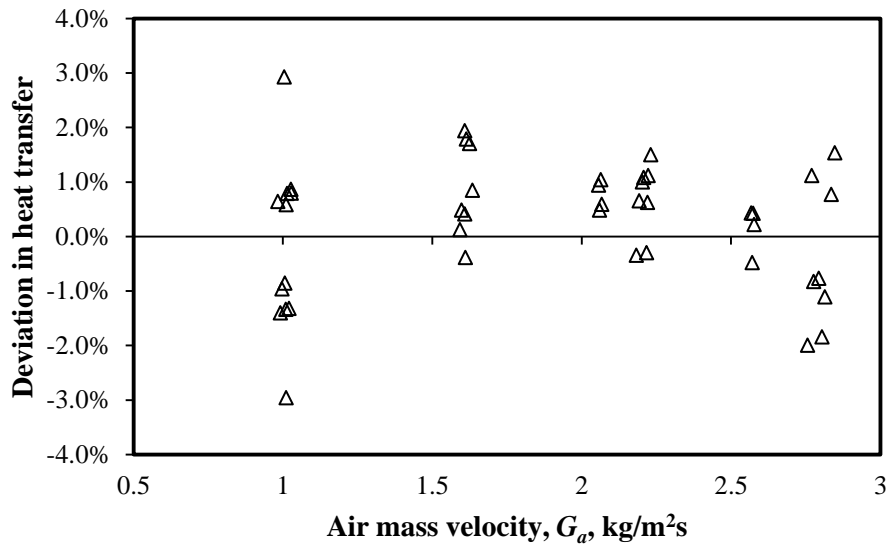


Figure 5.14: The heat transfer prediction with the Effectiveness-NTU method by using the obtained correlations for the mass and film heat transfer coefficients

The correlations of Mizushina et al. (1967) was used in prior designs of the tube bundle and Figures 5.15 and 5.16 show comparisons of these mass and heat transfer coefficients. The current correlation for the mass transfer coefficient is a function of deluge water temperature, air and deluge water flow rate, while the correlation of Mizushina et al. (1967) is only of air and deluge water flow rate. Mizushina’s mass transfer coefficient shown in Figure 5.15 increases with increasing air and deluge flow rate, while the current correlation increases with increasing air flow rate but decreases with increasing deluge water flow rate. The contribution of the current correlation at higher deluge water flow rates is lower compared to the correlation of Mizushina et al. (1967).

Figure 5.16 depicts a comparison of the film heat transfer coefficient of Mizushina et al. (1967) and the coefficient of the current study. The current correlation is a function of the air and deluge water flow rate and increases as both flow rates increase, while Mizushina’s correlation increase with an increase in deluge water flow rate. Mizushina’s correlation is also only a function of deluge water flow and is higher compared to film heat transfer coefficients of the current study at all air flow rates. This clarifies why Mizushina et al. (1967) overestimates the performance of the bundle in this study.

The different trends noted in Figures 5.15 and 5.16 are mainly due to the difference in the number of tube rows between the bundles of the current study and that of Mizushina et al. (1967). The current bundle has more than double the

amount of tube rows than the bundle tested by Mizushina et al. (1967). The smaller bundle of Mizushina et al. (1967) meant that a constant inlet process water temperature was possible and the mean deluge water temperature never came close to the two asymptotes during experiments. At high flow rates during the current study and especially high deluge water flow rates, supersaturated outlet conditions are recorded. Since the analysis is based on saturated outlet conditions, some of the mass transfer is unaccounted for and therefore underestimated. This can be a possible explanation for the contrasting trends of the mass transfer coefficient in Figure 5.15. It also explains the steeper gradient of the film heat transfer coefficient at higher deluge water flow rates in Figure 5.16 to compensate for the lower mass transfer. Figure 3.3 indicates that the resistances $1/h_{dw}A_o$ and $1/h_{de}A_o$ are in series and when one resistance decreases the other must increase for the same heat transfer. With such a small bundle Mizushina et al. (1967) tested, the effect of water loss due to evaporation would be significantly less and most of the evaporation is accounted for by his mass transfer coefficient. This in turn creates a less steep gradient for his film heat transfer coefficient at high deluge water flow rates. Neither Niitsu et al. (1967), Parker & Treybal (1961) or Hasan & Sirén (2002) presented a mass transfer coefficient as a function of the deluge water and air flow rates but rather only as a function of the air flow rate so their coefficients could not be compared.

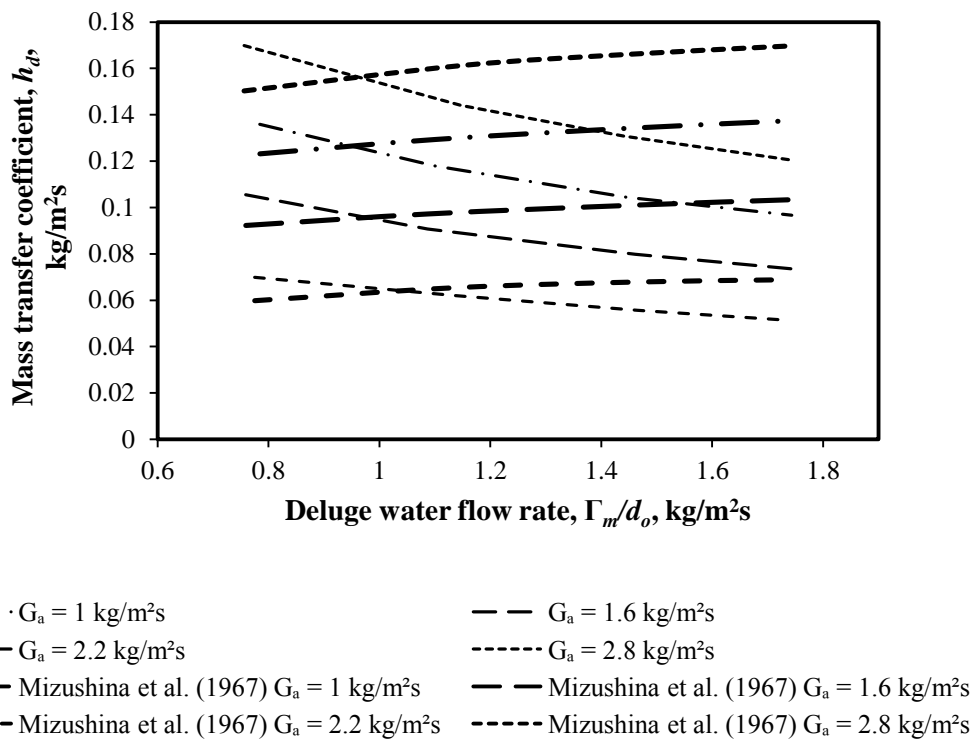


Figure 5.15: Mass transfer coefficient comparison between the current study and Mizushina et al. (1967)

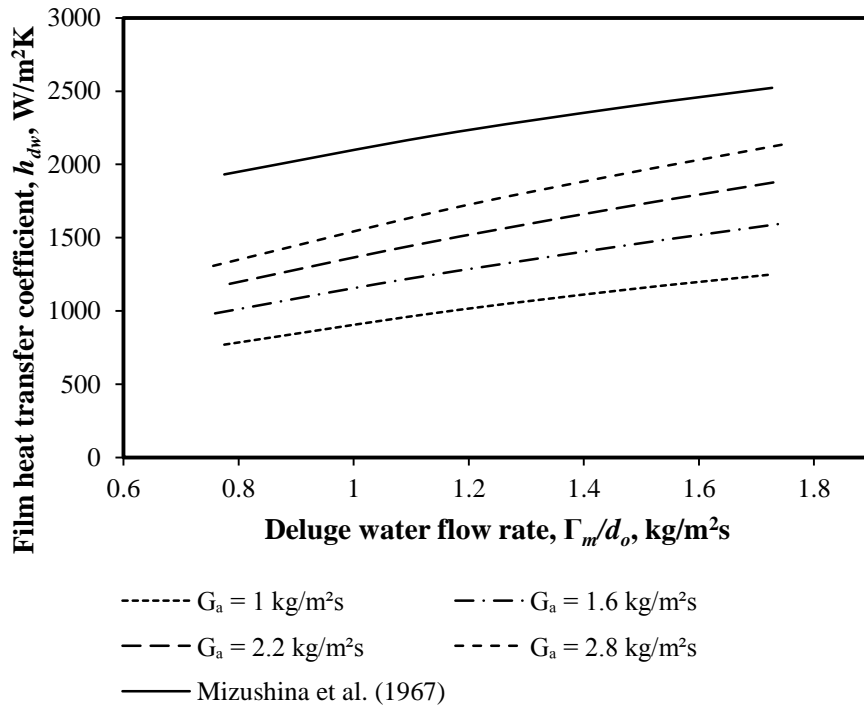


Figure 5.16: Film heat transfer coefficient comparison between the current study and Mizushina et al. (1967)

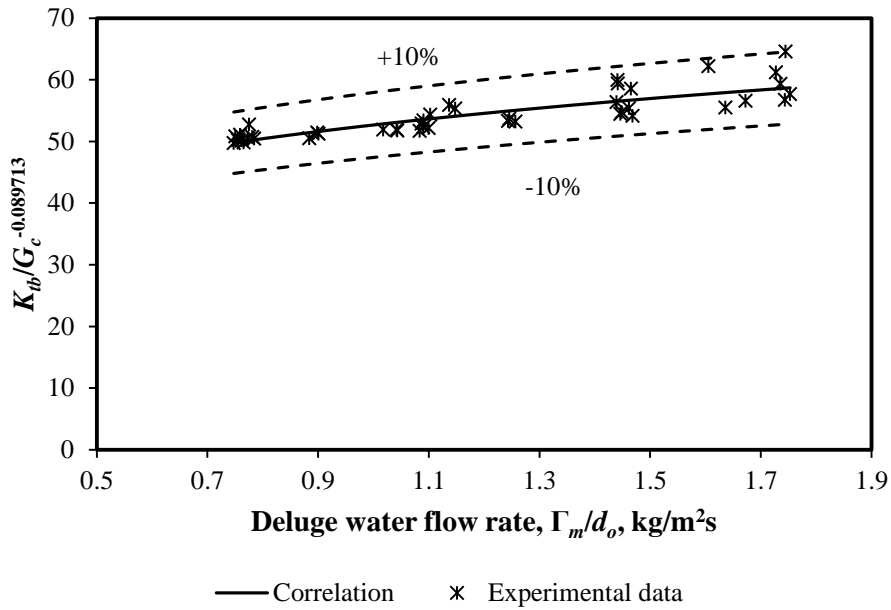


Figure 5.17: Air-side loss coefficient for the deluged tube bundle

Two-phase air-side pressure drop over tube banks are scarce in literature and Eq. (5.10) is obtained from the experimental results. It is a function of the deluge water and the air flow rate, similar to the correlation of Niitsu et al. (1967). In an

attempt to make the correlation generic, the air flow rate is defined through the critical area of the bundle. Figure 5.17 represents the correlation along with the experimental dataset.

$$K_{tb} = 52.6716 \left(\frac{\Gamma_m}{d_o} \right)^{0.19307} G_c^{-0.089713} \quad (5.10)$$

Figure 5.18 confirms the need for the correlation to predict the pressure drop over the tube bundle, since the Niitsu correlation underestimates the pressure drop by 29 to 39%. The complete data set for all the air- and deluge water flow rates is indicated in the graph. The main reason for the discrepancy is the fact that the bundle geometry of Niitsu et al. (1967) is different compared to the current bundle.

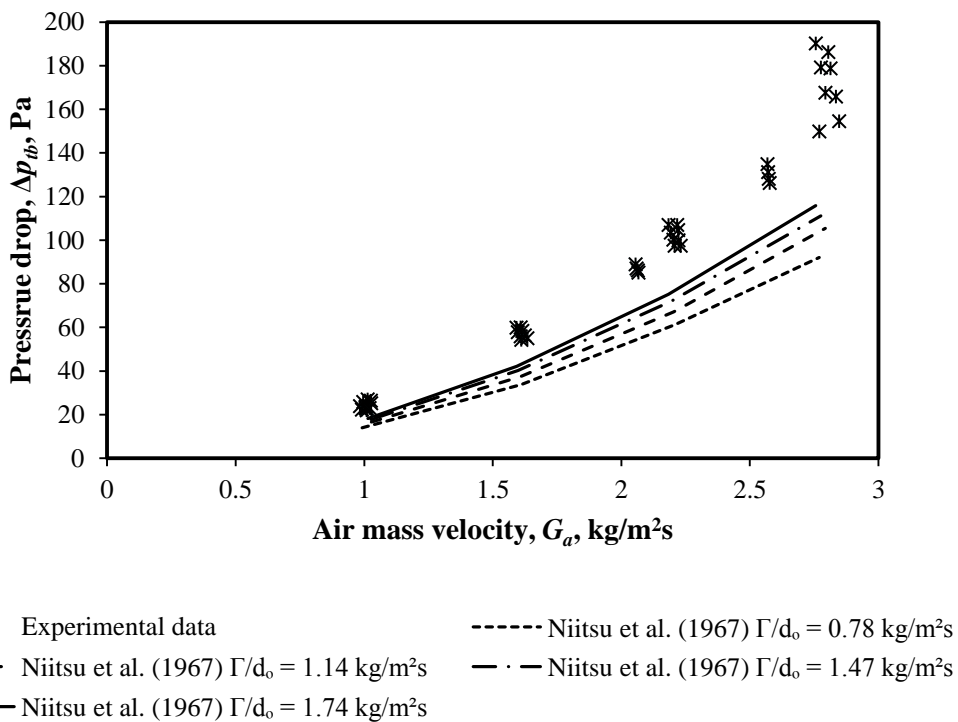


Figure 5.18: Two phase air-side pressure drop over the tube bundle

5.4 Tube bundle performance characteristics for dry operation

5.4.1 Bundle heat transfer characteristics

Dry thermal tests are conducted and Table 5.5 shows the operating ranges of all the measured parameters. One test involves five set points of air flow rates at $G_a = 1, 2, 3, 4$ and $4.6 \text{ kg/m}^2\text{s}$ with the process water flow rate kept constant. The tests are repeated three times, each time starting at a lower inlet process water temperature.

Table 5.5: Operating ranges for all the parameters during the dry thermal tests

Parameter	Symbol	Range	Units
Inlet dry-bulb temperature	T_{ai}	14.2 – 16.7	°C
Inlet wet-bulb temperature	T_{wbi}	12.2 – 13.1	°C
Outlet dry-bulb temperature	T_{ao}	30.8 – 37.9	°C
Outlet wet-bulb temperature	T_{wbo}	18.7 – 20.4	°C
Inlet process water temperature	T_{wi}	42.5 – 45.4	°C
Outlet process water temperature	T_{wo}	38.8 – 44.0	°C
Pressure drop over the nozzles	Δp_n	37.2 – 1032	Pa
Pressure drop over the tube bundle	Δp_{tb}	15.4 – 403.8	Pa
Atmospheric pressure	p_a	100560 – 101420	Pa
Process water mass flow rate	m_w	10.2 – 10.5	kg/s
Air mass flow rate	m_{avi}	2.0 – 10.5	kg/m ² s
Dry air mass flux	G_a	0.9 – 4.6	kg/m ² s
Critical dry air mass flux	G_c	1.8 – 9.3	kg/m ² s

Figure 5.19 displays the energy balances obtained from the three dry thermal tests. The energy balances were satisfactory except for the lower and higher flow rates where some energy balances were greater than 5%. The energy balances are defined as $(Q_a - Q_w)/Q_m$ with $Q_m = (Q_a + Q_w)/2$.

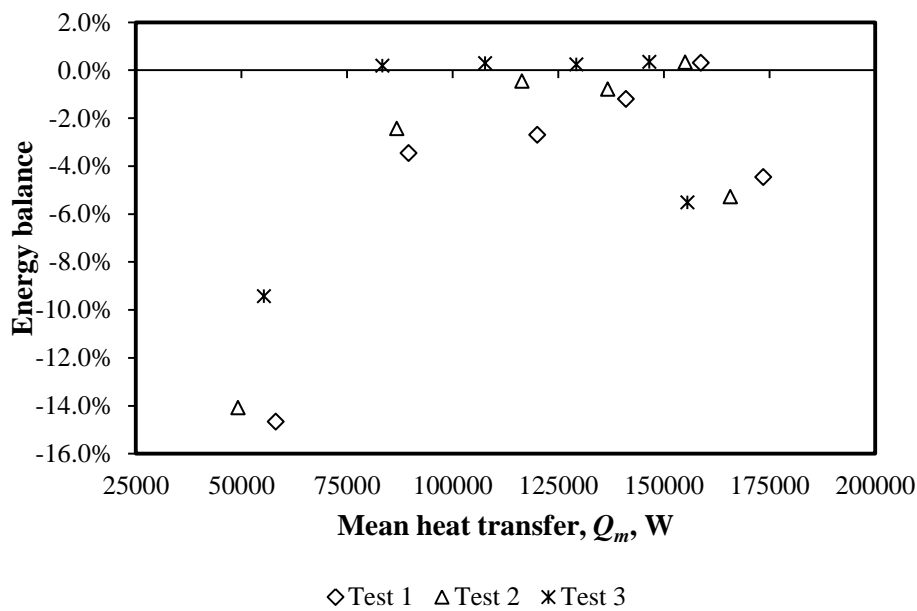


Figure 5.19: Energy balances of the dry thermal tests of the tube bundle

The experimentally determined Nusselt number values are plotted in Figure 5.20 in conjunction with correlations of Khan, et al. (2006), Zukauskas (1987) and Parker & Treybal (1961). The error bars on the graph indicate a 10% deviation on

the experimentally obtained results. The correlations of Parker & Treybal (1961) and Zukauskas (1987) obtained from actual experimental data predict the Nusselt number within 10% over this current Reynolds number range. The correlation of Khan et al. (2006) seem to overestimate the value and is within 10% for a Reynolds number of 5500 and higher. The assumptions of an isothermal boundary of the tube surface and a uniform velocity through the tube bank for their analytical model can be a possible reason for the overestimation of the Nusselt number values at lower Reynolds numbers.

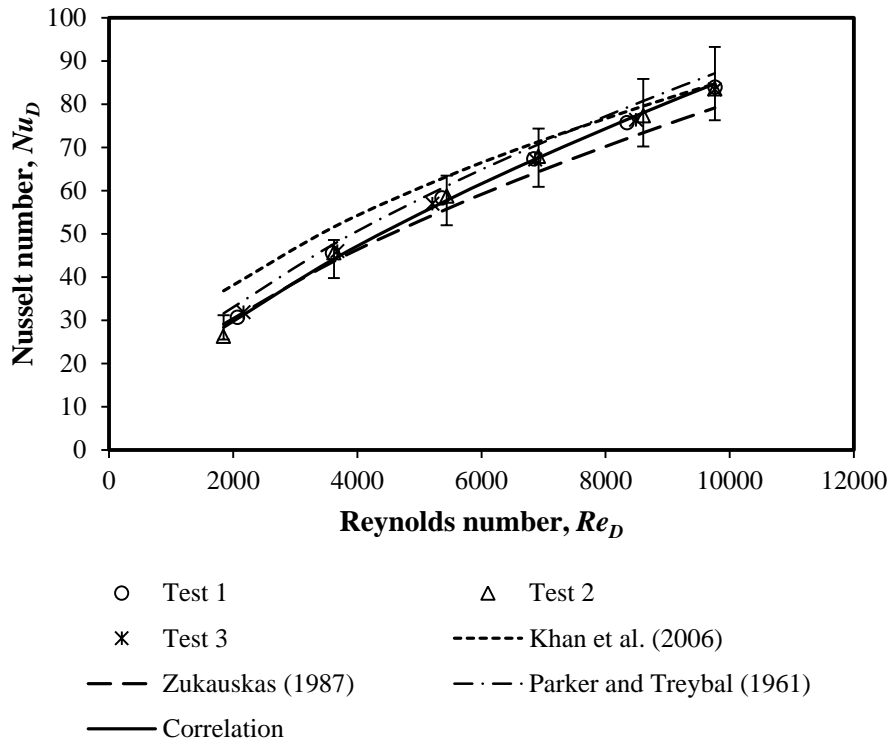


Figure 5.20: Air-side Nusselt number for dry operation

The bundle tested by Parker & Treybal (1961) is different but the correlation obtained from this author is sufficient to predict the Nu_D accurately. The correlation from the current analysis is,

$$Nu_D = 0.22731 Re_D^{0.65658} Pr_{avm}^{0.3333} \left(\frac{Pr_{avm}}{Pr_{avto}} \right)^{0.25} \quad (5.11)$$

which is valid over $1850 \leq Re_D \leq 9750$ for a bundle with 19 mm outer diameter tubes, $P_t = 2d_o$ and a triangular pitch tube layout. The correlation has a similar shape to the one proposed by Zukauskas (1987).

Figure 5.21 is the depiction of the characteristic heat transfer parameter over a range of the characteristic flow parameter. The data from all three experiments shows good repeatability. The resultant curve fit for the data is given by the following relation,

$$Ny = 54.3053Ry^{0.656597} \quad (5.12)$$

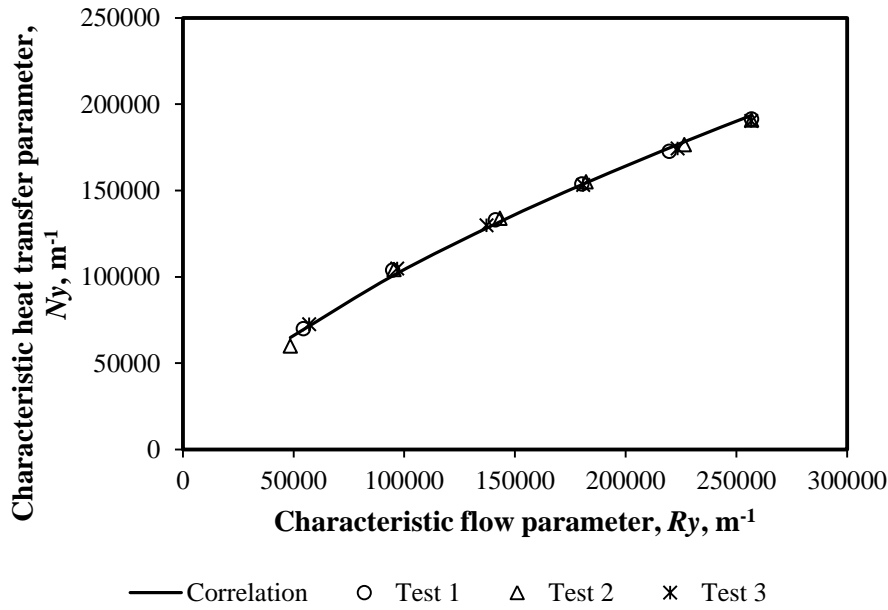


Figure 5.21: Characteristic heat transfer parameter during dry tests

5.4.2 Bundle pressure drop characteristics

Figure 5.22 illustrates the loss coefficient for the tube bundle under isothermal conditions for air flow rates over the tube bank of $1 < G_a < 4.6 \text{ kg/m}^2\text{s}$ or $2.2 < m_{avi} < 10.5 \text{ kg/s}$. Six set points are chosen within this range at $G_a = 1, 1.75, 2.5, 3.25, 4$ and $4.6 \text{ kg/m}^2\text{s}$. The loss coefficient in Figure 5.22(a) is based on the maximum velocity through the minimum flow area of the tube bundle and Figure 5.22(b) is based on the mean approach velocity.

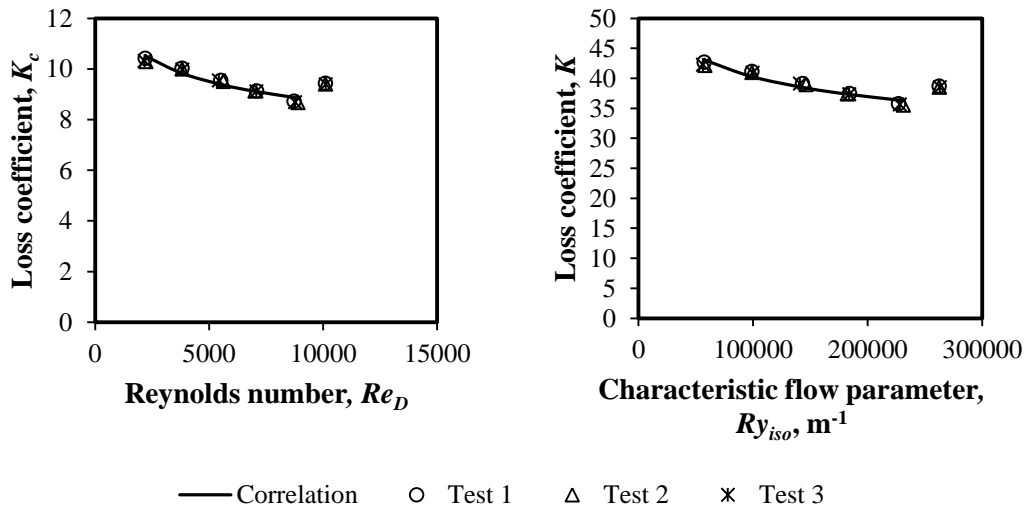
There is a gradual downward trend in the data except for the last data point at the highest flow rate in both cases where the loss coefficient tends to increase. This may be due to flow separation over the tubes with the high air velocity at the high air mass flow rates. Gaddis & Gnielinski (1985) also noted a point of inflection in their $K-Re_D$ curves for a staggered arrangement. This point of inflection is highly dependent on bundle geometry for staggered bundles but is normally observed in the transitional regime for an inline arrangement. This point is far away from the general operating point for this system and therefore not included in the correlations. Eq. (5.13) is based on the maximum velocity through the bundle and depicted in Figure 5.22(a) and Eq. (5.14) on the mean approach velocity and presented in Figure 5.22(b).

$$K_c = 27.11721Re_D^{-0.1231} \quad (5.13)$$

with $Re_D = \rho_{av}v_{max}d_o/\mu_{av}$.

$$K = 165.947Ry_{iso}^{-0.1231} \quad (5.14)$$

with $Ry_{iso} = m_{av}/\mu_{av}A_{fr}$



(a) Loss coefficient based on the maximum velocity through the minimum flow area of the bundle

(b) Loss coefficient based on the mean approach velocity

Figure 5.22: Dry tube bundle isothermal loss coefficient

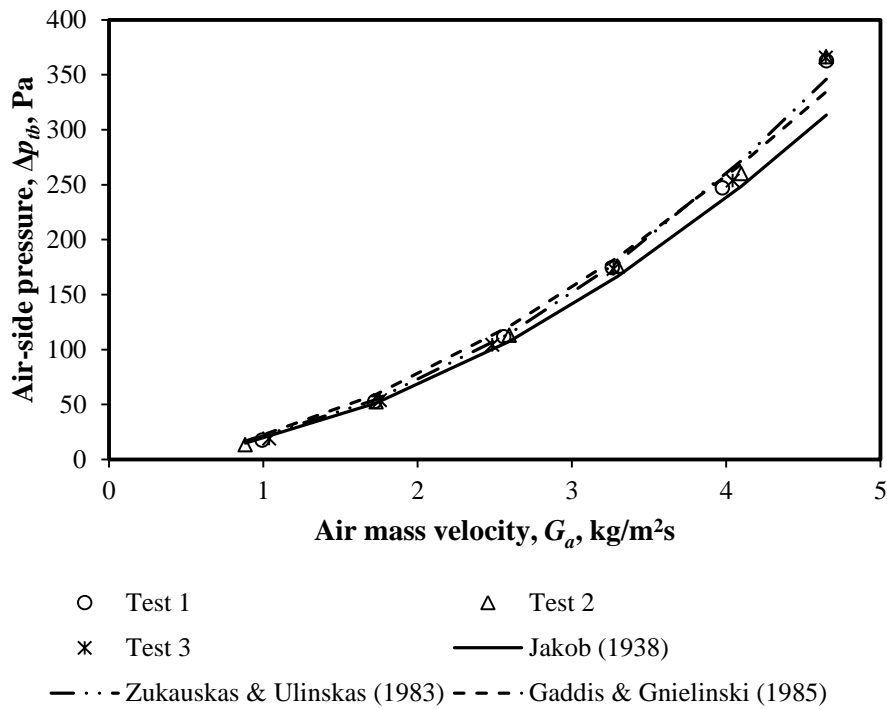


Figure 5.23: Air-side pressure drop over the tube bundle in cross flow

Jakob (1938), Zukauskas & Ulinskas (1983) and Gaddis & Gnielinski (1985) studied the pressure drop over banks of tubes in cross flow and all three correlations compare well with the data as presented in Figure 5.23. It is recommended that the correlation of Gaddis & Gnielinski (1985) is used to determine the pressure drop over the dry tube bundle, since the correlation yielded satisfactory results for the bundle geometry of Heyns (2008) as well.

The loss coefficient of the tube bundle under thermal conditions is given in Figure 5.24 and is plotted with the correlation for the loss coefficient which is applicable over $1850 \leq Re_D \leq 9750$ and for a tube bundle with a triangular pitch and $P_t = 2d_o$.

$$K = 40.6995 - 1.7737 \times 10^{-3} Re_D + 1.1025 \times 10^{-6} Re_D^2 - 2.2247 \times 10^{-10} Re_D^3 + 1.296 \times 10^{-14} Re_D^4 \quad (5.15)$$

This correlation is similar to the correlation published by Zukauskas & Ulinskas (1983). Eq. (5.15) can be used to determine the loss coefficient to calculate the pressure drop over the tube bundle with Eq. (3.58).

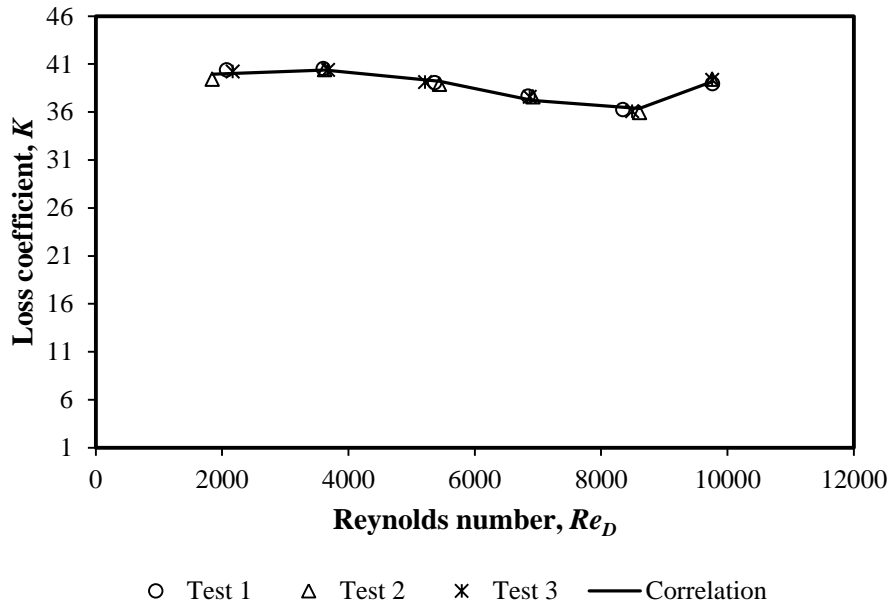


Figure 5.24: Dry tube bundle thermal loss coefficient based on the mean approach velocity

omitted from the analysis. The model indicates when backflow occurs but cannot model the heat transfer at that state. Backflow occurs when the pressure drop over two tubes of the same vapor pass diverge which indicates full condensation has occurred in the tube with the highest pressure drop. The diverging pressure drop diverges the model and makes the points of interest incalculable so no simulation result can be presented. If backflow is modeled, the heat transfer can be determined. The backflow location in this dephlegmator is primarily at the bottom of the first stage finned tube bundles. These backflow locations create stagnant zones that fill with non-condensables and have a detrimental effect on the performance of the dephlegmator. The effect would be limited considering the relatively small size of the zones. Nevertheless, the dephlegmator doesn't experience backflow for the majority of its operating conditions.

The psychrometric chart shown in Figure 6.2 confirms plume abatement which is one of the attractive features of this hybrid dephlegmator. The inlet air at (1/3/6) has more or less the same properties, with 15.6 °C and 50% relative humidity chosen as the reference ambient conditions which is the same as Heyns (2008). The saturated outlet air from the second stage tube bundle (4/5) is mixed with the hot and dry air from the first stage finned tube bundles (7), resulting in the unsaturated air as indicated by (8) and is sucked out of the dephlegmator by the fan.

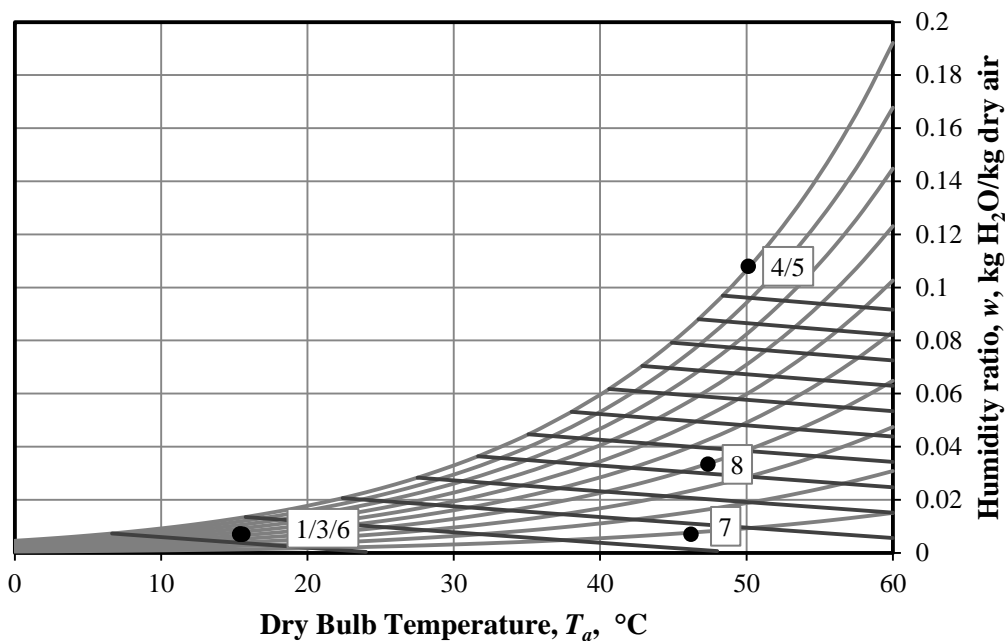


Figure 6.2: Psychrometric chart with the properties of air at the numbered locations indicated

Figure 6.3 indicates a significant increase in performance compared to the first generation hybrid dephlegmator as investigated by Heyns (2008). This performance enhancement is mainly due to the increase in heat transfer area of the second stage tube bundle by reducing the tube diameter and increasing the number

of tubes per row and the number of tube rows. The current dry performance analysis compares well with Owen (2013).

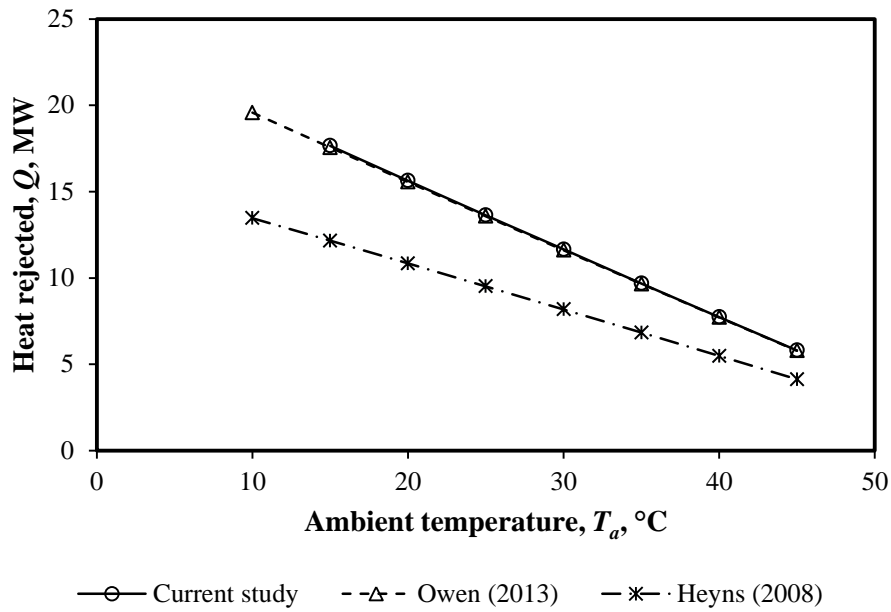


Figure 6.3: Dry operation heat rejection comparison

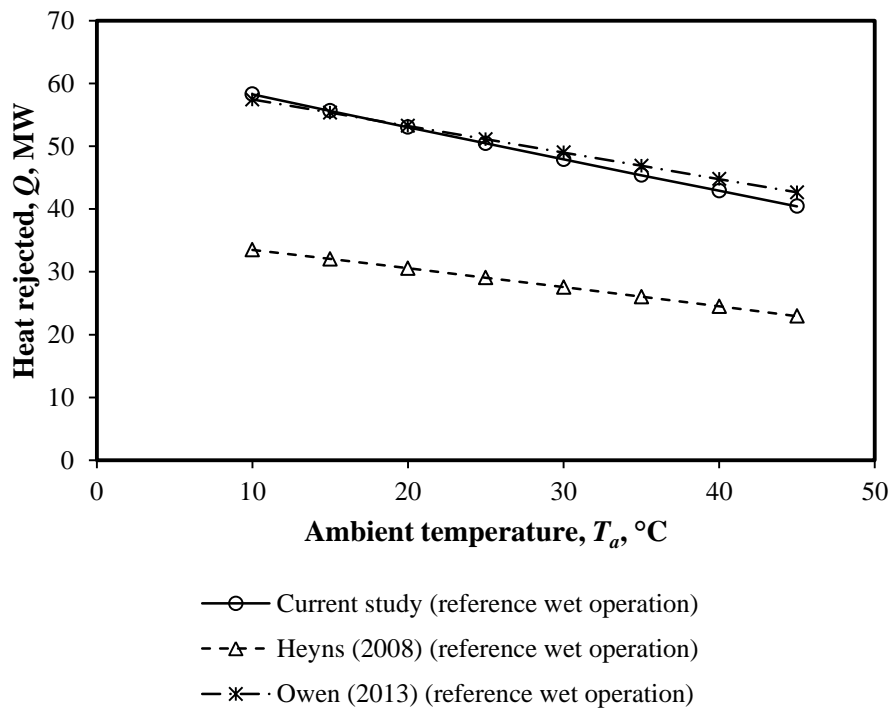


Figure 6.4: Wet operation heat rejection comparison

Figure 6.4 shows that for wet operation at the reference deluge water flow rate of 106 kg/s, the current analysis and that of Owen (2013) yields greater heat transfer

performance compared to the analysis of Heyns (2008). The improvement in performance can again be ascribed to the greater heat transfer area of the novel induced draft HDWD. In the wet operation analysis of Owen (2013), a more conservative model is used to calculate the steam-side pressure drop and thus vapor temperature and the correlation of Niitsu et al. (1967) is utilized to calculate the air-side pressure drop over the deluged tube bundle. Conversely in the current analysis, a more realistic model is followed for calculating the vapor temperature and the air-side pressure drop over the deluged tube bundle is calculated with Eq. (5.10).

In the current analysis, static pressure recovery is experienced due to condensation taking place resulting in increased vapor temperatures. The higher vapor temperatures lead to increased heat transfer performance. The heat transfer decrement of the analysis of Owen (2013) due to the conservative steam-side pressure drop calculation is cancelled with the use of the Niitsu et al. (1967) correlation, since it underestimates the pressure drop over the deluged tube bundle as shown in Figure 5.18. This in turn overestimates the air flow through the second stage tube bundles that yields greater heat transfer than the first stage finned tube bundles. These two modeling differences highlighted between the current analysis and that of Owen (2013), results in more or less the same heat transfer prediction.

Figure 6.5 and 6.6 illustrates the performance of the dephlegmator at different vapor temperatures under dry and wet operation respectively. The heat transfer performance increase with an increase in the vapor temperature as expected. At a vapor and ambient temperature of 40 °C the ITD is zero and negative at higher ambient temperatures and is therefore incalculable.

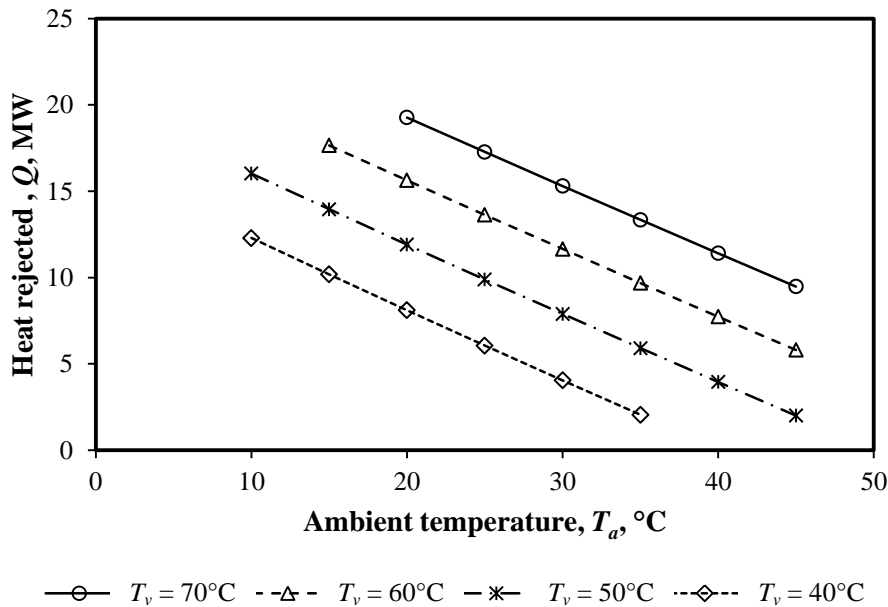


Figure 6.5: Dry operation heat rejection comparison for different vapor temperatures

In Figure 6.5 vapor backflow is noted at 10 °C for a vapor temperature of 60 °C and lower than 20 °C for a vapor temperature of 70 °C. The heat transfer capability of the finned tube bundles is sufficiently high at these temperatures to result in full condensation in the second tube row of the first stage finned tube bundles. The heat transfer of the second stage tube bundle is not sufficient to avoid the backflow occurring. These points are however unrealistic operating parameters.

During wet operation as represented in Figure 6.6 the heat transfer capability of the second stage tube bundle is not sufficient at lower vapor temperatures to condense enough steam to avoid backflow in the first stage tube bundles. This results in vapor backflow at conditions lower than 20 °C for a vapor temperature of 40 °C, and lower than 15 °C for a vapor temperature of 50 °C.

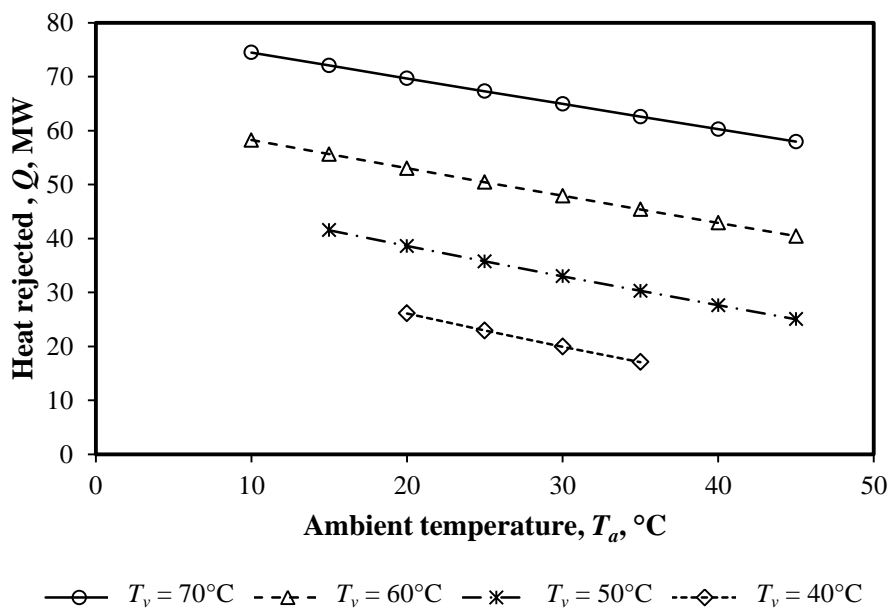


Figure 6.6: Wet operation heat rejection performance for different vapor temperatures

Figure 6.7 depicts the effect of the deluge water flow rate on the heat transfer performance. Three deluge water flow rates are investigated namely 106, 120 and 145 kg/s or $G_{dw} = 1.85, 2.09$ and $2.53 \text{ kg/m}^2\text{s}$. A deluge water flow rate of 120 kg/s yields a 0.8% increase in performance while a flow rate of 145 kg/s yields a 2% increase compared to the reference flow rate of 106 kg/s. In the current analysis at an inlet vapor temperature of 60 °C, the average deluge water temperature is ~50 °C which is the reported limit at which scaling is no longer soft and easily washable according to Finlay & Harris (1984).

A performance comparison between the dry and the reference wet operation of the dephlegmator with $T_v = 60^\circ\text{C}$ is illustrated in Figure 6.8. The heat transfer at 10 °C with the dry operation is not shown because it is incalculable due to backflow.

A performance enhancement of between 215 and 597% is noted for ambient temperatures between 15 and 45 °C.

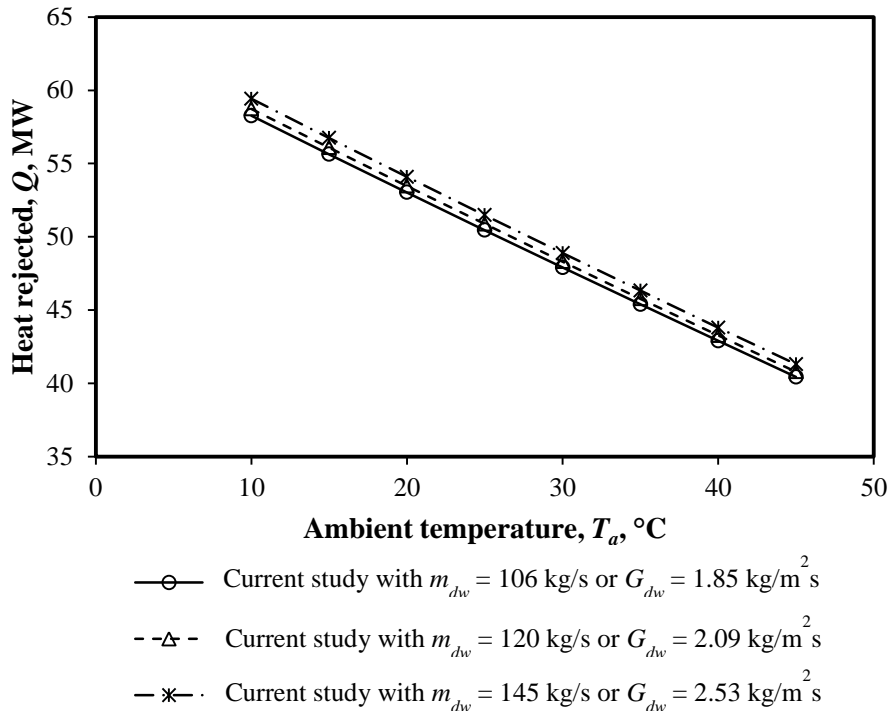


Figure 6.7: The effect of deluge water flow rate variation on the performance of the dephlegmator

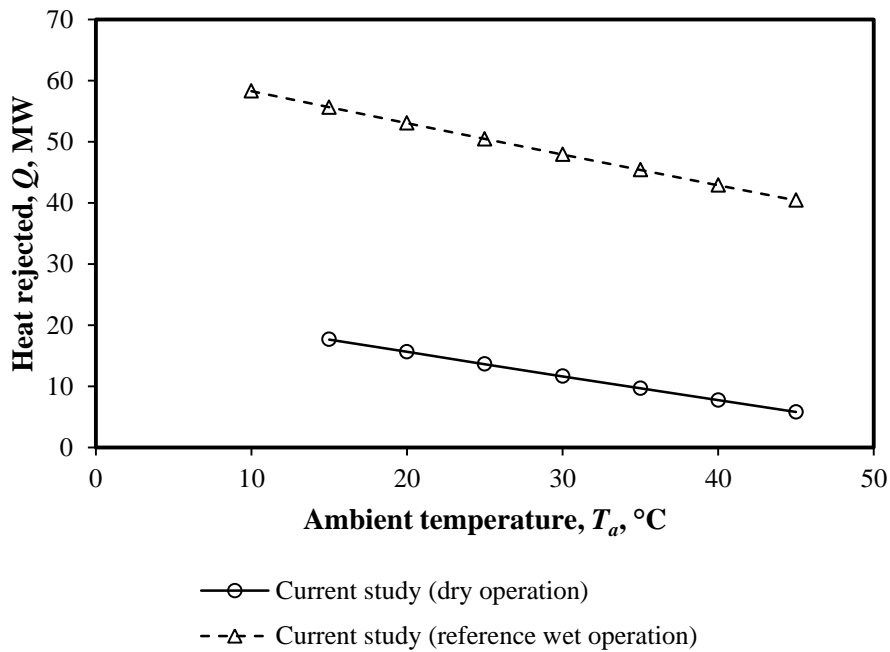


Figure 6.8: Comparison of the dry versus wet operation performance at the reference deluge water flow rate

Figure 6.9 exemplifies the fan power consumption (only $\Delta p_f V$) during dry and wet operation of the HDWD. The fan speed is kept constant for dry and wet operation. No draft equation was solved for the analysis of Heyns (2008) and consequently not plotted here. The dry operation fan power consumption of the current study agrees well with the results of Owen (2013) because the calculated vapor temperature is close to 60 °C and Owen (2013) assumed the temperature constant throughout the dephlegmator. For the dry operation the air volumetric flow rate is higher and the static pressure over the fan lower, but the fan power is still greater compared to the wet operation case. The required static pressure of the fan is higher for the wet operation due to greater air-side pressure drop over the wet bundle compared to dry operation. This lowers the volumetric flow rate throughout the whole dephlegmator and consequently lowers the total required fan power consumption. The discrepancy in the fan power for the wet operation between the current analysis and Owen (2013) can mainly be ascribed to the fact that the correlation of Niitsu et al. (1967) is used in the analysis of Owen (2013) and due to the calculated vapor temperature difference. Niitsu et al. (1967) underestimates the actual pressure drop over the deluged tube bundles.

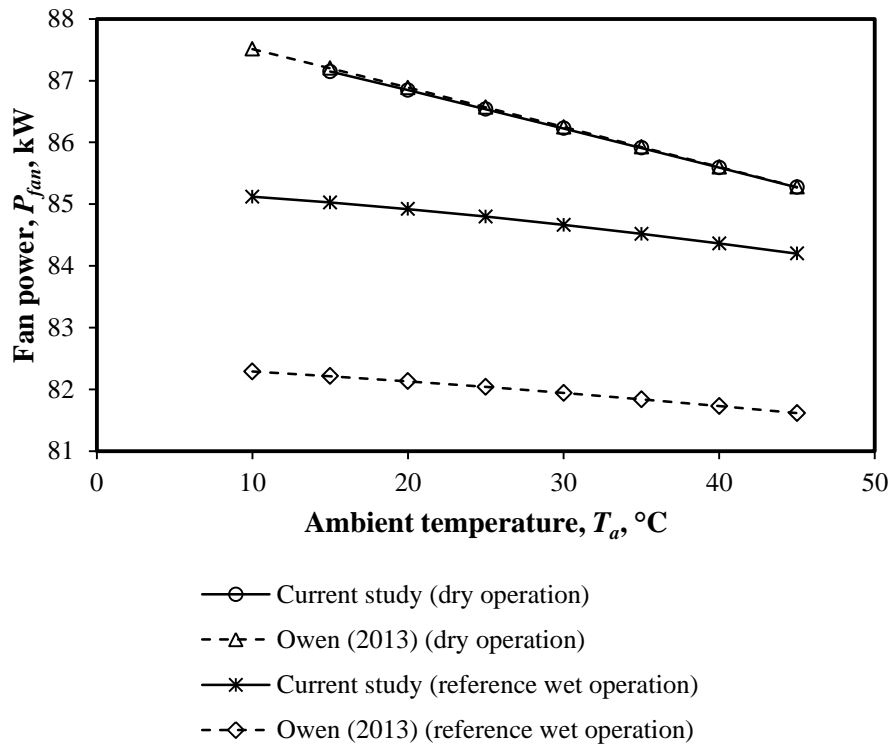


Figure 6.9: Fan power consumption for dry and wet operation

The fan power consumption at different vapor temperatures is depicted for dry and wet operation in Figure 6.10 and 6.11 respectively. The deluge water flow rate is kept constant at the reference flow rate of 106 kg/s. In both cases the fan power consumption reduces with an increase in vapor and ambient temperatures. A change in these temperatures determines the air flow distribution through the

first and second stage of the HDWD and consequently the fan operating point as detailed earlier. The peculiar slope for $T_v = 60^\circ\text{C}$ for dry operation can be attributed to interdependencies of the vapor temperature and the air flow distribution at this specific vapor temperature. The slope does however agree well with the results of Owen (2013) as shown in Figure 6.9.

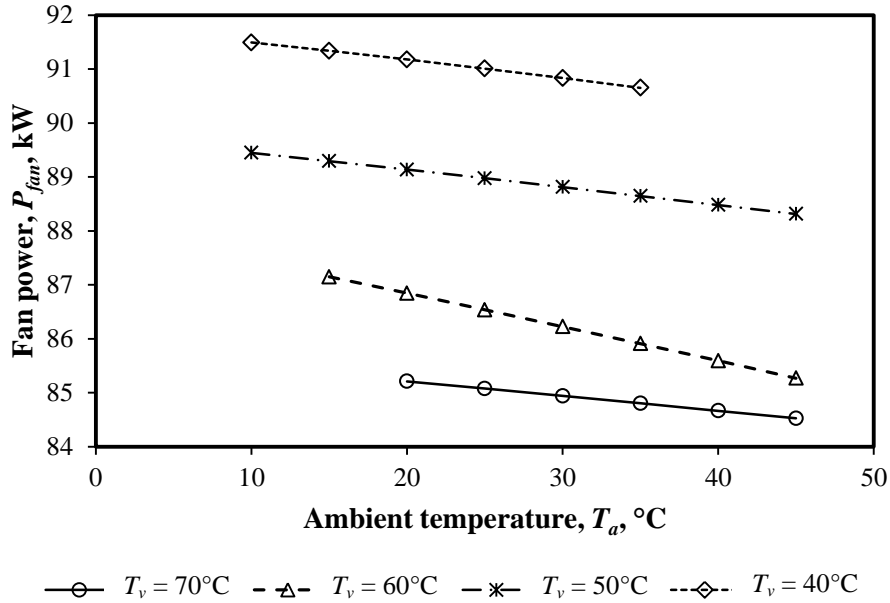


Figure 6.10: Dry operation fan power consumption comparison for different vapor temperatures

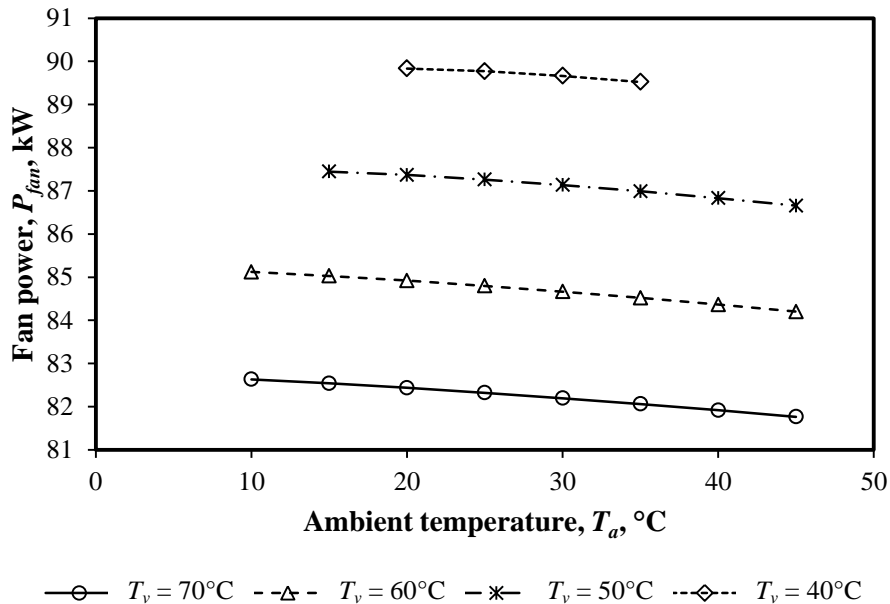


Figure 6.11: Wet operation fan power consumption comparison for different vapor temperatures

Figure 6.12 illustrates how the deluge water evaporation rate increases with increasing deluge water flow rate and decreases with increasing ambient temperature. With greater deluge water flow rates, greater heat transfer can be expected with accompanying evaporation losses. The evaporation losses decrease with increasing ambient temperature due to less air flowing through the tube bank compared to the finned tube bundles. With the assumption of saturated outlet conditions above the second stage tube bundle [(4) in Figure 6.1], the amount of water evaporated can only decrease with a decrease in air flow rate. Figure 6.13 depicts how the evaporation rate increases with an increase in vapor temperature. The deluge water flow rate is again fixed at the reference flow rate. The higher vapor temperature results in higher surface temperatures in the HDWD that will lead to higher evaporation losses.

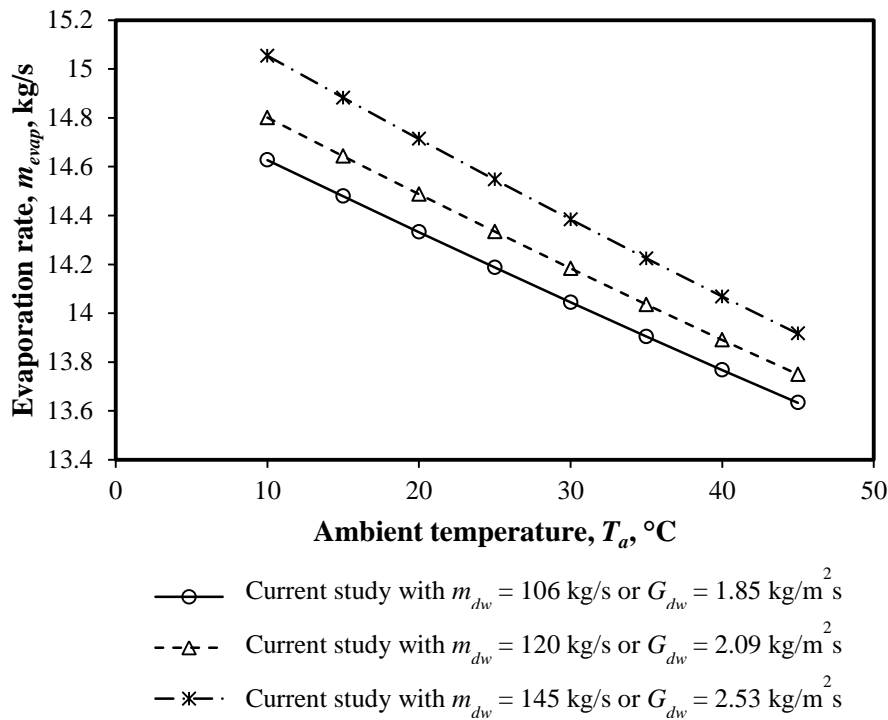


Figure 6.12: The predicted evaporation rate at different deluge water flow rates

A comparison of the evaporation losses at the reference deluge water flow rate between the three models is shown in Figure 6.14. More water evaporates in the current configuration compared to the configuration of Heyns (2008), due to the greater heat transfer area the deluge water is exposed to. The discrepancy in the obtained evaporation rates for the current model and that of Owen (2013) can again be attributed to the use of the correlation of Niitsu et al. (1967) and the calculated vapor temperatures. As stated earlier, the pressure drop is underestimated in the model of Owen (2013) and subsequently the air flow through the second stage tube bundles is overestimated. An increased air flow rate will result in higher evaporation rates with the assumption of saturated outlet conditions. The evaporation rate slopes of the current analysis and that of Owen

(2013) is dictated by the calculated vapor temperatures that has an influence on the density of the air flowing through the tube bundle section and determines the air flow distribution through the first and second stage of cooling of the HDWD.

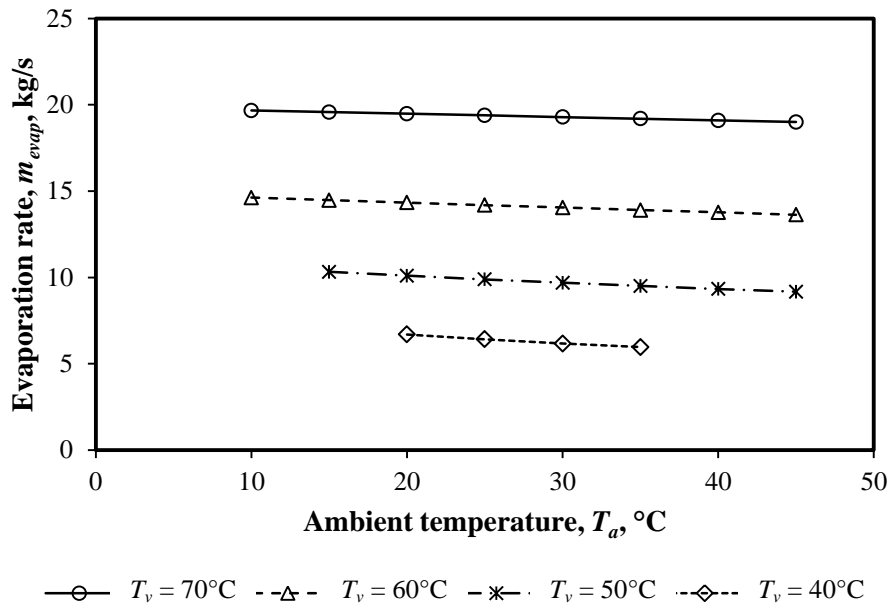


Figure 6.13: The predicted evaporation rate at different vapor temperatures

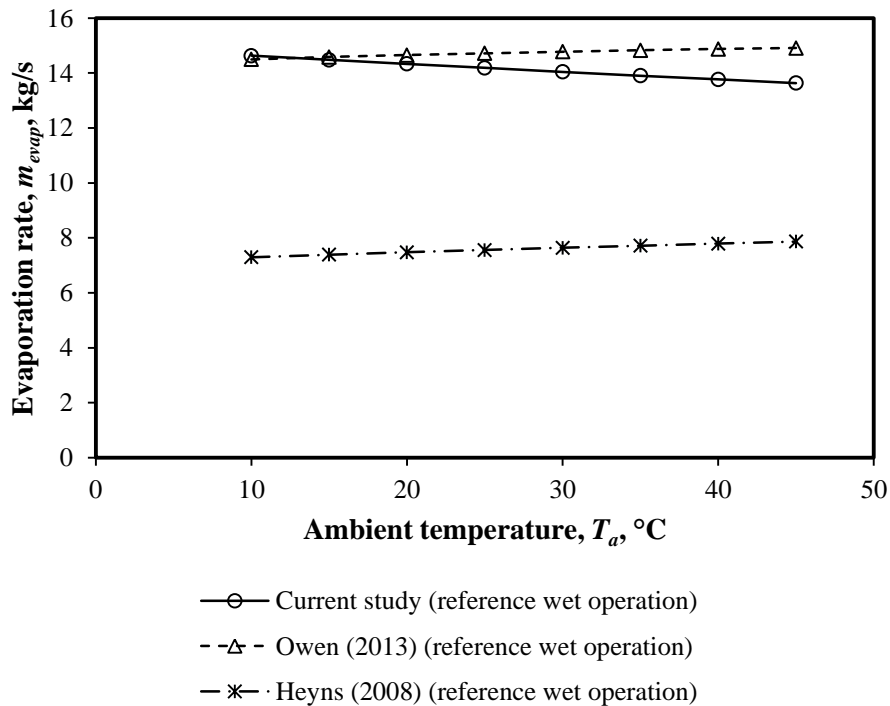


Figure 6.14: A comparison of the predicted evaporation rates of the three models used

7 Conclusion

This thesis presents a hybrid induced draft dephlegmator which is a continuation of work done by Heyns (2008) and Owen (2013). It is proposed to augment the performance of air-cooled condenser systems. Other current hybrid systems have been considered and compared with the dephlegmator to prove the viability of the technology. The dephlegmator consists of two stages of cooling with steam flow in series and the air flow in parallel through both stages. The first stage comprises finned tube bundles, similar to existing air-cooled condenser bundles, while the second stage consists of bare tube bundles. The outer surface of the second stage bundle can be operated dry or wet. The heat and mass transfer characteristics and air-side pressure drop of the bare tube bundle with its unique geometry is unknown and is required for the detail design of the dephlegmator.

A bundle representative of this second stage tube bundle of the dephlegmator has successfully been designed, manufactured and installed into the test facility after some necessary modifications. Dry and wet performance tests of the tube bundle at different air and deluge water flow rates yielded the performance characteristics after thorough analysis of the experimental data. The characteristics compare well with other correlations from literature that confirm the cogency of these correlations. The optimum tube pitch and layout has been confirmed by comparing the experimental results to literature such as the work of Owen (2013).

The current dephlegmator model verifies the initial model of Owen (2013) and improves it by incorporating the pressure drop over the tube bundle obtained from the experiments and by employing a more realistic steam-side pressure drop calculation to simulate its performance. It shows measurable performance increase to the pioneering study of Heyns (2008) under dry and wet operation due to the novel second stage bundle geometry but at the expense of increased water consumption. The dephlegmator has 215 to 597% higher performance under wet operation compared to dry with no visible plume. Wet operation has a lower air flow rate and a higher static pressure rise over the fan compared to dry operation with a slightly lower static pressure rise and greater flow rate supplied by the fan. Consequently the fan power is lower for the wet operation compared to dry. Varying the deluge water flow rate from 1.85 to 2.53 kg/m²s yields a 2% increase in performance for wet operation.

This proves the proper operation and significant performance enhancement capability of this novel hybrid induced draft dephlegmator to be fitted to an air-cooled condenser system to increase the overall power plant output and efficiency by minimizing water consumption with no visible plume.

8 References

- Bertrand, T.P., 2011, *Evaluation of a 1.5 x 1.5 m² counter-flow fill performance test facility with a view to contributing to a fill performance standard*. Stellenbosch University.
- Bourillot, C., 1983, *Numerical model for calculating the performance of an evaporative cooling tower*, California.
- Chato, J.C., 1962, *Laminar condensation inside horizontal and inclined tubes*, Journal of ASHRAE. pp. 52–60.
- Erens, P.J. & Dreyer, A.A., 1993, *Modelling of indirect evaporative air coolers*, International Journal of Heat and Mass Transfer. pp. 17–26.
- Ettouney, H.M., El-Dessouky, H.T., Bouhamra, W. & Al-Azmi, B., 2001, *Performance of Evaporative Condensers*, Heat Transfer Engineering. pp. 41–55.
- Finlay, I.C. & Harris, D., 1984, *Evaporative cooling of tube banks*, International Journal of Refrigeration. pp. 214–224.
- Fried, E. & Idelchik, I.E., 1989, *Flow Resistance: A Design Guide for Engineers First*. J. A. Orvedahl, ed., New York: Hemisphere Publishing Corporation.
- Gaddis, E.S. & Gnielinski, V., 1985, *Pressure drop in cross flow across tube bundles*, International Chemical Engineering. pp. 1–15.
- Groenewald, W. & Kröger, D.G., 1995, *Effect of mass transfer on turbulent friction during condensation inside ducts*, International Journal of Heat and Mass Transfer. pp. 3385–3392.
- Hasan, A. & Sirén, K., 2003, *Performance investigation of plain and finned tube evaporatively cooled heat exchangers*, Applied Thermal Engineering. pp. 325–340.
- Hasan, A. & Sirén, K., 2002, *Theoretical and computational analysis of closed wet cooling towers and its applications in cooling of buildings*, Energy and Buildings. pp. 477–486.
- Heyns, J.A., 2008, *Performance characteristics of an air-cooled steam condenser incorporating a hybrid (dry/wet) dephlegmator*. Stellenbosch University.
- Heyns, J.A. & Kröger, D.G., 2010, *Experimental investigation into the thermal-flow performance characteristics of an evaporative cooler*, Applied Thermal Engineering. Elsevier Ltd, pp. 492–498.

- Khan, W.A., Culham, J.R. & Yovanovich, M.M., 2006, *Convection heat transfer from tube banks in crossflow: Analytical approach*, International Journal of Heat and Mass Transfer. pp. 4831–4838.
- Kröger, D.G., 2004, *Air-cooled Heat exchangers and Cooling Towers: Thermal-Flow Performance Evaluation and Design*, Tulsa, Oklahoma, USA: PennWell Corporation.
- Lips, S. & Meyer, J.P., 2011, *Two-phase flow in inclined tubes with specific reference to condensation: A review*, International Journal of Multiphase Flow. pp. 845–859.
- Maulbetsch, J. & DiFilippo, M., 2012, *Advanced Hybrid Cooling Systems: Technology Review*, Palo Alto, California.
- Merkel, F., 1925, *Verdunstungskühling*, VDI-Zeitschrift. pp. 123–128.
- Mizushina, T., Ito, R. & Miyashita, H., 1968, *Characteristics and methods of thermal design of evaporative coolers*, International Chemical Engineering. pp. 532–538.
- Mizushina, T., Ito, R. & Miyashita, H., 1967, *Experimental study of an evaporative cooler*, International Chemical Engineering. pp. 727–732.
- Niitsu, Y., Naito, K. & Anzai, T., 1967, *Studies on Characteristics and Design Procedure of Evaporative Coolers*, Journal of SHASE.
- Owen, M., 2013, *Air-cooled condenser steam flow distribution and related dephlegmator design considerations*. Stellenbosch University.
- Owen, M.T.F. & Kröger, D.G., 2013, *A Hybrid Dephlegmator for Incorporating into an Air-cooled steam condenser*, International Conference on Applied Energy.
- Panjeshahi, M.H., Ataei, A., Gharaie, M. & Parand, R., 2009, *Optimum design of cooling water systems for energy and water conservation*, Chemical Engineering Research and Design. pp. 200–209.
- Papaefthimiou, V.D., Rogdakis, E.D., Koronaki, I.P. & Zannis, T.C., 2012, *Thermodynamic study of the effects of ambient air conditions on the thermal performance characteristics of a closed wet cooling tower*, Applied Thermal Engineering. Elsevier Ltd, pp. 199–207.
- Parker, R.P. & Treybal, R.E., 1961, *The heat, mass transfer characteristics of evaporative coolers*, AIChE Chemical Engineering Progress Symposium Series. pp. 138–149.
- Poppe, M. & Rögener, H., 1984, *Evaporative cooling systems*, VDI-Warmteatlas, Section Mh.

- Sarker, M.M.A., Kim, E., Moon, C.G. & Yoon, J.I., 2008, *Performance characteristics of the hybrid closed circuit cooling tower*, Energy and Buildings. pp. 1529–1535.
- Sarker, M.M.A., Shim, G.J., Lee, H.S., Moon, C.G. & Yoon, J.I., 2009, *Enhancement of cooling capacity in a hybrid closed circuit cooling tower*, Applied Thermal Engineering. Elsevier Ltd, pp. 3328–3333.
- Söylemez, M.S., 2001, *On the optimum sizing of cooling towers*, Energy Conversion and Management. pp. 783–789.
- Stabat, P. & Marchio, D., 2004, *Simplified model for indirect-contact evaporative cooling-tower behaviour*, Applied Energy. pp. 433–451.
- Tezuka, S., Kasai, S. & Nakamura, T., 1977, *Performance of an Evaporative Cooler*, Heat Transfer Japanese Research. pp. 1–18.
- Wilber, K.R. & Zammit, K., 2005, *Development of Procurement Guidelines for Air-Cooled Condensers*, California.
- Zalewski, W. & Gryglaszewski, P.A., 1997, *Mathematical model of heat and mass transfer processes in evaporative fluid coolers*, Chemical Engineering and Processing: Process Intensification. pp. 271–280.
- Zheng, W.-Y., Zhu, D.-S., Zhou, G.-Y., Wu, J.-F. & Shi, Y.-Y., 2012, *Thermal performance analysis of closed wet cooling towers under both unsaturated and supersaturated conditions*, International Journal of Heat and Mass Transfer. Elsevier Ltd, pp. 7803–7811.
- Zukauskas, A., 1987, *Heat Transfer from Tubes in Cross Flow* S. Kakac, R. K. Shah, & W. Aung, eds. *Handbook of Single Phase Convective Heat Transfer*, pp.6.1 – 6.45.
- Zukauskas, A. & Ulinskas, R., 1983, *Banks of plain and finned tubes. Heat Exchanger Design Handbook*, pp.1–17.

Appendix A: Correlations for heat and mass transfer and air-side pressure drop

A.1 Dry operation of the tube bundle

A.1.1 Heat transfer correlations

The dimensional correlation for the air-side convective heat transfer coefficient as proposed by Parker & Treybal (1961)

$$h_a = 30.3152G_c^{0.607} \quad (\text{A.1})$$

which is valid over critical mass flux range of $0.7 < G_c < 9.6 \text{ kg/m}^2\text{s}$.

The correlation of Zukauskas (1987) for the Nusselt number of a staggered tube bundle for $1000 < Re_D < 2 \times 10^5$,

$$Nu_D = 0.35 \left(\frac{P_t}{P_l} \right)^{0.2} Re_D^{0.6} Pr_{avm}^{0.36} \left(\frac{Pr_{avm}}{Pr_{avto}} \right)^{0.25} \quad (\text{A.2})$$

Khan et al. (2006) proposed a correlation for the Nusselt number after a thorough analytical analysis on the flow pattern of the air over the tubes,

$$Nu_D = \frac{0.61 \left(\frac{P_t}{d_o} \right)^{0.091} \left(\frac{P_l}{d_o} \right)^{0.053}}{1 - 2 \exp\left(-\frac{1.09P_l}{d_o}\right)} Re_D^{0.5} Pr_{avm}^{\frac{1}{3}} \quad (\text{A.3})$$

A.1.2 Pressure drop correlations

All the pressure drop correlations take on the following form,

$$\Delta p_{tb} = K_c n_r \frac{\rho_{av} v_{max}^2}{2} \quad (\text{A.4})$$

with each author publishing a different value for K_c with $a = P_t/d_o$ and $b = P_l/d_o$.

Jakob (1938) as quoted in Gaddis & Gnielinski (1985). No applicable range was given.

$$K_c = \frac{1}{Re_D^{0.16}} \left[1 + \frac{0.47}{(a-1)^{1.06}} \right] \quad (\text{A.5})$$

Zukauskas & Ulinskas (1983) proposed the following relation for the pressure loss coefficient over a bank of tubes with $a = 2$ and a triangular pitch pattern with $1000 < Re_D < 10000$, $n_r > 6$,

$$\frac{K_c}{k_1} = \left(0.343 + \frac{0.303 \times 10^3}{Re_D} - \frac{0.717 \times 10^5}{Re_D^2} + \frac{0.88 \times 10^7}{Re_D^3} - \frac{0.38 \times 10^9}{Re_D^4} \right) \quad (\text{A.6})$$

k_1 was found to be close to 1 and no appreciable effect of cooling or heating was found on K_c for $Re_D > 1000$. The correlation of Gaddis & Gnielinski (1985) for a staggered bundle with the pressure loss coefficient K_c defined as,

$$K = \xi_{i,l} f_{zn,l} + \xi_{i,t} f_{z,t} \left[1 - \exp\left(-\frac{Re_D + 200}{1000}\right) \right] \quad (\text{A.7})$$

with the laminar contributing term given by,

$$\xi_{i,l} f_{zn,l} = \frac{280\pi[(b^{0.5} - 0.6)^2 + 0.75]}{(4ab - \pi)a^{1.6}Re_D} \left(\frac{\mu_{avto}}{\mu_{avm}}\right)^{\frac{0.57}{\left(\frac{4ab}{\pi} - 1\right)Re_D}^{0.25}} \quad (\text{A.8})$$

together with the turbulent contributing term,

$$\xi_{i,t} f_{z,t} = \frac{1}{Re_D^{0.25}} \left[2.5 + \frac{1.2}{(a - 0.85)^{1.08}} + 0.4 \left(\frac{b}{a} - 1\right)^3 - 0.01 \left(\frac{a}{b} - 1\right)^3 \right] \left(\frac{\mu_{avto}}{\mu_{avm}}\right)^{0.14} \quad (\text{A.9})$$

The equation of Gaddis & Gnielinski (1985) is applicable over $1 \leq Re_D \leq 3 \times 10^5$, $n_r \geq 10$, $1.25 \leq a \leq 3$ and $0.6 \leq b \leq 3$.

A.2 Wet operation of the tube bundle

A.2.1 Film heat and mass transfer coefficients

The heat and mass transfer correlations of four authors are quoted, starting with the correlation for mass transfer of Parker & Treybal (1961),

$$h_d = 0.04935 \left(\frac{m_{avm}}{A_c}\right)^{0.905} \quad (\text{A.10})$$

with the applicable range $0.68 < m_{avm}/A_c < 5$, $\text{kg/m}^2\text{s}$ and the film heat transfer coefficient,

$$h_w = 704(1.3936 + 0.02214T_{dwm}) \left(\frac{\Gamma_m}{d_o}\right)^{0.333} \quad (\text{A.11})$$

The deluge water temperature is in °C and an applicable range of $1.4 < \Gamma_m/d_o < 3$, $\text{kg/m}^2\text{s}$.

The correlation for mass transfer of Niitsu et al. (1967),

$$h_d = 0.076 \left(\frac{m_{avm}}{A_c} \right)^{0.8} \quad (\text{A.12})$$

with an applicable range of $1.5 \leq \left(\frac{m_{avm}}{A_c} \right) \leq 5$, kg/m²s and the film heat transfer coefficient,

$$h_w = 990 \left(\frac{\Gamma_m}{d_o} \right)^{0.46} \quad (\text{A.13})$$

for $P_t/d_o = 2.34$, $P_l/d_o = 2.38$ and $0.5 \leq \Gamma_m/d_o \leq 3.2$, kg/m²s.

The correlation for mass transfer of Mizushina et al. (1967)

$$h_d = 5.5439 \times 10^{-8} Re_{avm}^{0.9} Re_{dwm}^{0.15} d_o^{-1.6} \quad (\text{A.14})$$

for $1.2 \times 10^3 < Re_{avm} < 1.4 \times 10^4$ and $50 < Re_{dwm} < 240$ with $Re_{avm} = m_{avm} d_o / (A_c \mu_{avm})$ and $Re_{dwm} = 4 \Gamma_m / \mu_{dwm}$ with $\Gamma_m = m_{dw} d_o / (2n_{tr} P_t L_{tb})$.

The film heat transfer coefficient,

$$h_w = 2102.9 \left(\frac{\Gamma_m}{d_o} \right)^{0.333} \quad (\text{A.15})$$

applicable for the range $0.2 < \Gamma_m/d_o < 5.5$ kg/m²s.

Hasan & Sirén (2002) supplies this mass transfer coefficient in conjunction with the use of Eq. (A.11) which is valid for $0.96 < G_a < 2.76$ kg/m²s.

$$h_d = 0.065 G_a^{0.773} \quad (\text{A.16})$$

A.2.2 Pressure drop correlations

The pressure drop over the tube bundle of Niitsu et al. (1967)

$$\Delta p_a = 4.9 n_r P_l \left(\frac{m_{av}}{n_b A_c} \right)^{1.85} \left(\frac{\Gamma_m}{d_o} \right)^{0.285} \quad (\text{A.17})$$

valid for $2 \leq m_{av}/A_c \leq 6$ and $1.3 \leq \Gamma_m/d_o \leq 3.5$ kg/s as reported in Heyns (2008).

Appendix B: Induced draft HDWD model

The method of analysis of this section is similar to the methods used by Kröger (2004) as quoted by Heyns (2008) and Owen (2013) and the following assumptions are applicable:

- Correlations for all the thermo-physical properties of the fluids (air, vapor and water/condensate) are defined in Kröger (2004)
- Saturated steam enters the dephlegmator
- All the steam that enters condenses and leaves the system as water
- The condensation heat transfer coefficient for the second stage tube bundle is calculated from the vapor properties of the first pass and assumed constant throughout the bundle, since the vapor temperature does not vary drastically
- The convergence interval throughout the analysis is 1×10^{-7}

B.1 Evaluation of the thermal performance of the HDWD with wet operation of the second stage bundles

B.1.1 The first stage (finned tube) section

Figure 6.1 is again quoted here for easy reference when referring to the sample calculation.

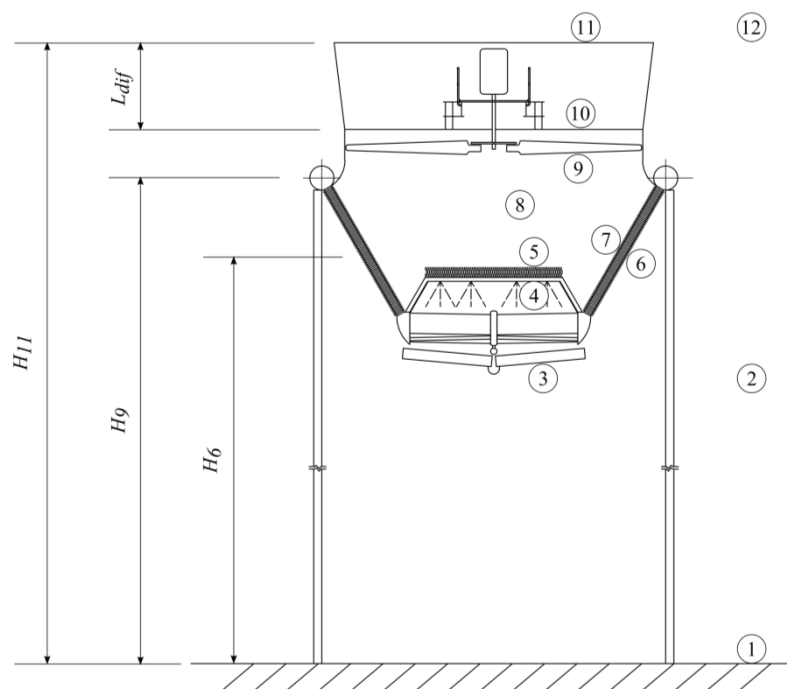


Figure B.1: Schematic of the dephlegmator with numbered locations for the sample calculation

The ambient conditions

Atmospheric pressure	$p_{a1} = 84600 \text{ Pa}$
Ambient dry-bulb temperature	$T_{a1} = 15.6 \text{ }^\circ\text{C}$
Ambient wet-bulb temperature	$T_{wb1} = 10 \text{ }^\circ\text{C}$

Physical properties of the system

Inside height of the tube	$H_t = 0.097 \text{ m}$
Inside width of the tube	$W_t = 0.017 \text{ m}$
Length of finned tube	$L_t = 4.5 \text{ m}$
Number of tube rows	$n_r = 2$
Number of tubes per bundle (first row)	$n_{tb1} = 57$
Number of tubes per bundle (second row)	$n_{tb2} = 58$
Number of steam passes	$n_{vp} = 1$
Number of bundles	$n_b = 8$
Apex angle of the A-frame	$\theta = 30^\circ$
Diameter of the inlet steam header	$d_s = 0.75 \text{ m}$
Number of steam inlet headers	$n_s = 2$
Height of the middle of the finned tube bundle above ground level	$H_6 = 22.5 \text{ m}$
Height of the fan above ground level	$H_9 = 25 \text{ m}$
Height of the collecting troughs above ground level	$H_2 = 18 \text{ m}$
Height of the top of the second stage tube bundle above ground level	$H_4 = 20 \text{ m}$
Height of the top of the drift eliminators above ground level	$H_5 = 21.5 \text{ m}$
Height of complete mixing in the plenum above ground level	$H_8 = 24 \text{ m}$
Height of the diffuser outlet above ground level	$H_{11} = 30 \text{ m}$
Diameter of the casing	$d_c = 9.17 \text{ m}$

Geometric relations and various areas

Inside area of the tube per unit length

$$A_{ti} = 2(H_t - W_t) + W_t\pi = 0.21341 \text{ m}^2$$

Inside cross-sectional tube flow area

$$A_{ts} = W_t(H_t - W_t) + \frac{1}{4}\pi W_t^2 = 1.587 \times 10^{-3} \text{ m}^2$$

Hydraulic diameter of the tube

$$d_e = 4A_{ts}/A_{ti} = 0.02975 \text{ m}^2$$

Effective frontal area of one bundle based on the second tube row,

$$A_{fr} = 0.05n_{tb2}L_t = 13.05 \text{ m}^2$$

Height of the diffuser

$$L_{dif} = 0.4d_c = 3.668 \text{ m}$$

Converged iteration parameters for the first stage

Air mass flow rate through the first stage	$m_{av67} = 408.680 \text{ kg/s}$
Mean outlet air temperature after the first tube row of the finned tube bundle	$T_{ao(b1)} = 304.445 \text{ K}$
Mean bundle outlet temperature	$T_{a7} = 319.347 \text{ K}$
Air pressure at the inlet of the heat exchanger	$p_{a6} = 84363.923 \text{ Pa}$

Performance analysis procedure for the first tube row

The corresponding humidity ratio at ambient conditions

$$w_1 = w(T_{a1}, T_{wb1}, p_a, p_v(T_{wb1})) = 6.9024 \times 10^{-3} \text{ kg H}_2\text{O/kg dry air}$$

Air temperature at the inlet of the finned tube bundle

$$T_{a6} = T_{a1} - 0.00975H_6 = 15.381 \text{ }^\circ\text{C}$$

The mean temperature through the first row of the finned bundles

$$T_{am(b1)} = (T_{a6} + T_{ao(b1)})/2 = 296.488 \text{ K}$$

The air properties at $T_{am(b1)}$

Density	$\rho_{avm(b1)} = \rho_{av}(w_1, p_{a6}, T_{am(b1)}) = 0.98706 \text{ kg/m}^3$
Specific heat	$c_{pavm(b1)} = c_{pav}(T_{am(b1)}, w_1) = 1012.8366 \text{ J/kgK}$
Dynamic viscosity	$\mu_{avm(b1)} = \mu_{av}(T_{am(b1)}, w_1) = 1.8234 \times 10^{-5} \text{ kg/ms}$
Thermal conductivity	$k_{avm(b1)} = k_{av}(T_{am(b1)}, w_1) = 0.02588 \text{ W/mK}$

The corresponding Prandtl number

$$Pr_{avm(b1)} = \frac{\mu_{avm(b1)}c_{pavm(b1)}}{k_{avm(b1)}} = 0.71364$$

The mean temperature through the second row of the finned bundles

$$T_{am(b2)} = (T_{a7} + T_{ao(b1)})/2 = 311.896 \text{ K}$$

The air properties at $T_{am(b2)}$

Density	$\rho_{avm(b2)} = \rho_{av}(w_1, p_{a6}, T_{am(b2)}) = 0.93829 \text{ kg/m}^3$
Specific heat	$c_{pavm(b2)} = c_{pav}(T_{am(b2)}, w_1) = 1013.5489 \text{ J/kgK}$
Dynamic viscosity	$\mu_{avm(b2)} = \mu_{av}(T_{am(b2)}, w_1) = 1.8938 \times 10^{-5} \text{ kg/ms}$

Thermal conductivity $k_{avm(b2)} = k_{av}(T_{am(b2)}, w_1) = 0.02707 \text{ W/mK}$

The enthalpy at the outlet of the heat exchanger

$$i_{ma7} = i_{ma}(T_{a7}, w_1) = 64379.2047 \text{ J/kg}$$

The corresponding Prandtl number

$$Pr_{avm(b2)} = \frac{\mu_{avm(b2)} c_{pavm(b2)}}{k_{avm(b2)}} = 0.70918$$

The heat transfer through the first tube row

$$Q_{a(b1)} = m_{av67} c_{pavm(b1)} (T_{ao(b1)} - T_{a6}) = 6587188.5136 \text{ W}$$

The heat transfer through the second tube row

$$Q_{a(b2)} = m_{av67} c_{pavm(b2)} (T_{a7} - T_{ao(b1)}) = 6172644.5808 \text{ W}$$

Total heat transfer rate

$$Q_{a67} = Q_{a(b1)} + Q_{a(b2)} = 12759833.09442 \text{ W}$$

Air-side characteristic flow parameter for the first tube row

$$Ry_{(b1)} = \frac{m_{av67} n_{tb2}}{\mu_{avm(b1)} A_{fr} n_b n_{tb1}} = 218449.02330 \text{ m}^{-1}$$

The characteristic heat transfer parameter for the first tube row

$$Ny_{(b1)} = 366.007945 Ry_{(b1)}^{0.433256} = 75300.1746 \text{ m}^{-1}$$

Corresponding effective heat transfer coefficient

$$h_{ae} A_{a(b1)} = k_{avm(b1)} Pr_{avm(b1)}^{0.333} n_b A_{fr} Ny_{(b1)} \frac{n_{tb1}}{n_{tb2}} = 178689.7877 \text{ W/K}$$

Properties of the condensate in the first tube row

The properties of the condensate are determined with the average vapor temperature for the first tube row. The temperature is the average of the in- and outlet vapor temperature of the steam in the tube and will be discussed in the steam-side pressure drop section.

Steam temperature $T_{v(b1)} = 334.9227 \text{ K}$

Density $\rho_{c(b1)} = \rho_w(T_{v(b1)}) = 982.2743 \text{ kg/m}^3$

Specific heat $c_{pc(b1)} = c_{pw} \left(\frac{T_{v(b1)} + 273.15}{2} \right) = 4178.252 \text{ J/kgK}$

Dynamic viscosity $\mu_{c(b1)} = \mu_w(T_{v(b1)}) = 4.5083 \times 10^{-4} \text{ kg/ms}$

Thermal conductivity $k_{c(b1)} = k_w(T_{v(b1)}) = 0.65488 \text{ W/mK}$

Latent heat $i_{fg(b1)} = i_{fg}(T_{v(b1)}) = 2354278.815 \text{ J/kg}$

Mass flow rate of steam condensed in the first tube row

$$m_{c(b1)} = Q_{a(b1)}/i_{fg(b1)} = 2.79796 \text{ kg/s}$$

The area exposed to the condensing steam in the first tube row

$$A_{c(b1)} = n_{tb1}n_bA_{ti}L_t = 437.911 \text{ m}^2$$

Overall heat transfer coefficient based on the condensing surface area

$$U_{c(b1)}H_tL_t = \frac{h_{ae}A_{a(b1)}}{2n_{tb1}n_b} = 195.9318 \text{ W/K}$$

The corresponding mass flow rate of air flowing over one side of a finned tube is

$$m_{at(b1)} = \frac{m_{av67}}{2n_{tb1}n_b} = 0.44811 \text{ kg/s}$$

Mean condensation heat transfer coefficient

$$h_{c(b1)} = 0.9245 \left[\frac{L_t k_c^3 \rho_c^2 9.81 \cos(90^\circ - \theta) i_{fg(b1)}}{\mu_c m_{at(b1)} c_{pavm(b1)} (T_{v(b1)} - T_{a6}) a_1} \right]^{0.333}$$

$$h_{c(b1)} = 14808.8185 \text{ W/m}^2\text{K}$$

with

$$a_1 = [1 - \exp\{-U_{c(b1)}H_tL_t/(m_{at(b1)}c_{pavm(b1)})\}]$$

Overall heat transfer coefficient for the first tube row

$$UA_{(b1)} = \left(\frac{1}{h_{ae}A_{a(b1)}} + \frac{1}{h_{c(b1)}A_{c(b1)}} \right)^{-1}$$

$$UA_{(b1)} = 173898.1055 \text{ W/K}$$

The effectiveness of the first condenser tube row

$$e_{(b1)} = 1 - \exp\left(\frac{-UA_{(b1)}}{m_{av67}c_{pavm(b1)}}\right)$$

$$e_{(b1)} = 0.34303$$

The heat transfer for the first tube row is then

$$Q_{a(b1)} = m_{av67}c_{pavm(b1)}(T_{v(b1)} - T_{a6})e_{(b1)} = 6587188.5136 \text{ W}$$

The difference between the value above and the previously calculated value for $Q_{a(b1)}$ is less than 1×10^{-7} indicating convergence.

Similar procedure for the performance of the second tube row

Air-side characteristic flow parameter for the second tube row

$$Ry_{(b2)} = \frac{m_{av67}}{\mu_{avm(b2)} A_{fr} n_b} = 206704.3859 \text{ m}^{-1}$$

The characteristic heat transfer parameter

$$Ny_{(b2)} = 360.588007 Ry_{(b2)}^{0.470373} = 114079.6706 \text{ m}^{-1}$$

Corresponding effective heat transfer coefficient

$$h_{ae} A_{a(b2)} = k_{avm(b2)} Pr_{avm(b2)}^{0.333} n_b A_{fr} Ny_{(b2)} = 287496.4974 \text{ W/K}$$

Properties of the condensate in the second tube row

Again, the properties of the condensate are determined from the average of the calculated inlet and outlet vapor temperature of the steam in the second tube row similar to the first tube row.

Steam temperature	$T_{v(b2)} = 335.0980 \text{ K}$
Density	$\rho_{c(b2)} = \rho_w(T_{v(b2)}) = 982.1800 \text{ kg/m}^3$
Specific heat	$c_{pc(b2)} = c_{pw}\left(\frac{T_{v(b2)}+273.15}{2}\right) = 4178.220 \text{ J/kgK}$
Dynamic viscosity	$\mu_{c(b2)} = \mu_w(T_{v(b2)}) = 4.4964 \times 10^{-4} \text{ kg/ms}$
Thermal conductivity	$k_{c(b2)} = k_w(T_{v(b2)}) = 0.65504 \text{ W/mK}$
Latent heat	$i_{fg(b2)} = i_{fg}(T_{v(b2)}) = 2353848.7708 \text{ J/kg}$

Mass flow rate of steam condensed in the second tube row

$$m_{c(b2)} = Q_{a(b2)} / i_{fg(b2)} = 2.62236 \text{ kg/s}$$

The area exposed to the condensing steam in the second tube row

$$A_{c(b2)} = n_{tb2} n_b A_{ti} L_t = 445.594 \text{ m}^2$$

Overall heat transfer coefficient based on the condensing surface area

$$U_{c(b2)} H_t L_t = \frac{h_{ae} A_{a(b2)}}{2 n_{tb2} n_b} = 309.8023 \text{ W/K}$$

The corresponding mass flow rate of air flowing over one side of a finned tube is

$$m_{at(b2)} = \frac{m_{av67}}{2 n_{tb2} n_b} = 0.44039 \text{ kg/s}$$

Mean condensation heat transfer coefficient

$$h_{c(b2)} = 0.9245 \left[\frac{L_t k_c^3 \rho_c^2 9.81 \cos(90^\circ - \theta) i_{fg(b2)}}{\mu_c m_{at(b2)} c_{pavm(b2)} (T_{v(b2)} - T_{ao(b1)}) a_2} \right]^{0.333}$$

$$h_{c(b2)} = 15199.37877 \text{ W/m}^2\text{K}$$

with

$$a_2 = [1 - \exp\{-U_{c(b2)} H_t L_t / (m_{at(b2)} c_{pavm(b2)})\}]$$

Overall heat transfer coefficient for the second tube row

$$UA_{(b2)} = \left(\frac{1}{h_{ae} A_{a(b2)}} + \frac{1}{h_{c(b2)} A_{c(b2)}} \right)^{-1}$$

$$UA_{(b2)} = 275789.5099 \text{ W/K}$$

The effectiveness of the second condenser tube row

$$e_{(b2)} = 1 - \exp\left(\frac{-UA_{(b2)}}{m_{av67} c_{pavm(b2)}}\right)$$

$$e_{(b2)} = 0.48614$$

The heat transfer for the second tube row is then

$$Q_{a(b2)} = m_{av67} c_{pavm(b2)} (T_{v(b2)} - T_{ao(b1)}) e_{(b2)} = 6172644.5808 \text{ W}$$

Convergence is reached since the difference between the value above and the previously calculated value for $Q_{a(b2)}$ is less than 1×10^{-7} .

B.1.2 The second stage (bare tube) section

The steam temperature for the tube bundle, T_{vtb} , is a weighted average of the steam temperatures for the three passes and is 62.4083 °C or 335.5583 K. The amount of steam condensed in the tube bundles of one dephlegmator consisting of 8 bundles is 17.7916 kg/s.

The deluge water mass flow rate for eight bundles
Spray zone height

$$m_{dw} = 106 \text{ kg/s}$$

$$L_{sz} = 0.95 \text{ m}$$

Physical properties of the tube bundles

Number of tube rows
Rows of tubes in the first pass
Rows of tubes in the second pass
Rows of tubes in the third and final pass
Tubes per row
Thermal conductivity of the tube wall

$$n_{tbr} = 25$$

$$n_{hr1} = 20$$

$$n_{hr2} = 4$$

$$n_{hr3} = 1$$

$$n_{tr} = 75$$

$$k_t = 43 \text{ W/mK}$$

Tube length	$L_{tb} = 2.5 \text{ m}$
Transverse pitch	$P_t = 0.038 \text{ m}$
Longitudinal pitch	$P_l = 0.0329 \text{ m}$
Outer diameter of the tubes	$d_o = 0.019 \text{ m}$
Inner diameter of the tubes	$d_i = 0.0158 \text{ m}$

Geometric relations and various areas

Minimum air flow area and frontal area through one tube bundle is respectively

$$A_c = (n_{tr} + 0.5)(P_t - d_o)L_{tb} = 3.586 \text{ m}^2$$

and

$$A_{tbfr} = (n_{tr} + 0.5)P_tL_{tb} = 7.1725 \text{ m}^2$$

The effective air-side surface area of one bundle is calculated as

$$A_o = \pi d_o L_{tb} n_{tr} n_{tbr} = 279.798 \text{ m}^2$$

Total inner tube condensing surface area

$$A_i = \pi d_i n_{tr} n_{tbr} L_{tb} = 232.674 \text{ m}^2$$

The cross-sectional area of the tube is

$$A_{tbts} = \frac{\pi}{4} d_i^2 = 1.961 \times 10^{-4} \text{ m}^2$$

Converged iteration parameters for the plain tube bundles

Air vapor mass flow at the inlet of the tube bundle	$m_{av34} = 149.396 \text{ kg/s}$
Steam condensed in eight bundles of one dephlegmator	$m_{ctb} = 17.7916 \text{ kg/s}$
The inner wall temperature of the tubes	$T_{wi} = 60.9608 \text{ }^\circ\text{C}$
Mean deluge water temperature	$T_{dwm} = 51.088 \text{ }^\circ\text{C}$
Saturated outlet air temperature	$T_{a4} = 49.2483 \text{ }^\circ\text{C}$

Performance analysis of the second stage tube bundles

The geodetic pressure and temperature at point 3 below the collecting troughs ($H_3 = H_2$)

$$p_{a3} = p_{a1} \left(1 - 0.00975 \frac{H_2}{T_{a1}} \right)^{3.5} = 84420.169 \text{ Pa}$$

and

$$T_{a3} = T_{a1} - 0.00975 H_2 = 15.425 \text{ }^\circ\text{C}$$

The humidity ratio at the inlet of the tube bundle

$$w_3 = w(T_{a3}, T_{wb1}, p_{a3}, p_v(T_{wb1})) = 6.9940 \times 10^{-3} \text{ kg H}_2\text{O/ kg dry air}$$

The corresponding enthalpy of the inlet air

$$i_{ma3} = i_{ma}(T_{a3}, w_3) = 33400.552 \text{ J/kg}$$

In order to calculate the enthalpy of the air at the mean deluge water temperature, the saturated humidity at the deluge water temperature is calculated as follows,

$$w_{sdwm} = w(T_{dwm}, T_{dwm}, p_{a3}, p_v(T_{dwm}))$$

$$w_{sdwm} = 0.11410 \text{ kg H}_2\text{O/ kg dry air}$$

with the enthalpy,

$$i_{masdwm} = i_{ma}(T_{dwm}, w_{sdwm}) = 347850.8605 \text{ J/kg}$$

For the transfer characteristics of Mizushina et al. (1967) the mean temperature and humidity need to be determined. Therefore the mean air temperature over the tube bundle,

$$T_{a34} = 0.5(T_{a3} + T_{a4}) = 32.3364 \text{ }^\circ\text{C}$$

The temperatures at 4 and 5 are the same, since it is adiabatic flow over the drift eliminators. The saturated humidity ratio at the outlet of the tube bundle,

$$w_{s4} = w(T_{a4}, T_{a4}, p_{a3}, p_v(T_{a4})) = 0.102514 \text{ kg H}_2\text{O/kg dry air}$$

The average humidity ratio over the tube bundle is then,

$$w_{34} = 0.5(w_3 + w_{s4}) = 0.05475 \text{ kg H}_2\text{O/kg dry air}$$

The average viscosity of air at the mean conditions,

$$\mu_{av34} = \mu_{av}(T_{a34}, w_{34}) = 1.81682 \times 10^{-5} \text{ kg/ms}$$

The Reynolds number of the air flowing through tube bundle

$$Re_{av34} = \frac{m_{av34} d_o}{n_b A_c \mu_{av34}} = 5445.6450$$

A uniform water distribution over the tube bundle, along with negligible evaporation of deluge water is assumed in the following analysis. The water flow rate over one half of tube per unit length is

$$\Gamma_m = \frac{m_{dw} d_o}{2n_b n_{tr} P_t L_{tb}} = 0.01767 \text{ kg/ms}$$

The viscosity of the deluge water evaluated at the mean deluge water temperature

$$\mu_{dwm} = \mu_w(T_{dwm}) = 5.3424 \times 10^{-4} \text{ kg/ms}$$

This yields the Reynolds number of the deluge water over the tube bank

$$Re_{dwm} = \frac{4\Gamma_m}{\mu_{dwm}} = 132.27528$$

The mass transfer coefficient according to the relation of Mizushima et al. (1967) as quoted in Eq. (A.14),

$$h_d = 5.5439 \times 10^{-8} Re_{av34}^{0.9} Re_{dwm}^{0.15} d_o^{-1.6} = 0.15083 \text{ kg/m}^2\text{s}$$

The dry air mass flow for all eight bundles

$$m_{a34} = \frac{m_{av34}}{1+w_3} = 148.358 \text{ kg/s}$$

The number of transfer units for the air side can be determined as follows

$$NTU_a = \frac{n_b A_o h_d}{m_{a34}} = 2.27562$$

From this the outlet air enthalpy is expressed as

$$i_{ma4} = i_{masdwm} - (i_{masdwm} - i_{mai})e^{-NTU_a} = 315546.2577 \text{ J/kg}$$

The specific heat of dry air and vapor at the outlet temperature

$$\text{Specific heat of air} \quad c_{pa4} = c_{pa} \left(\frac{T_{a4}}{2} + 273.15 \right) = 1006.8754 \text{ J/kgK}$$

$$\text{Specific heat of vapor} \quad c_{pv4} = c_{pv} \left(\frac{T_{a4}}{2} + 273.15 \right) = 1883.830 \text{ J/kgK}$$

The outlet air temperature can be confirmed by using the following formula

$$T_{a4} = \frac{i_{ma4} - w_{s4} i_{fg0}}{c_{pa4} + w_{s4} c_{pv4}} = 49.2483 \text{ }^\circ\text{C}$$

The heat transfer to the air from the eight tube bundles

$$Q_{atb} = m_{a34}(i_{ma4} - i_{ma3}) = 41858625.8521 \text{ W}$$

The convective heat transfer coefficient between the film and the outer surface of the tubes is determined by the correlation supplied by Mizushima et al. (1967) as quoted in Eq. (A.15)

$$h_{dw} = 2102.9 \left(\frac{\Gamma_m}{d_o} \right)^{0.333} = 2052.5614 \text{ W/m}^2\text{K}$$

Properties of the condensate in the plain tube bundle

$$\text{Density} \quad \rho_{ctb} = \rho_w(T_{vtb} + 273.15) = 981.9316 \text{ kg/m}^3$$

Specific heat	$c_{pctb} = c_{pw} \left(\frac{T_{vtb}}{2} + 273.15 \right) = 4178.1381 \text{ J/kgK}$
Dynamic viscosity	$\mu_{ctb} = \mu_w(T_{vtb} + 273.15) = 4.4656 \times 10^{-4} \text{ kg/ms}$
Thermal conductivity	$k_{ctb} = k_w(T_{vtb} + 273.15) = 0.65547 \text{ W/mK}$
Latent heat	$i'_{fgtb} = i_{fg}(T_{vtb} + 273.15) = 2352719.3952 \text{ J/kg}$

The corresponding Prandtl number

$$Pr_{ctb} = \frac{\mu_{ctb} c_{pctb}}{k_{ctb}} = 2.8465$$

Properties of the vapor in the plain tube bundle

Density	$\rho_{vtb} = \rho_v(T_{vtb} + 273.15) = 0.14447 \text{ kg/m}^3$
Specific heat	$c_{pvtb} = c_{pv} \left(\frac{T_{vtb}}{2} + 273.15 \right) = 1890.09877 \text{ J/kgK}$
Dynamic viscosity	$\mu_{vtb} = \mu_v(T_{vtb} + 273.15) = 1.1159 \times 10^{-5} \text{ kg/ms}$
Vapor pressure	$p_{vtb} = p_v(T_{vtb} + 273.15) = 22254.0511 \text{ Pa}$
Critical pressure	$p_{cr} = 22.09 \times 10^6 \text{ Pa}$

Chato (1962) proposed a procedure to calculate the condensate heat transfer coefficient for near horizontal tubes. The following equation is the equation for condensation in horizontal tubes with low Reynolds numbers (<35000). The effect of the slight slope of the tubes is found to be negligible.

$$Re_{vtb} = \frac{m_{ctb} d_i}{n_b n_{hr1} n_{tr} A_{tbts} \mu_{vtb}} = 10706.6362$$

With the converged inner wall temperature $T_{wi} = 60.9608 \text{ }^\circ\text{C}$, the condensation heat transfer coefficient can be determined

$$h_c = 0.555 \left[\frac{9.8 \rho_{ctb} (\rho_{ctb} - \rho_{vtb}) k_{ctb}^3 i'_{fgtb}}{\mu_{ctb} (T_{vtb} - T_{wi}) d_i} \right]^{0.25}$$

$$h_c = 15535.80213 \text{ W/m}^2\text{K}$$

with $i'_{fgtb} = i_{fgtb} + 0.68 c_{pctb} (T_{vtb} - T_{wi})$. The confirmed wall temperature,

$$T_{wi} = T_{vtb} - Q_{atb} / (n_b A_i h_c) = 60.9608 \text{ }^\circ\text{C}$$

The overall heat transfer coefficient between the steam and the water film on the outer surface of the tubes

$$UA_o = n_b A_o \left[\frac{1}{h_{dw}} + \frac{d_o}{d_i h_c} + \frac{d_o \ln \left(\frac{d_o}{d_i} \right)}{2k_t} \right]^{-1}$$

$$UA_o = 3697694.8671 \text{ W/K}$$

The mean deluge water temperature can be determined as

$$T_{dwm} = T_{vtb} - (m_{a34}/UA_o)(i_{ma4} - i_{ma3}) = 51.088 \text{ }^\circ\text{C}$$

The amount of water evaporated

$$m_{evap} = m_{a34}(w_{s4} - w_3) = 14.1712 \text{ kg/s}$$

The amount of steam condensed in the second stage of one dephlegmator with eight bundles

$$m_{ctb} = Q_{atb}/i_{fgtb} = 17.7916 \text{ kg/s}$$

B.2 Evaluation of the draft equation for the dephlegmator system

The draft equation for the dephlegmator is solved by solving all the resistances depicted in Figure B.2. Thereafter the analysis entails determining the pressure at point 8 through each of the three fluid paths and iterating the flow rates until the pressure at point 8 converges. A uniform velocity is assumed at point 8. The resistance to turn the flow through 90° at the inlet of the second stage bundle is neglected and normal flow approach is assumed for the dephlegmator.

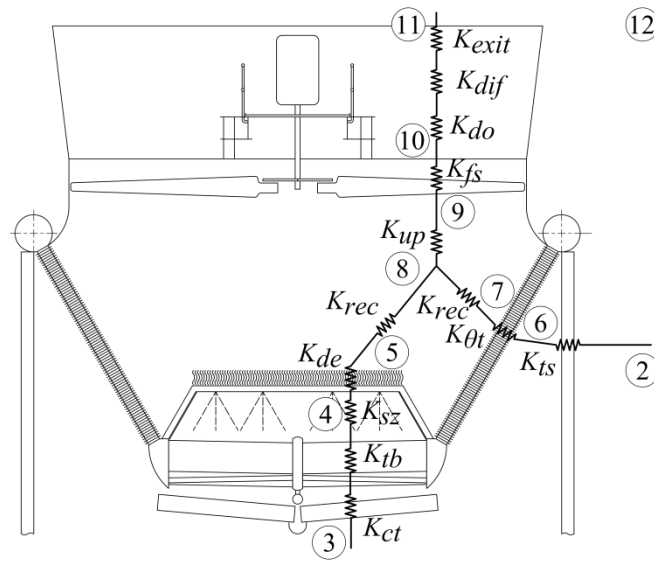


Figure B.2: Dephlegmator with the flow resistances indicated for the draft equation

Converged iteration parameters for this section

Pressure at point 6	$p_{a6} = 84363.923 \text{ Pa}$
Pressure at point 4	$p_{a4} = 84229.818 \text{ Pa}$
Pressure at point 8	$p_{a8} = 84203.169 \text{ Pa}$
Temperature at point 8	$T_{a8} = 47.115 \text{ }^\circ\text{C}$

B.2.1 The first stage (finned tube) section

The air temperature at the heat exchanger inlet height is $T_{a6} = 288.531$ K. The ratio of minimum to free flow area through the heat exchanger is $\sigma_{min} = 0.48$. The average air temperature over the finned tube bundles is

$$T_{a67} = 0.5(T_{a6} + T_{a7}) = 303.939 \text{ K}$$

The humidity ratio at point 6 and 7 is equal to point 1 because no additional water has been added to the air stream, thus $w_6 = w_7 = w_1$. The viscosity of air at this mean temperature over the finned tube bundles

$$\mu_{av67} = \mu_{av}(T_{a67}, w_6) = 1.8576 \times 10^{-5} \text{ kg/ms}$$

The characteristic flow parameter is

$$Ry = \frac{m_{av67} n_{tb2}}{n_b A_{fr} \mu_{av67} n_{tb1}}$$

$$Ry = 214430.272 \text{ m}^{-1}$$

The isothermal air-side loss coefficient for the finned tube bundles

$$K_{he} = 4177.08481 Ry^{-0.4392686} = 19.011$$

The air density at point 6 and 7, the in- and outlet of the finned tube bundle section, is respectively,

$$\rho_{av6} = \rho_{av}(w_6, p_{a6}, T_{a6}) = 1.01428 \text{ kg/m}^3$$

and

$$\rho_{av7} = \rho_{av}(w_6, p_{a6}, T_{a7}) = 0.91640 \text{ kg/m}^3$$

The pressure at point 6 is used to determine the density at point 7 to eliminate the need for another iteration parameter. The density is not a strong function of pressure and a negligible error is induced. The average density across the finned tube section is,

$$\rho_{av67} = 2(\rho_{av6}^{-1} + \rho_{av7}^{-1})^{-1} = 0.96286 \text{ kg/m}^3$$

With a loss coefficient for the tower supports of $K_{ts} = 1.5$ based on the frontal area of the finned tube bundles, the pressure at point 6 can be confirmed as

$$p_{a6} = p_{a1} \left(1 - 0.00975 \frac{H_6}{T_{a1}} \right)^{3.5} - K_{ts} \left(\frac{m_{av67}}{A_{fr} n_b} \right)^2 \frac{1}{2\rho_{av6}}$$

$$p_{a6} = 84363.923 \text{ Pa}$$

The acceleration effects over the finned tube bundles can be taken into account with the calculated densities at point 6 and 7. A uniform outlet velocity at point 7 is assumed, therefore the kinetic energy correction factor $\alpha_e = 1$. The total finned tube bundle loss coefficient,

$$K_{\theta t} = K_{he} + \frac{2}{\sigma_{min}^2} \frac{\rho_{av6} - \rho_{av7}}{\rho_{av6} + \rho_{av7}} + \frac{2\rho_{av6}\alpha_e}{\rho_{av6} + \rho_{av7}}$$

$$K_{\theta t} = 20.5018$$

The dry air mass flow rate through the finned tube bundles of the dephlegmator

$$m_{a67} = \frac{m_{av67}}{1+w_1} = 405.878 \text{ kg/s}$$

The pressure at point 7 at the outlet of the finned tube bundles

$$p_{a7} = p_{a6} - K_{\theta t} \left(\frac{m_{av67}}{n_b A_{fr}} \right)^2 \frac{1}{2\rho_{av67}}$$

$$p_{a7} = 84200.782 \text{ Pa}$$

The plenum recovery coefficient, $K_{rec} = 0.3$, is the last resistance before the complete mixing of the two streams occur. Therefore the pressure at point 8 through the dry section

$$p_{a8} = p_{a7} + K_{rec} \left(\frac{m_{av67}}{A_{fr} n_b} \right)^2 \frac{1}{2\rho_{av67}}$$

$$p_{a8} = 84203.169 \text{ Pa}$$

B.2.2 The second stage (bare tube) section

The pressure at point 3 below the collecting troughs is the same as at point 2. It is only the geodetic pressure that is accounted for and is previously calculated as $p_{a3} = 84420.169 \text{ Pa}$. The converged mass flow rate of air through the bundle is $m_{av34} = 149.396 \text{ kg/s}$ and the corresponding dry air mass flow rate is $m_{a34} = 148.358 \text{ kg/s}$. The mass flow rate of the deluge water over the tube bundle is $m_{dw} = 106 \text{ kg/s}$. The dry air mass velocity through the tube bundle is

$$G_{a34} = \frac{m_{a34}}{A_{tbfr} n_b} = 2.5855 \text{ kg/m}^2\text{s}$$

The deluge water mass velocity is

$$G_{dw} = \frac{m_{dw}}{A_{tbfr} n_b} = 1.8473 \text{ kg/m}^2\text{s}$$

The dry air mass velocity is lower than $G_a = 3 \text{ kg/m}^2\text{s}$ which is the reported point of flooding for this specific bundle configuration. The deluge water mass velocity

should be above $G_{dw} = 1.5 \text{ kg/m}^2\text{s}$ to ensure proper wetting of the tubes which makes the current flow rates acceptable.

The relation obtained by Bertrand (2011) for the pressure drop over the collecting troughs is defined as

$$\Delta p_{trw} = 1.563 G_{dw}^{0.184} G_{a34}^{1.693} = 8.7388 \text{ Pa}$$

The density and viscosity at point 4

$$\begin{aligned} \text{Density} \quad \rho_{av4} &= \rho_{av}(w_{s4}, p_{a4}, T_{a4}) = 0.86138 \text{ kg/m}^3 \\ \text{Dynamic viscosity} \quad \mu_{av4} &= \mu_{av}(T_{a4}, w_{s4}) = 5.0914 \times 10^{-6} \text{ kg/ms} \end{aligned}$$

The inlet mass flow rate for the tube bundle is $m_{av3} = m_{av34} = 149.396 \text{ kg/s}$ and with the density at point 3,

$$\rho_{av3} = \rho_{av}(w_3, p_{a3}, T_{a3}) = 1.01474 \text{ kg/m}^3$$

The inlet velocity

$$v_{av3} = m_{av3} / (\rho_{av3} n_b A_{tbfr}) = 2.5658 \text{ m/s}$$

The outlet mass flow rate and velocity is respectively

$$m_{av4} = m_{a34}(1 + w_{s4}) = 163.567 \text{ kg/s}$$

and

$$v_{av4} = m_{av4} / (\rho_{av4} n_b A_{tbfr}) = 3.3093 \text{ m/s}$$

The mean mass flow rate and density through the tube bundle,

$$m_{avm34} = 0.5(m_{av3} + m_{av4}) = 156.481 \text{ kg/s}$$

with the mean density

$$\rho_{av34} = 2(\rho_{av3}^{-1} + \rho_{av4}^{-1})^{-1} = 0.93179 \text{ kg/m}^3$$

The critical mass velocity through the tube bundle

$$G_{c34} = G_{a34} A_{tbfr} / A_c = 5.1711 \text{ kg/m}^2\text{s}$$

The tube bundle loss coefficient obtained from experiments in the current study as quoted in Eq. (5.10)

$$K_{tb} = 52.6716 \left(\frac{\Gamma_m}{d_o} \right)^{0.19307} G_c^{-0.089713}$$

$$K_{tb} = 44.8186$$

The pressure drop over the tube bundle

$$\Delta p_{tb} = \frac{K_{tb} m_{avm34}^2}{2\rho_{av34} (n_b A_{tbfr})^2} + \rho_{av4} v_{av4}^2 - \rho_{av3} v_{av3}^2$$

$$\Delta p_{tb} = 181.6128 \text{ Pa}$$

With the length and the width of the drift eliminator sections being $L_{de} = 2.05 \text{ m}$ and $W_{de} = 2.9 \text{ m}$, the frontal area of the drift eliminators can be determined

$$A_{frde} = L_{de} W_{de} = 5.945 \text{ m}^2$$

The characteristic flow parameter for the drift eliminators

$$Ry_{de} = m_{av34} / (n_b A_{frde} \mu_{av4}) = 616966.0114 \text{ m}^{-1}$$

Loss coefficient for the drift eliminators as proposed by Kröger (2004)

$$K_{de} = 27.4892 Ry_{de}^{-0.14247} = 4.1136$$

The loss coefficient of the spray zone as proposed by Cale (1982) and documented in Kröger (2004)

$$K_{sz} = L_{sz} \left[0.4 \left(\frac{G_{dw}}{G_{a34}} \right) + 1 \right] = 1.2215$$

The pressure drop over the drift eliminators

$$\Delta p_{de} = K_{de} \left(\frac{m_{av34}}{A_{frde} n_b} \right)^2 \frac{1}{2\rho_{av4}}$$

$$\Delta p_{de} = 23.5608 \text{ Pa}$$

The pressure drop over the spray zone

$$\Delta p_{sz} = K_{sz} \left(\frac{m_{av34}}{A_{tbfr} n_b} \right)^2 \frac{1}{2\rho_{av4}}$$

$$\Delta p_{sz} = 4.8065 \text{ Pa}$$

The kinetic energy recovery at the top of the drift eliminators

$$\Delta p_{ke} = -K_{rec} \left(\frac{m_{av34}}{A_{frde} n_b} \right)^2 \frac{1}{2\rho_{av4}}$$

$$\Delta p_{ke} = -1.7183 \text{ Pa}$$

The confirmed pressure at point 4 at the top of the tube bundle

$$p_{a4} = p_{a3} - \Delta p_{tb} - \Delta p_{trw} = 84229.818 \text{ Pa}$$

The pressure at point 8 through the tube bundle section

$$p_{a8} = p_{a4} - \Delta p_{sz} - \Delta p_{de} - \Delta p_{ke} = 84203.169 \text{ Pa}$$

B.2.3 The mixed section

The mass flow rate at point 8

$$m_{av8} = m_{a34}(1 + w_{s4}) + m_{a67}(1 + w_6) = 572.2467 \text{ kg/s}$$

The corresponding humidity ratio at point 8

$$w_8 = \frac{w_{s4}m_{a34} + w_6m_{a67}}{m_{a34} + m_{a67}}$$

$$w_8 = 0.03250 \text{ kg H}_2\text{O/kg dry air}$$

The enthalpy at point 8, ($i_{ma4} \approx i_{ma5}$)

$$i_{ma8} = \frac{i_{ma4}m_{a34} + i_{ma7}m_{a67}}{m_{a34} + m_{a67}}$$

$$i_{ma8} = 131611.6862 \text{ J/kg}$$

At point 8,

Specific heat of air $c_{pa8} = c_{pa} \left(\frac{T_{a8}}{2} + 273.15 \right) = 1006.8399 \text{ J/kgK}$

Specific heat of vapor $c_{pv8} = c_{pv} \left(\frac{T_{a8}}{2} + 273.15 \right) = 1882.8555 \text{ J/kgK}$

With the specific heats determined, the air temperature at point 8 can be calculated,

$$T_{a8} = \frac{i_{ma8} - w_8 i_{fg0}}{c_{pa8} + w_8 c_{pv8}}$$

$$T_{a8} = 47.1154 \text{ }^\circ\text{C}$$

After the mixing section the air continues through the safety screens below the fan with a resistance of $K_{up} = 0.1317$ and above the fan there is again safety screens and support beams with resistances of $K_{so} = 0.2324$ and $K_{bo} = 0.1584$ respectively. The total downstream losses is then,

$$K_{do} = K_{so} + K_{bo} = 0.3908$$

The pressure drop over these obstacles is based on the effective area of air flow through the fan section. The effective area is defined for a hub diameter of $d_h = 1.4 \text{ m}$ as,

$$A_e = \frac{\pi}{4}(d_c^2 - d_h^2) = 64.504 \text{ m}^2$$

Kröger (2004) proposed a practical diffuser with a diameter at the outlet to be calculated as $d_{difo} = 1.1d_c = 10.087 \text{ m}$ with a conservative efficiency of $\eta_{dif} = 0.8$. The area ratio of the diffuser is the cross-sectional area at the outlet over the cross-sectional area of the fan casing.

$$n_1 = A_{difo}/A_{fc} \text{ with } A_{difo} = \frac{\pi}{4}d_{difo}^2 \text{ and } A_{fc} = \frac{\pi}{4}d_c^2$$

Thus,

$$n_1 = A_{difo}/A_{fc} = 1.21 \text{ m}^2$$

The loss coefficient for the diffuser as defined in Fried & Idelchik (1989) is

$$K_{dif} = \frac{1 - \eta_{dif}}{1 - n_1^{-2}}$$

$$K_{dif} = 0.63094$$

With the density at point 8,

$$\rho_{av8} = \rho_{av}(w_8, p_{a8}, T_{a8} + 273.15) = 0.89864 \text{ kg/m}^3$$

the volumetric flow rate through the fan can be determined

$$V_{av8} = m_{av8}/\rho_{av8} = 636.791 \text{ m}^3/\text{s}$$

The fan static pressure at a reference density of 1.2 kg/m^3 can be approximated by the following correlation

$$\Delta p_{f(1.2)} = 320.0451719 - 0.2975215484V_{av8} + 6.351486 \\ \times 10^{-4}V_{av8}^2 - 8.14 \times 10^{-7}V_{av8}^3$$

The fan static pressure for this specific case with the density adapted, is then

$$\Delta p_f = \frac{\rho_{av8}}{1.2} \Delta p_{f(1.2)} = 133.2606 \text{ Pa}$$

The geodetic pressure at point 11 at the diffuser outlet at a height of 30 m

$$p_{a11} = p_{a1} \left(1 - 0.00975 \frac{H_{11}}{T_{a1}} \right)^{3.5}$$

$$p_{a11} = 84300.434 \text{ Pa}$$

The pressure at point 8 through the fan section

$$p_{a8} = p_{a11} - \Delta p_f + \alpha_e \left(\frac{1}{A_{dif0}^2} - \frac{1}{A_{fc}^2} \right) \frac{m_{av8}^2}{2\rho_{av8}} + (K_{up} + K_{do}) \left(\frac{m_{av8}}{A_e} \right)^2 \frac{1}{2\rho_{av8}} + K_{dif} \left(\frac{m_{av8}}{A_{fc}} \right)^2 \frac{1}{2\rho_{av8}}$$

$$p_{a8} = 84203.169 \text{ Pa}$$

This value for the pressure at point 8 agrees well with the other two calculated values indicating convergence. The error is less than 1×10^{-7} .

B.3 The steam side pressure drop

The following is a method of analysis proposed by Groenewald & Kröger (1995) who investigated the pressure drop in finned flattened tubes for condenser applications. Relations for the frictional pressure drop for the flattened tubes and pipes are supplied. This makes it ideal correlations to use, since the first stage of finned tubes is geometrically similar to those Groenewald & Kröger tested and the second stage bundle consist of plain round tubes. Lips & Meyer (2011) did a thorough survey of two phase flow in inclined tubes and no correlations for condensation in 19 mm tubes were found. The correlations of Groenewald & Kröger (1995) are deemed satisfactory, since Owen (2013) used these correlations in a similar analysis.

B.3.1 The first stage (finned tube) section

All the steam condensed in the dephlegmator is sucked through the inlet of the first stage of finned tube bundles of the dephlegmator. This total steam is

$$m_{vtot} = m_{c(b1)} + m_{c(b2)} + m_{ctb} = 23.2119 \text{ kg/s}$$

Figure B.3 shows a sectioned view of the dephlegmator. The Roman numerals indicate positions along the flow path where the pressure of the steam is calculated. The mass flow rate flowing in tube row 1 and 2 of the first stage is iterated until the static pressure at point (iv) converges to the same value. It is assumed that the velocities from the two streams from the two tube rows are the same in the header at point (iv) and complete mixing occurred. The amount of steam entering one flattened tube in the second tube row in the finned tube section converged to $m_{v(ii)(b2)} = 0.023946 \text{ kg/s}$. From continuity the mass flow rate of steam in the first tube row,

$$m_{v(ii)(b1)} = \frac{m_{vtot} - m_{v(ii)(b2)}n_b n_{tb2}}{n_b n_{tb1}}$$

$$m_{v(ii)(b1)} = 0.026537 \text{ kg/s}$$

The vapor temperature at the inlet header, $T_{v(i)}$, is taken as $60 \text{ }^\circ\text{C}$. The static pressure at this point is the vapor pressure

$$p_{v(i)} = p_v(T_{v(i)}) = 19925.116 \text{ Pa}$$

The dynamic pressure at (i) with $m_{v(i)} = m_{vtot}$ and $\rho_{v(i)} = \rho_v(T_{v(i)}) = 0.130231 \text{ kg/m}^3$

$$p_{d(i)} = \frac{1}{2} \rho_{v(i)} \left(\frac{m_{v(i)}}{\rho_{v(i)} 0.25 \pi d_s^2 n_s} \right)^2 = 2649.6836 \text{ Pa}$$

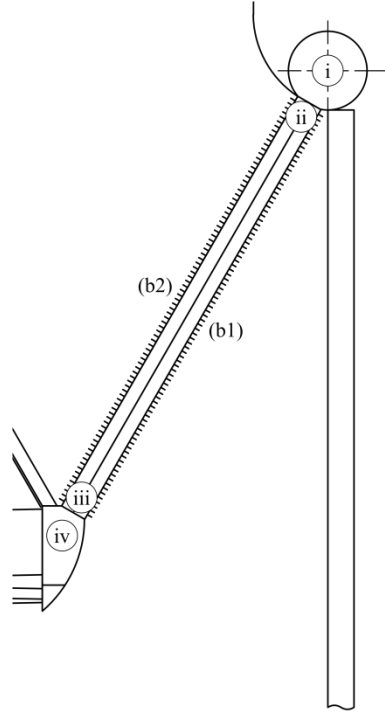


Figure B.3: First stage steam-side pressure drop

The total pressure at (i)

$$p_{t(i)} = p_{d(i)} + p_{v(i)} = 22574.7997 \text{ Pa}$$

The contraction ratio for parallel plates with an area ratio $\sigma_{(ii)(i)} = 0.5$

$$\begin{aligned} \sigma_c = & 0.6144517 + 0.04566493\sigma_{(ii)(i)} - 0.336651\sigma_{(ii)(i)}^2 \\ & + 0.4082743\sigma_{(ii)(i)}^3 + 2.672041\sigma_{(ii)(i)}^4 \\ & - 5.963169\sigma_{(ii)(i)}^5 + 3.558944\sigma_{(ii)(i)}^6 \end{aligned}$$

$$\sigma_c = 0.640418$$

The inlet loss coefficient due to the contraction

$$K_c = (1 - \sigma_c^{-1})^2 = 0.315261$$

The analysis for tube row 1

The saturated vapor temperature at (ii) calculated with the converged static pressure at (ii)

$$T_{v(ii)(b1)} = T_s(p_{v(ii)(b1)}) = 61.3833 \text{ }^\circ\text{C}$$

Properties of the vapor at (ii)

Density $\rho_{v(ii)(b1)} = \rho_v(T_{v(ii)(b1)}) = 0.13826 \text{ kg/m}^3$

Dynamic viscosity $\mu_{v(ii)(b1)} = \mu_v(T_{v(ii)(b1)}) = 1.1127 \times 10^{-5} \text{ kg/ms}$

The inlet velocity at (ii)

$$v_{v(ii)(b1)} = \frac{m_{v(ii)(b1)}}{\rho_{v(ii)(b1)} A_{ts}}$$

$$v_{v(ii)(b1)} = 120.9430 \text{ m/s}$$

The total pressure at (ii)

$$p_{t(ii)(b1)} = p_{t(i)} - 0.5K_c \rho_{v(ii)(b1)} v_{v(ii)(b1)}^2 = 22256.0157 \text{ Pa}$$

The dynamic pressure at (ii)

$$p_{d(ii)(b1)} = 0.5 \rho_{v(ii)(b1)} v_{v(ii)(b1)}^2 = 1011.1758 \text{ Pa}$$

The static pressure at (ii)

$$p_{v(ii)(b1)} = p_{t(ii)(b1)} - p_{d(ii)(b1)} = 21244.8399 \text{ Pa}$$

The converged temperature at (iii) calculated from the pressure at this point

$$T_{v(iii)(b1)} = T_s(p_{v(iii)(b1)}) = 62.1621 \text{ }^\circ\text{C}$$

The average vapor temperature for tube row 1

$$T_{v(b1)} = 0.5(T_{v(ii)(b1)} + T_{v(iii)(b1)}) = 61.7727 \text{ }^\circ\text{C}$$

This is the temperature at which the thermo-physical properties are determined for the thermal analysis of the first stage of the dephlegmator as explained in Section B.1.1. The enthalpy of the condensate is then

$$i_{c(b1)} = c_{pw} \left(\frac{T_{v(b1)}}{2} + 273.15 \right) T_{v(b1)}$$

$$i_{c(b1)} = 258101.85709 \text{ J/kg}$$

and the enthalpy of the vapor

$$i_{v(b1)} = i_{c(b1)} + i_{fg}(T_{v(b1)}) = 2612380.67180 \text{ J/kg}$$

The pressure drop over the tube is dependent on the vapor quality at the end of the tube. Therefore,

$$x_{(iii)(b1)} = \frac{i_{v(b1)} - \frac{Q_{a(b1)}}{n_b m_{v(ii)(b1)} n_{tb1}} - i_{c(b1)}}{i_{v(b1)} - i_{c(b1)}}$$

$$x_{(iii)(b1)} = 0.76878$$

The flow in the flattened tubes can be approximated as parallel plates. The hydraulic diameter for parallel plates is,

$$d_{fh} = 2W_t = 0.034 \text{ m}$$

The Reynolds number of the vapor at (ii)

$$Re_{v(ii)(b1)} = \frac{\rho_{v(ii)(b1)} d_{fh} v_{v(ii)(b1)}}{\mu_{v(ii)(b1)}} = 51096.8239$$

The mass flow rate of the vapor at (iii)

$$m_{v(iii)(b1)} = m_{v(ii)(b1)} x_{(iii)(b1)} = 0.0204008 \text{ kg/s}$$

Properties of the vapor and condensate at (iii)

Density of vapor $\rho_{v(iii)(b1)} = \rho_v(T_{v(iii)(b1)}) = 0.14296 \text{ kg/m}^3$

Density of condensate $\rho_{c(iii)(b1)} = \rho_w(T_{v(iii)(b1)}) = 982.06462 \text{ kg/m}^3$

Dynamic viscosity $\mu_{v(iii)(b1)} = \mu_v(T_{v(iii)(b1)}) = 1.1151 \times 10^{-5} \text{ kg/ms}$

The vapor velocity at (iii)

$$v_{v(iii)(b1)} = \frac{m_{v(iii)(b1)}}{\rho_{v(iii)(b1)} A_{ts}}$$

$$v_{v(iii)(b1)} = 89.92145 \text{ m/s}$$

The Reynolds number of the vapor at (iii)

$$Re_{v(iii)(b1)} = \frac{\rho_{v(iii)(b1)} d_{fh} v_{v(iii)(b1)}}{\mu_{v(iii)(b1)}} = 39194.7112$$

The wall Reynolds number for the frictional pressure drop

$$Re_{w(b1)} = \frac{d_{fh}}{4L_t} (Re_{v(ii)(b1)} - Re_{v(iii)(b1)}) = 22.48177$$

The mean dynamic viscosity and density of the vapor for tube row 1 are

$$\mu_{v(b1)} = 0.5(\mu_{v(ii)(b1)} + \mu_{v(iii)(b1)}) = 1.1139 \times 10^{-5} \text{ kg/ms}$$

and

$$\rho_{v(b1)} = 2(\rho_{v(ii)(b1)}^{-1} + \rho_{v(iii)(b1)}^{-1})^{-1} = 0.14057 \text{ kg/m}^3$$

Coefficients for the frictional pressure drop for duct flow

$$C_{1(b1)} = 1.0649 + 1.0411 \times 10^{-3} Re_{w(b1)} - 2.0110 \times 10^{-7} Re_{w(b1)}^3$$

$$C_{1(b1)} = 1.08602$$

$$C_{2(b1)} = 290.1479 + 59.3153 Re_{w(b1)} + 1.5995 \times 10^{-2} Re_{w(b1)}^3$$

$$C_{2(b1)} = 1805.41125$$

The frictional pressure drop for the current tube row

$$\Delta p_{f(b1)} = \frac{0.3164 \mu_{v(b1)}^2 L_t}{2 \rho_{v(b1)} Re_{v(ii)(b1)} d_{fh}^3} \left[\frac{C_{1(b1)}}{2.75} (Re_{v(ii)(b1)}^{2.75} - Re_{v(iii)(b1)}^{2.75}) + \frac{C_{2(b1)}}{1.75} (Re_{v(ii)(b1)}^{1.75} - Re_{v(iii)(b1)}^{1.75}) \right]$$

$$\Delta p_{f(b1)} = 588.45369 \text{ Pa}$$

The momentum pressure drop over tube row 1

$$\Delta p_{m(b1)} = -\rho_{v(b1)} (v_{v(ii)(b1)}^2 - v_{v(iii)(b1)}^2) = -919.51802 \text{ Pa}$$

The gravitational pressure drop

$$\Delta p_{g(b1)} = -9.81 \rho_{v(b1)} L_t \sin(90 - \theta) = -5.37410 \text{ Pa}$$

The minus indicate pressure gain. The area ratio at the outlet end is the same as the area ratio at the inlet $\sigma_{(ii)(i)} = \sigma_{(iii)(iv)} = 0.5$ therefore the outlet loss coefficient for the flattened tube,

$$K_e = (1 - \sigma_{(iii)(iv)})^2 = 0.25$$

The converged total pressure at (iii) in tube row 1

$$p_{t(iii)(b1)} = p_{t(ii)(b1)} - \Delta p_{f(b1)} - \Delta p_{m(b1)} - \Delta p_{g(b1)} = 22592.4542 \text{ Pa}$$

with the corresponding dynamic pressure

$$p_{d(iii)(b1)} = 0.5 \rho_{v(iii)(b1)} v_{v(iii)(b1)}^2 = 577.9763 \text{ Pa}$$

and the static pressure at the same point

$$p_{v(iii)(b1)} = p_{t(iii)(b1)} - p_{d(iii)(b1)} = 22014.4779 \text{ Pa}$$

The converged total pressure at (iv)

$$p_{t(iv)} = p_{t(iii)(b1)} - 0.5K_e\rho_{v(iii)(b1)}v_{v(iii)(b1)}^2 = 22447.96009 \text{ Pa}$$

After assuming uniform velocity in the header at point (iv) and a flow area of $A_{(iv)} = 1.305 \text{ m}^2$ normal to the flow direction, the dynamic pressure is calculated with the total vapor mass flow rate in the header as $m_{v(iv)} = 17.7916 \text{ kg/s}$ and the density as $\rho_{v(iv)} = \rho_v(T_{v(iv)}) = 0.145542 \text{ kg/m}^3$.

$$p_{d(iv)} = 0.5\rho_{v(iv)}\left(\frac{m_{v(iv)}}{\rho_{v(iv)}A_{(iv)}n_b}\right)^2 = 9.97726 \text{ Pa}$$

The static pressure at (iv) from which the temperature is calculated,

$$p_{v(iv)} = p_{t(iv)} - p_{d(iv)} = 22437.9828 \text{ Pa}$$

By following exactly the same procedure for the second tube row, the pressure and temperature at points (i) to (iv) are calculated and tabulated in Table B.1.

Table B.1: Converged static pressures and temperatures for the vapor of tube row 2

Point	Pressure [Pa]	Temperature [°C]
(i)	19925.1161	60
(ii)	21504.0713	61.6482
(iii)	22100.6328	62.2478
(iv)	22437.9828	62.5809

The amount of condensate removed at (iv)

$$m_{c(iv)} = m_{c(b1)} + m_{c(b2)} = 5.42033 \text{ kg/s}$$

B.3.2 The second stage (bare tube) section

The pressure drop calculation for the second stage tube bundles is almost exactly the same as the analysis for the flattened tubes of the first stage bundles. The relation for the contraction coefficient and the coefficients C_1 and C_2 for the frictional pressure drop are the main difference, since the second stage bundle consists of round tubes.

Figure B.4 shows the second stage tube bundle with all the relevant points where the steam pressure and temperature are determined. The vapor entering the second stage tube bundle

$$m_{v(iv)} = m_{ctb} = m_{vtot} - m_{c(iv)} = 17.7916 \text{ kg/s}$$

The contraction ratio for round tubes with an area ratio $\sigma_{tb} = 0.5$ is the same for all the passes and was also used by Owen (2013)

$$\sigma_{ctb} = 0.61375 + 0.13318\sigma_{tb} - 0.26095\sigma_{tb}^2 + 0.511146\sigma_{tb}^3$$

$$\sigma_{ctb} = 0.679035$$

The inlet loss coefficient due to the contraction

$$K_{ctb} = (1 - \sigma_{ctb}^{-1})^2 = 0.223425$$

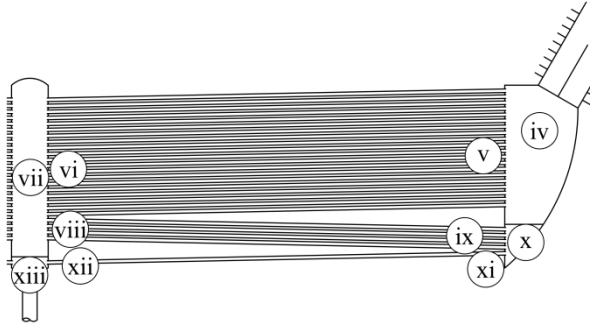


Figure B.4: Second stage steam-side pressure drop

The analysis for pass 1 of the bare tube bundle

The mass flow rate in one tube for the current pass

$$m_{v(v)(p1)} = \frac{m_{v(iv)}}{n_b n_{tr} n_{hr1}}$$

$$m_{v(v)(p1)} = 1.4826 \times 10^{-3} \text{ kg/s}$$

The saturated vapor temperature at (v) is calculated with the converged static pressure at (v)

$$T_{v(v)(p1)} = T_s(p_{v(v)(p1)}) = 62.3516 \text{ }^\circ\text{C}$$

Properties of the vapor at (v)

Density $\rho_{v(v)(p1)} = \rho_v(T_{v(v)(p1)}) = 0.1441 \text{ kg/m}^3$

Dynamic viscosity $\mu_{v(v)(p1)} = \mu_v(T_{v(v)(p1)}) = 1.1157 \times 10^{-5} \text{ kg/ms}$

The inlet velocity at (v)

$$v_{v(v)(p1)} = \frac{m_{v(v)(p1)}}{\rho_{v(v)(p1)} A_{tbts}}$$

$$v_{v(v)(p1)} = 52.4682 \text{ m/s}$$

The total pressure at (v)

$$p_{t(v)(p1)} = p_{t(iv)} - 0.5K_{ctb}\rho_{v(v)(p1)}v_{v(v)(p1)}^2 = 22403.6374 \text{ Pa}$$

The dynamic pressure at (v)

$$p_{d(v)(p1)} = 0.5\rho_{v(v)(p1)}v_{v(v)(p1)}^2 = 198.3789 \text{ Pa}$$

The static pressure at (v)

$$p_{v(v)(p1)} = p_{t(v)(p1)} - p_{d(v)(p1)} = 22205.2585 \text{ Pa}$$

The converged temperature at (vi) calculated from the static pressure at this point

$$T_{v(vi)(p1)} = T_s(p_{v(vi)(p1)}) = 62.5026 \text{ }^\circ\text{C}$$

The enthalpy of the condensate at (vi)

$$i_{c(vi)(p1)} = c_{pw} \left(\frac{T_{v(vi)(p1)}}{2} + 273.15 \right) T_{v(vi)(p1)}$$

$$i_{c(vi)(p1)} = 261143.5539 \text{ J/kg}$$

The enthalpy of the vapor at (v) and (vi) is respectively

$$i_{v(v)(p1)} = i_g(T_{v(v)(p1)}) = 2619447.4356 \text{ J/kg}$$

and

$$i_{v(vi)(p1)} = i_g(T_{v(vi)(p1)}) = 2619737.5820 \text{ J/kg}$$

The heat transfer for the current pass is needed to determine the quality at the end of the pass for the pressure drop calculation. This is simply done by multiplying the total heat transfer by the number of tube rows for the current pass and dividing it by the total number of tube rows of the bundle. This yields the fraction of heat transfer for the current pass. Thus,

$$x_{(vi)(p1)} = \frac{i_{v(v)(p1)} - \frac{Q_{atb}n_{hr1}}{m_{v(iv)}n_{tbr}} - i_{c(vi)(p1)}}{i_{v(vi)(p1)} - i_{c(vi)(p1)}}$$

$$x_{(vi)(p1)} = 0.20187$$

The Reynolds number of the vapor at (v)

$$Re_{v(v)(p1)} = \frac{\rho_{v(v)(p1)} d_i v_{v(v)(p1)}}{\mu_{v(v)(p1)}} = 10708.3706$$

The mass flow rate of the vapor at (vi)

$$m_{v(vi)(p1)} = m_{v(v)(p1)} x_{(vi)(p1)} = 2.9930 \times 10^{-4} \text{ kg/s}$$

This is also the amount of steam that will enter the second pass, since all the condensate is extracted at the end of each pass. Therefore the quality of steam at the start of each consecutive pass is 100%.

Properties of the vapor and condensate at (vi)

Density of vapor	$\rho_{v(vi)(p1)} = \rho_v(T_{v(vi)(p1)}) = 0.1451 \text{ kg/m}^3$
Density of condensate	$\rho_{c(vi)(p1)} = \rho_w(T_{v(vi)(p1)}) = 981.8805 \text{ kg/m}^3$
Dynamic viscosity	$\mu_{v(vi)(p1)} = \mu_v(T_{v(vi)(p1)}) = 1.1162 \times 10^{-5} \text{ kg/ms}$

The vapor velocity at (vi)

$$v_{v(vi)(p1)} = \frac{m_{v(vi)(p1)}}{\rho_{v(vi)(p1)} A_{tbts}}$$

$$v_{v(vi)(p1)} = 10.5236 \text{ m/s}$$

The Reynolds number of the vapor at (vi)

$$Re_{v(vi)(p1)} = \frac{\rho_{v(vi)(p1)} d_i v_{v(vi)(p1)}}{\mu_{v(vi)(p1)}} = 2160.7620$$

The wall Reynolds number for the frictional pressure drop

$$Re_{w(p1)} = \frac{d_i}{4L_{tb}} (Re_{v(v)(p1)} - Re_{v(vi)(p1)}) = 13.5052$$

The mean dynamic viscosity and density of the vapor for pass 1 of the tube bundle are

$$\mu_{v(p1)} = 0.5(\mu_{v(v)(p1)} + \mu_{v(vi)(p1)}) = 1.1160 \times 10^{-5} \text{ kg/ms}$$

and

$$\rho_{v(p1)} = 2(\rho_{v(v)(p1)}^{-1} + \rho_{v(vi)(p1)}^{-1})^{-1} = 0.14459 \text{ kg/m}^3$$

Coefficients for the frictional pressure drop for pipe flow

$$C_{1(p1)} = 1.0046 + 1.719 \times 10^{-3} Re_{w(p1)} - 9.7746 \times 10^{-6} Re_{w(p1)}^2$$

$$C_{1(p1)} = 1.0260$$

$$C_{2(p1)} = 574.3115 + 24.2891 Re_{w(p1)} + 1.8515 Re_{w(p1)}^2$$

$$C_{2(p1)} = 1240.0381$$

The frictional pressure drop for the current pass

$$\Delta p_{f(p1)} = \frac{0.3164 \mu_v^2(p1) L_{tb}}{2 \rho_v(p1) Re_{v(v)(p1)} d_i^3} \left[\frac{C_{1(p1)}}{2.75} (Re_{v(v)(p1)}^{2.75} - Re_{v(vi)(p1)}^{2.75}) \right. \\ \left. + \frac{C_{2(p1)}}{1.75} (Re_{v(v)(p1)}^{1.75} - Re_{v(vi)(p1)}^{1.75}) \right]$$

$$\Delta p_{f(p1)} = 419.3031 \text{ Pa}$$

The momentum pressure drop over the tube

$$\Delta p_{m(p1)} = -\rho_v(p1) (v_{v(v)(p1)}^2 - v_{v(vi)(p1)}^2) = -382.0254 \text{ Pa}$$

The gravitational pressure drop over the second stage tube bundle is zero because the tubes are essentially horizontal. The area ratio at the outlet end of the tube bundle is the same as at the inlet. Therefore the outlet loss coefficient of the round tube,

$$K_e = (1 - \sigma_{tb})^2 = 0.25$$

The converged total pressure at (vi)

$$p_{t(vi)(p1)} = p_{t(v)(p1)} - \Delta p_{f(p1)} - \Delta p_{m(p1)} = 22366.3596 \text{ Pa}$$

The dynamic pressure at (vi)

$$p_{d(vi)(p1)} = 0.5 \rho_v(vi)(p1) v_{v(vi)(p1)}^2 = 8.0322 \text{ Pa}$$

The static pressure at (vi)

$$p_{v(vi)(p1)} = p_{t(vi)(p1)} - p_{d(vi)(p1)} = 22358.3274 \text{ Pa}$$

The converged total pressure at (vii) in the central header after the first pass

$$p_{t(vii)} = p_{t(vi)(p1)} - 0.5 K_e \rho_v(vi)(p1) v_{v(vi)(p1)}^2 = 22364.3516 \text{ Pa}$$

With an area of $A_h = 0.58 \text{ m}^2$ normal to the flow in the header, the density calculated as $\rho_v(vii) = \rho_v(T_{v(vii)}) = 0.14508 \text{ kg/m}^3$ and the vapor mass flow rate determined as $m_{v(vii)} = 3.5916 \text{ kg/s}$, the dynamic pressure can be calculated at (vii)

$$p_{d(vii)} = 0.5\rho_{v(vii)} \left(\frac{m_{v(vii)}}{\rho_{v(vii)}A_h n_b} \right)^2 = 2.0649 \text{ Pa}$$

The static pressure at (vii)

$$p_{v(vii)} = p_{t(vii)} - p_{d(vii)} = 22362.2867 \text{ Pa}$$

The above procedure for the second stage tube bundle is repeated for the second and third pass to obtain the pressures and temperatures shown in Table B.2.

Table B.2: Converged vapor temperature and static pressure at various points in the second stage tube bundle

Point	Pressure [Pa]	Temperature [°C]
(iv)	22437.9828	62.5809
(v)	22205.2585	62.3516
(vi)	22358.3274	62.5026
(vii)	22362.2867	62.5065
(viii)	22116.1556	62.2633
(ix)	22273.2588	62.4188
(x)	22279.7903	62.4252
(xi)	22105.8105	62.2530
(xii)	22203.3489	62.3497
(xiii)	22203.6797	62.3500

The average vapor temperature, T_{vtb} , is a weighted average of the temperatures of the vapor for each pass and is expressed as

$$T_{vtb} = \frac{n_{hr1}T_{v(p1)} + n_{hr2}T_{v(p2)} + n_{hr3}T_{v(p3)}}{n_{tbr}}$$

$$T_{vtb} = 62.4083 \text{ °C}$$

with $T_{v(p1)} = (T_{v(v)} + T_{v(vi)})/2$, $T_{v(p2)} = (T_{v(viii)} + T_{v(ix)})/2$ and $T_{v(p3)} = (T_{v(xi)} + T_{v(xii)})/2$. This temperature is used to calculate the thermo-physical properties of the vapor and condensate for the thermal analysis of the second stage tube bundle in Section B.1.2.

Table B.3 is a summary of all the important parameters for the pressure drop calculation. As previously stated, all the condensate is removed at the end of each pass and only the remaining vapor continues to the next pass. Just for the sake of clarity the frictional and momentum pressure drop for the three passes, along with the fraction of the total heat transfer for each of the three passes are also shown.

Table B.3: Summary of the important parameters for the second stage tube bundle under wet operation

	Pass 1	Pass 2	Pass 3
Q_{atbp} [W]	33486900.682	6697380.136	1674345.034
m_v [kg/s]	17.792	3.592	0.752
m_c [kg/s]	14.200	2.840	0.752
x	0.202	0.209	0.056
Δp_f [Pa]	419.303	426.425	328.573
Δp_m [Pa]	-382.025	-389.488	-284.271

B.4 Evaluation of the thermal performance of the HDWD with dry operation of the second stage bundles

This section only details the differences in the analysis of the HDWD under dry compared to wet operation, which are the thermal analysis and the draft equation of the second stage section. The converged parameters of the sections which are identical to the analysis of wet operation are quoted for completeness. When there is referred to parameters such as temperatures, it is the calculated or quoted values of the current analysis of the dry operation of the HDWD.

The following parameters have been obtained by following the procedure defined in Section B.1.1 to determine the thermal performance of the finned tube bundles section.

Converged iteration parameters for the thermal analysis of the finned tube bundles

Air mass flow rate through the first stage	$m_{av67} = 414.222$ kg/s
Mean outlet air temperature after the first tube row of the finned tube bundle	$T_{ao(b1)} = 303.798$ K
Mean bundle outlet temperature	$T_{a7} = 318.084$ K
Air pressure at the inlet of the heat exchanger	$p_{a6} = 84363.6140$ Pa

B.4.1 Thermal analysis of the section stage (bare tube) section

Converged iteration parameters for the bare tube bundles

Air vapor mass flow at the inlet of the tube bundle	$m_{av34} = 168.587$ kg/s
Steam condensed in eight bundles of one dephlegmator	$m_{ctb} = 2.1274$ kg/s
The inner wall temperature of the tubes	$T_{wi} = 60.1745$ °C
The vapor temperature	$T_{vtb} = 60.26116$ °C

Saturated outlet air temperature

$$T_{a4} = 44.7952 \text{ }^\circ\text{C}$$

The thermo-physical properties of the air are determined at the mean of the in- and outlet temperatures over the bundle,

$$T_{a34} = 0.5(T_{a3} + T_{a4}) = 303.2598 \text{ K}$$

The thermo-physical properties of air at the evaluation temperature

Density	$\rho_{avm34} = \rho_{av}(w_3, p_{a3}, T_{a34}) = 0.96566 \text{ kg/m}^3$
Specific heat	$c_{pavm34} = c_{pav}(T_{a34}, w_3) = 1013.1203 \text{ J/kgK}$
Dynamic viscosity	$\mu_{avm34} = \mu_{av}(T_{a34}, w_3) = 1.8545 \times 10^{-5} \text{ kg/ms}$
Thermal conductivity	$k_{avm34} = k_{av}(T_{a34}, w_3) = 0.0264027 \text{ W/mK}$

The corresponding Prandtl number

$$Pr_{avm34} = \frac{\mu_{avm34} c_{pavm34}}{k_{avm34}} = 0.711602$$

The outlet enthalpy of the air above the tube bundle

$$i_{ma4} = i_{ma}(T_{a4}, w_3) = 62948.8641 \text{ J/kg}$$

The heat transferred to the air

$$Q_{atb} = m_{av34} c_{pavm34} (T_{a4} - T_{a3}) = 5016471.527 \text{ W}$$

The thermo-physical properties of air at the vapor temperature

Specific heat	$c_{pavs} = c_{pav}(T_{vtb}, w_3) = 1013.1212 \text{ J/kgK}$
Dynamic viscosity	$\mu_{avs} = \mu_{av}(T_{vtb}, w_3) = 1.9902 \times 10^{-5} \text{ kg/ms}$
Thermal conductivity	$k_{avs} = k_{av}(T_{vtb}, w_3) = 0.028697 \text{ W/mK}$

The corresponding Prandtl number

$$Pr_{avs} = \frac{\mu_{avs} c_{pavs}}{k_{avs}} = 0.702632$$

Mean velocity of air through the tube bundle

$$v_{am34} = \frac{m_{av34}}{n_b A_{tb} f_r \rho_{avm34}} = 3.04257 \text{ m/s}$$

The diagonal pitch of the tubes

$$P_d = \sqrt{\left(\frac{P_t}{2}\right)^2 + P_l^2} = 0.038 \text{ m}$$

The maximum velocity of air through the bundle based on the minimum flow area

$$v_{max} = \frac{v_{am34} P_t}{P_t - d_o} = 6.085 \text{ m/s}$$

The Reynolds number based on the maximum air velocity

$$Re_D = \frac{\rho_{avm34} v_{max} d_o}{\mu_{avm34}} = 6020.3675$$

Zukauskas (1987) proposed Eq. (A.2) to predict the average Nusselt number for a tube bundle

$$Nu_D = 0.35 Re_D^{0.6} Pr_{avm34}^{0.38} \left(\frac{Pr_{avm34}}{Pr_{avs}} \right)^{0.25} \left(\frac{P_t}{P_l} \right)^{0.2} = 58.82514$$

which is valid for $1000 < Re_D < 200000$. The corresponding air-side heat transfer coefficient,

$$h_a = \frac{Nu_D k_{avm34}}{d_o} = 81.74424 \text{ W/m}^2\text{K}$$

The thermo-physical properties of the condensate at the saturated vapor temperature

Density	$\rho_{ctb} = \rho_w(T_{vtb} + 273.15) = 983.0792 \text{ kg/m}^3$
Specific heat	$c_{pctb} = c_{pw} \left(\frac{T_{vtb}}{2} + 273.15 \right) = 4178.541 \text{ J/kgK}$
Dynamic viscosity	$\mu_{ctb} = \mu_w(T_{vtb} + 273.15) = 4.6126 \times 10^{-4} \text{ kg/ms}$
Thermal conductivity	$k_{ctb} = k_w(T_{vtb} + 273.15) = 0.65344 \text{ W/mK}$
Latent heat	$i_{fgtb} = i_{fg}(T_{vtb} + 273.15) = 2357980.951 \text{ J/kg}$

The corresponding Prandtl number

$$Pr_{ctb} = \frac{\mu_{ctb} c_{pctb}}{k_{ctb}} = 2.94961$$

The thermo-physical properties of the vapor at the saturated vapor temperature

Density	$\rho_{vtb} = \rho_v(T_{vtb} + 273.15) = 0.13172 \text{ kg/m}^3$
Specific heat	$c_{pvtb} = c_{pv} \left(\frac{T_{vtb}}{2} + 273.15 \right) = 1889.042 \text{ J/kgK}$
Dynamic viscosity	$\mu_{vtb} = \mu_v(T_{vtb} + 273.15) = 1.10909 \times 10^{-5} \text{ kg/ms}$
Thermal conductivity	$k_{vtb} = k_v(T_{vtb} + 273.15) = 0.021058 \text{ W/mK}$
Vapor pressure	$p_{vtb} = p_v(T_{vtb} + 273.15) = 20167.1878 \text{ Pa}$
Critical pressure	$p_{cr} = 22.09 \times 10^6 \text{ Pa}$

The mass flow rate of the steam condensed in all eight tube bundles of one dephlegmator

$$m_{ctb} = \frac{Q_{atb}}{i_{fgtb}} = 2.12744 \text{ kg/s}$$

The vapor Reynolds number at the inlet of the first pass of the tube bundle,

$$Re_{v(v)} = \frac{m_{ctb} d_i}{n_b n_{tr} n_{hr1} A_{tbts} \mu_{ctb}} = 30.9731$$

The condensation heat transfer coefficient proposed by Chato (1962) for low Reynolds number flows in near horizontal tubes requires an inner wall temperature of the tube. This temperature is solved iteratively and converged at $T_{wi} = 60.1745$ °C. The condensation heat transfer coefficient is only calculated for the first tube pass but used as an average for the whole tube bundle similar to the analysis of Heyns (2008). The method is considered valid, since the vapor temperature varies only by small amounts through the bundle as will be shown later. The condensation heat transfer coefficient is then,

$$h_c = 0.555 \left[\frac{9.8 \rho_{ctb} (\rho_{ctb} - \rho_{vtb}) k_{ctb}^3 i'_{fgtb}}{\mu_{ctb} (T_{vtb} - T_{wi}) d_i} \right]^{0.25}$$

$$h_c = 31106.5976 \text{ W/m}^2\text{K}$$

with $i'_{fgtb} = i_{fgtb} + 0.68 c_{pctb} (T_{vtb} - T_{wi})$. The wall temperature is confirmed with the following formula,

$$T_{wi} = T_{vtb} - \frac{Q_{atb}}{n_b A_i h_c} = 60.1745 \text{ °C}$$

The product of the overall heat transfer coefficient and the outer area of the tube bundle is

$$UA_o = n_b A_o \left[\frac{d_o}{d_i h_c} + \frac{d_o \ln \left(\frac{d_o}{d_i} \right)}{2k_t} + \frac{1}{h_a} \right]^{-1}$$

$$UA_o = 181795.0610 \text{ W/K}$$

The effectiveness of the tube bundle in dry mode

$$e_{tb} = 1 - \exp \left(- \frac{UA_o}{m_{av34} c_{pavm34}} \right) = 0.65506$$

The heat transfer is then

$$Q_{atb} = e_{tb} m_{av34} c_{pavm34} (T_{vtb} - T_{a3}) = 5016471.5271 \text{ W}$$

The outlet air temperature is confirmed at,

$$T_{a4} = T_{a3} + \frac{Q_{atb}}{m_{av34} c_{pavm34}} = 44.7952 \text{ °C}$$

B.4.2 Evaluation of the draft equation for the second stage (bare tube) section

The following parameters are obtained by following the procedures defined in Sections B.2.1 and B.2.3 to determine the air flow through the finned tube section and the mixed section.

Converged iteration parameters for the draft equation

Pressure at point 6	$p_{a6} = 84363.614$ Pa
Pressure at point 4	$p_{a4} = 84231.337$ Pa
Pressure at point 8	$p_{a8} = 84199.989$ Pa
Temperature at point 8	$T_{a8} = 44.8941$ °C

As previously calculated, the pressure at point 3 ($p_{a3} = 84420.169$ Pa) below the collecting troughs is equal to point 2. The converged mass flow rate of air through the tube bundle is $m_{av34} = 168.5869$ kg/s and the corresponding dry air mass flow rate is

$$m_{a34} = \frac{m_{av34}}{1+w_3} = 167.4312 \text{ kg/s}$$

The dry air mass flux through the bundle is

$$G_{a34} = \frac{m_{a34}}{A_{tbfr}n_b} = 2.9179 \text{ kg/s}$$

The relation proposed by Bertrand (2011) for the pressure drop over the collecting troughs during dry operation is defined as

$$\Delta p_{ct} = 1.027 G_{a34}^{2.0015} = 8.7583 \text{ Pa}$$

The film temperature of the air flowing through the tube bank is calculated with the mean temperature over the tube bank and the average vapor temperature.

$$T_f = 0.5(T_{vtb} + T_{a34}) = 318.3355 \text{ K}$$

The corresponding viscosity of air based on this temperature is

$$\mu_{avf} = \mu_{av}(T_f, w_3) = 1.9229 \times 10^{-5} \text{ kg/ms}$$

Gaddis & Gnielinski (1985) defined the following correlation for the turbulent contribution of the loss coefficient of the bundle for non-isothermal conditions during cross flow. This equation is quoted in Eq. (A.9) and is valid for $Re_D > 4000$

$$K_{tb} = \frac{1}{Re_D^{0.25}} \left[2.5 + \frac{1.2}{(a - 0.85)^{1.08}} + 0.4 \left(\frac{b}{a} - 1 \right)^3 - 0.01 \left(\frac{a}{b} - 1 \right)^3 \right] \left(\frac{\mu_{avf}}{\mu_{avm34}} \right)^{0.14}$$

$$K_{tb} = 0.4029$$

with $a = P_t/d_o = 2$ and $b = P_l/d_o = 1.732$. The resulting pressure drop over the tube bundle by implementing Eq. (A.4) is

$$\Delta p_{tb} = 0.5 K_{tb} n_{tbr} \rho_{avm34} v_{max}^2 = 180.0746 \text{ Pa}$$

The density and viscosity at point 4 above the tube bundle with a corresponding pressure of $p_{a4} = 84231.3365 \text{ Pa}$ are respectively,

$$\rho_{av4} = \rho_{av}(w_3, p_{a4}, T_{a4}) = 0.918994 \text{ kg/m}^3$$

and

$$\mu_{av4} = \mu_{av}(T_{a4}, w_3) = 1.92112 \times 10^{-5} \text{ kg/ms}$$

The characteristic flow parameter for the drift eliminators with $A_{frde} = 5.945 \text{ m}^2$ is

$$Ry_{de} = \frac{m_{av34}}{n_b A_{frde} \mu_{av4}} = 184512.8206 \text{ m}^{-1}$$

The loss coefficient for the drift eliminators as proposed by Kröger (2004)

$$K_{de} = 27.4892 Ry_{de}^{-0.14247} = 4.8855$$

The pressure drop over the drift eliminators

$$\Delta p_{de} = K_{de} \left(\frac{m_{av34}}{A_{frde} n_b} \right)^2 \frac{1}{2 \rho_{av4}} = 33.3989 \text{ Pa}$$

The kinetic energy recovery at the top of the drift eliminators

$$\Delta p_{ke} = -K_{rec} \left(\frac{m_{av34}}{A_{frde} n_b} \right)^2 \frac{1}{2 \rho_{av4}} = -2.0509 \text{ Pa}$$

The confirmed pressure at the top of the tube bundle

$$p_{a4} = p_{a3} - \Delta p_{tb} - \Delta p_{ct} = 84231.3365 \text{ Pa}$$

The pressure at point 8 through the tube bundle section

$$p_{a8} = p_{a4} - \Delta p_{de} - \Delta p_{ke} = 84199.9885 \text{ Pa}$$

This concludes the analysis to determine the draft through the second stage (bare tube) section. The same resistances are applicable for the draft equations through the finned tube section as well as the fan.

By repeating the analysis of the steam-side pressure drop as represented in Section B.3 for the dry operation of the dephlegmator, the following vapor temperatures and pressures are obtained as summarized in Tables B.4 and B.5. Table B.4 is a summary of the parameters of the first stage (finned tube) section, while Table B.5 is a summary of the parameters for the second stage (bare tube) section.

Converged static pressures and vapor temperatures at the positions indicated in Figures B.3 and B4 for the dry operation of the dephlegmator

Table B.4: Converged static pressures and temperatures of the vapor of tube row 1 and 2

Point	Pressure [Pa]		Temperature [°C]	
	Tube row 1	Tube row 2	Tube row 1	Tube row 2
(i)	19925.1161	19925.1161	60	60
(ii)	20036.1503	20090.4571	60.1105	60.1691
(iii)	20176.3615	20182.7048	60.2615	60.2683
(iv)	20185.8615	20185.8615	60.2717	60.2717

Table B.5: Converged vapor temperatures and static pressures at various points in the second stage tube bundle

Point	Pressure [Pa]	Temperature [°C]
(v)	20182.2230	60.2677
(vi)	20175.0838	60.2601
(vii)	20175.1461	60.2602
(viii)	20171.3075	60.2560
(ix)	20164.1430	60.2483
(x)	20164.2458	60.2485
(xi)	20161.5271	60.2455
(xii)	20154.8377	60.2383
(xiii)	20154.8431	60.2384

Again a summary of all the important parameters, as quoted for the wet operation of the tube bundle, are quoted for the dry operation in Table B.6. This is the results of the steam-side pressure drop calculation.

Table B.6: Summary of the important parameters for the second stage tube bundle under dry operation

	Pass 1	Pass 2	Pass 3
Q_{atbp} [W]	4013177.222	802635.444	200658.861
m_v [kg/s]	2.127	0.430	0.090
m_c [kg/s]	1.698	0.340	0.090
x	0.202	0.210	0.057
Δp_f [Pa]	16.067	16.239	13.337
Δp_m [Pa]	-5.951	-6.049	-4.432

Appendix C: Calibration

Various instruments used to measure the necessary parameters for the experiment were calibrated beforehand and is detailed in the subsections below.

C.1 Thermocouples

The calibration of the Type T (copper-constantan) thermocouples entailed using a FLUKE 9142 Field Metrology Well with a calibrated reference Platinum Resistance Temperature Detector (PRTD) as illustrated Figure C.1.

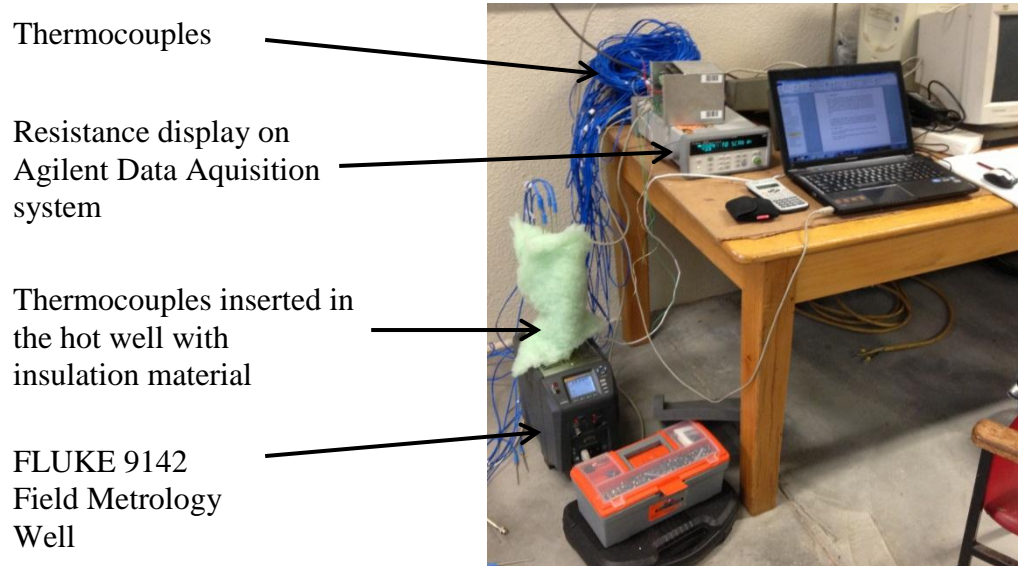


Figure C.1: Photo of the calibration of the thermocouples

The calibration procedure is discussed for four thermocouples, because the hot well of the FLUKE calibrator has a capacity for four thermocouples, but the procedure was repeated for all 45 thermocouples. The error in degrees Celsius before calibration between the thermocouples and the reference thermocouple is shown in the Table C.1 for three verification temperatures indicating the need for calibration:

Table C.1: Error of the thermocouples with regard to the reference thermocouple prior to calibration

Verification temperature [°C]	<i>Error = T_{ref} - T_{raw} [°C]</i>			
	<i>T_{ao1}</i>	<i>T_{wbo1}</i>	<i>T_{ao2}</i>	<i>T_{wbo2}</i>
23	0.4943	0.6199	0.5958	0.5035
35	0.4177	0.6164	0.5363	0.4720
47	0.3660	0.6241	0.5021	0.4574

Procedure:

1. Six temperatures: 10, 20, 30, 40, 50 and 60 °C are selected as set points that are representative of the temperature range expected during the experiments
2. Four thermocouples are inserted in the hot well of the calibrator along with the reference PRTD
3. Allow 30 minutes with the calibrator set at 25 °C and the Agilent data acquisition system on, to cancel any temperature effects in the electronics
4. Start the Agilent data acquisition system and log the temperatures every 5 seconds
5. Input the set point temperature into the calibrator and allow twelve minutes for the calibrator to reach the set point. This is to ensure a uniform temperature of the metal insert in the hot well.
6. Document the kOhm output of the PRTD
7. Steps 5 and 6 are repeated until all the set points in the selected range are logged.
8. The Agilent data acquisition system is stopped and all electronics are switched off after completion of the calibration

An average of 50 data points is used for each set point to represent the thermocouple reading. Table C.2 shows the reference temperature from the PRTD and the four thermocouple readings at the six set points.

Table C.2: Six points selected with the readings from the reference and ordinary thermocouples

Set point [°C]	kOhm reading [kΩ]	Reference Temperature [°C]	T_{ao1} [°C]	T_{wbo1} [°C]	T_{ao2} [°C]	T_{wbo2} [°C]
10	103.91	10.0350	9.5133	9.4489	9.4200	9.5030
20	107.8	20.0043	19.5167	19.4112	19.4007	19.4624
30	111.67	29.9559	29.5306	29.3933	29.4038	29.4489
40	115.54	39.9409	39.5608	39.3969	39.4193	39.4600
50	119.4	49.9335	49.5976	49.4116	49.4492	49.4840
60	123.24	59.9072	59.5923	59.3781	59.4304	59.4622

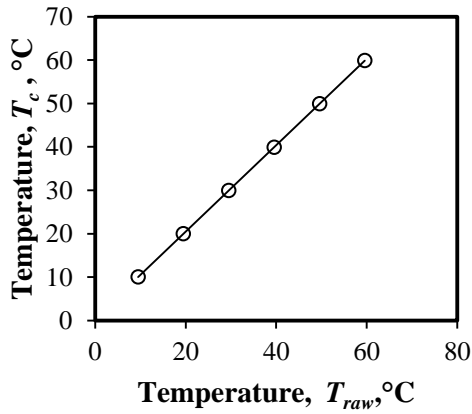
The thermocouple readings are plotted against the reference temperatures as illustrated in Figure C.2 to obtain the linear curve fits which are used as the calibration curves. These calibration curves are quoted below

$$T_{ao1(c)} = 0.99562649T_{ao1(raw)} + 0.56201942$$

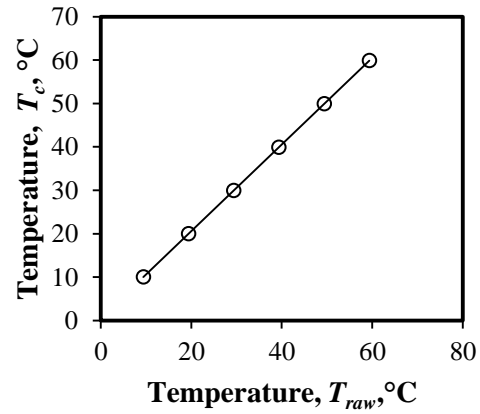
$$T_{wbo1(c)} = 0.99852116T_{wbo1(raw)} + 0.60701063$$

$$T_{ao2(c)} = 0.99691846T_{ao2(raw)} + 0.64831139$$

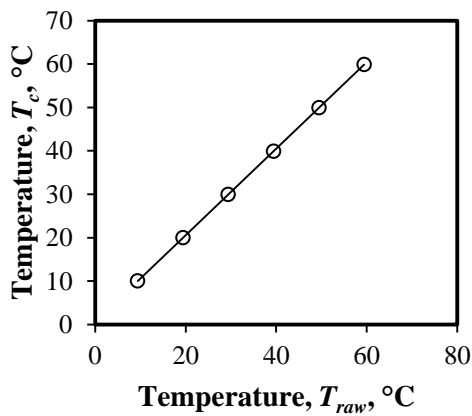
$$T_{wbo2(c)} = 0.99789187T_{wbo2(raw)} + 0.56539092$$



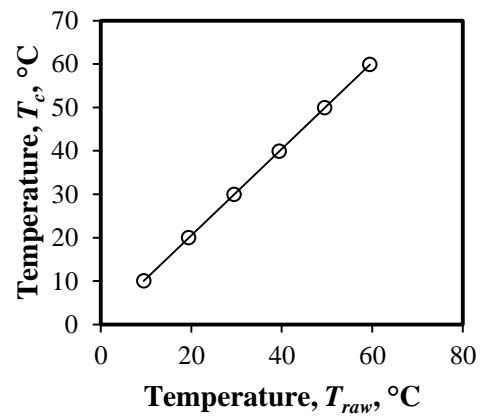
(a) The curve fit for T_{ao1}



(b) The curve fit for T_{wbo1}



(c) The curve fit for T_{ao2}



(d) The curve fit for T_{wbo2}

Figure C.2: The curve fits for four thermocouples

Verification:

Three temperatures: 23, 35 and 47 °C are selected as set points for the verification temperatures. Steps 2 – 8 of the calibration procedure are repeated. An average of 50 data points is again used for each set point to represent the thermocouple reading. The obtained calibration curve fit for each thermocouple is used to predict the reference thermocouple temperature. Table C.3 shows the difference between the calibrated thermocouple readings and the reference PRTD temperature at the three set points. This error is sufficiently low to confirm a valid calibration.

Table C.3: The error between the calibrated thermocouple temperatures and the reference thermocouple temperature

Set point [°C]	kOhm reading [kΩ]	Reference Temperature [°C]	<i>Error = T_{ref} - T_c</i>			
			<i>T_{ao1}</i> [°C]	<i>T_{wbo1}</i> [°C]	<i>T_{ao2}</i> [°C]	<i>T_{wbo2}</i> [°C]
23	108.973	23.0171	0.0307	0.0457	0.0162	-0.0148
35	113.616	34.9726	0.0069	0.0606	-0.0056	-0.0207
47	118.245	46.9400	0.0075	0.0855	-0.0029	-0.0099

C.2 Pressure transducers

The calibration of the pressure transducers for the air-side pressure drop over the flow nozzles and the tube bundle entailed coupling the Betz micromanometer, as illustrated in Figure C.3, to the three pressure transducers of Figure 4.9 respectively and following the procedure below.



Figure C.3: Betz micromanometer

Procedure:

1. Switch on the light of the Betz micromanometer and blow on the positive port to remove all the water droplets from the glass floating element inside
2. Zero the Betz micromanometer by turning the screw on top
3. Connect the negative port of the Betz micromanometer to the negative port of the pressure transducer
4. Blow on the positive port of the Betz micromanometer to obtain a mmH₂O reading
5. Seal the pipe with a finger and take down the readings on the pressure transducer and the Betz micromanometer after stabilization
6. Remove the finger to let some air escape

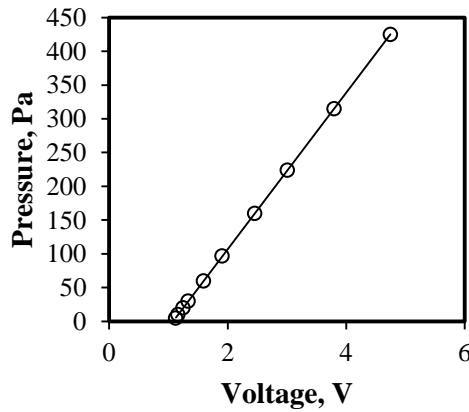
7. Repeat steps 5 and 6 until enough data points are obtained for a curve fit

Figure C.4 shows the results of calibration consisting of the data points and the linear curve fits indicated below,

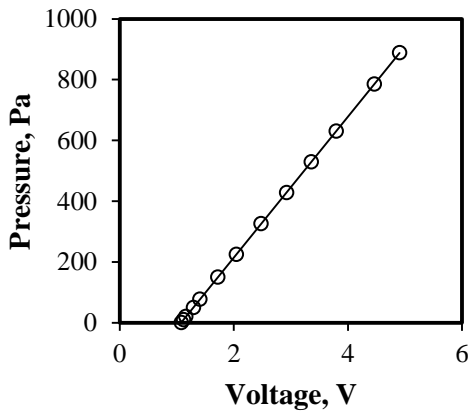
$$P_A = 231.5065V - 248.7281$$

$$P_B = 115.7668V - 124.6738$$

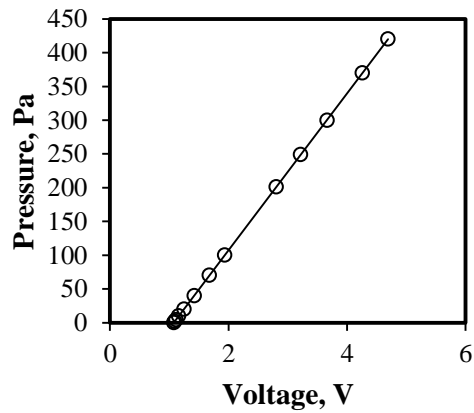
$$P_C = 116.1259V - 124.7574$$



(a) Pressure transducer (B)



(b) Pressure transducer (A)



(c) Pressure transducer (C)

Figure C.4: Plots of the calibration curves for the three pressure transducers in Figure 4.9

C.3 Venturi flow meter

Figure C.5 is an illustration of the Venturi calibration setup that consists of a pump, Venturi, two control valves, a tank, a sump, pressure transducer, mercury manometer and the Agilent data acquisition system. The tank in the setup has a

lower and a higher mark between which the volume of the tank is known. The aim is to determine the Venturi discharge coefficient in order to determine the volumetric flow rate of the deluge water by measuring the pressure drop over the contraction of the Venturi. The pressure drop is measured with a pressure transducer with a 4 – 20 mA output that needs to be calibrated. The calibration and the discharge coefficient determination occur in parallel by following the subsequent procedure.

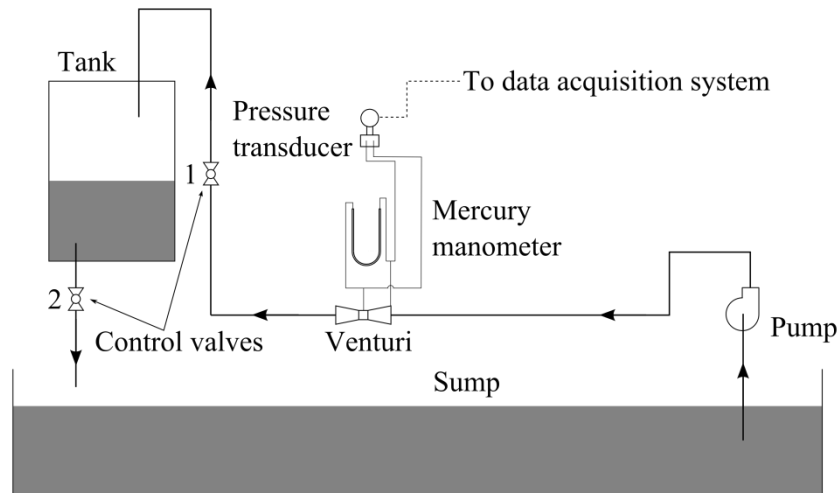


Figure C.5: Venturi calibration setup

Procedure to determine the discharge coefficient of the Venturi and calibrate the pressure transducer:

1. Start the pump with all valves fully open
2. Ensure the pressure drop over the Venturi flow meter can be measured with the mercury manometer and the pressure transducer in parallel
3. Set up and start the data acquisition system to log the 4 – 20 mA output signal from the pressure transducer every three seconds
4. Close the control valve 2 of the tank to commence filling
5. Start the time when the water level reaches the lower mark of the tank
6. Record the manometer reading for this particular valve setting
7. Stop the time when the water level reaches the higher mark
8. Open control valve 2 to drain the tank
9. Record the time for this particular valve setting
10. Regulate the flow rate to the tank by adjusting control valve 1
11. Repeat steps 4 – 10 to obtain enough points across the flow rate range of the pump
12. Switch off all associated equipment when enough data points are obtained

The output signal from the pressure transducer is correlated with the pressure obtained from the mercury manometer and shown in Figure C.6.

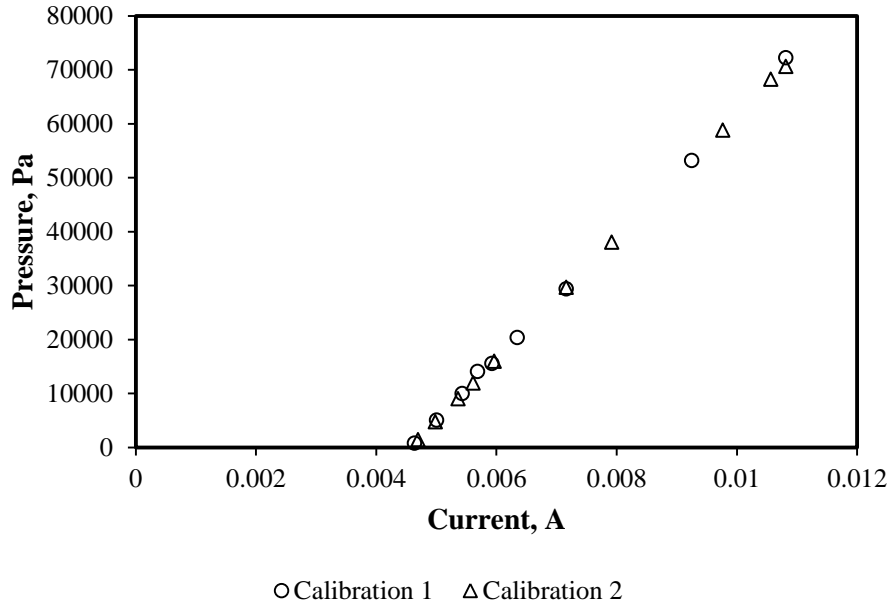


Figure C.6: Pressure transducer calibration

The curve fit formulae of the two calibration tests of the pressure transducer is the following:

$$P_{c1} = 11459573.2658I - 52199.9130$$

$$P_{c2} = 11319354.6878I - 51588.7434$$

The formulae has a $R=0.9995$ and $R=1.0000$ respectively. The theoretical volumetric flow rate is calculated with Bernoulli and manipulating the equation as follows (1 refers to the upstream pressure point and 2 the pressure point in the contraction),

$$\frac{P_1}{\rho g} + \frac{v_1^2}{2g} = \frac{P_2}{\rho g} + \frac{v_2^2}{2g}$$

$$2g \left(\frac{P_1 - P_2}{\rho g} + \frac{v_1^2}{2g} \right) = v_2^2$$

$$2 \left(\frac{P_1 - P_2}{\rho} \right) + v_1^2 = v_2^2$$

By substituting $v_1 = v_2 A_2 / A_1$ into the above equation and multiplying the equation with A_2^2 the following can be obtained,

$$2A_2^2 \left(\frac{P_1 - P_2}{\rho} \right) + A_2^2 \left(\frac{v_2 A_2}{A_1} \right)^2 = V^2$$

$$2A_2^2 \left(\frac{P_1 - P_2}{\rho} \right) = V^2 \left(1 + \frac{A_2^2}{A_1^2} \right)$$

$$2A_2^2 \left(\frac{P_1 - P_2}{\rho \left(1 + \frac{d_2^4}{d_1^4} \right)} \right) = V^2$$

$$V = A_2 \sqrt{\frac{2(P_1 - P_2)}{\rho \left(1 + \left(\frac{d_2}{d_1} \right)^4 \right)}}$$

The discharge coefficient, C_d , of the Venturi is a correction factor that accounts for frictional and the vena contracta losses that adjusts the theoretical flow rate to the actual measured flow rate and is expressed as,

$$V_{actual} = C_d V_{theoretical}$$

The discharge coefficient ranges from 0.9515 to 1.0267 for this particular experiment but should however be smaller than 1 because the actual flow measuring instrument has losses named earlier that cause the actual flow to be lower than the ideal theoretical case. This error suggests that some dimensional measuring errors of the Venturi or some slight timing errors in the filling of the tank could have been the cause for this.

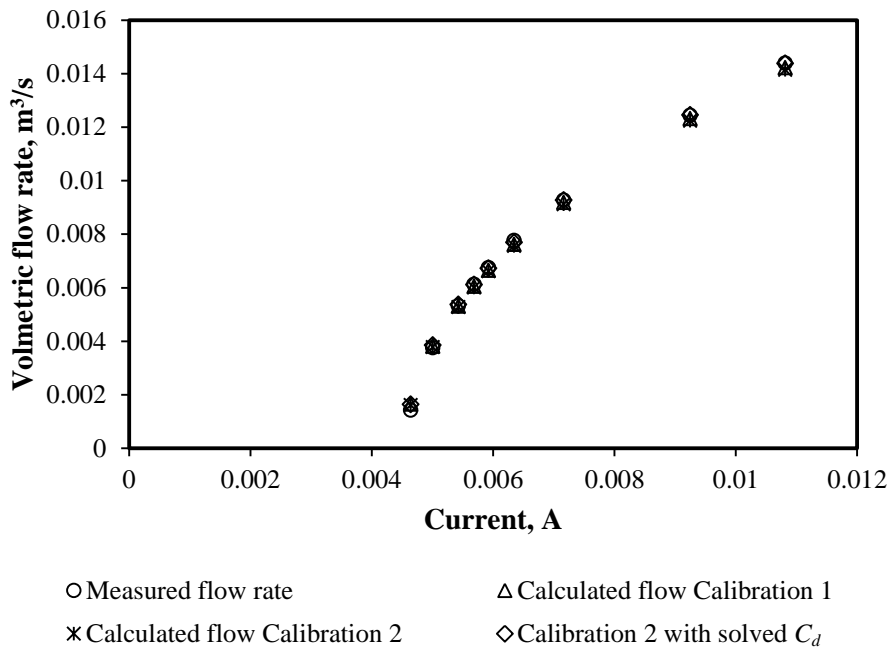


Figure C.7: Experimental and calculated deluge water flow rate comparison

Figure C.7 shows both the calibration curve fits for the pressure transducer implemented to compare the calculated flow rate. In Calibration 1 and 2 the arithmetic average discharge coefficient of all the discharge coefficients for each data point is used to determine the flow rate. Conversely, in the data set *Calculated flow with solved C_d* , the errors between the measured and the calculated flow rate is minimized to determine the optimal discharge coefficient to accurately predict the flow. This value for the discharge coefficient is 1.0197 and is used in subsequent experiments. The error of the calculated flow rate is on average less than 2.3 % compared to the measured flow rate, except for the lowest flow rate.

C.4 Process water flow meter

Similar to the procedure to calibrate the Venturi flow meter, the process water flow meter as depicted in Figure 4.12 is also calibrated. A tank with a known volume is filled with process water and timed, while the current output from the flow meter is logged during the filling of the tank. The flow meter directly measures the flow rate thus the current output is correlated with the actual calculated volumetric flow rate. The time to fill the tank is recorded at each set flow rate value, along with the value on the display of the process water flow meter for comparison. Two control valves are used during calibration. One is upstream of the tank to set the flow rate, and the other to control the filling and discharge of the tank.

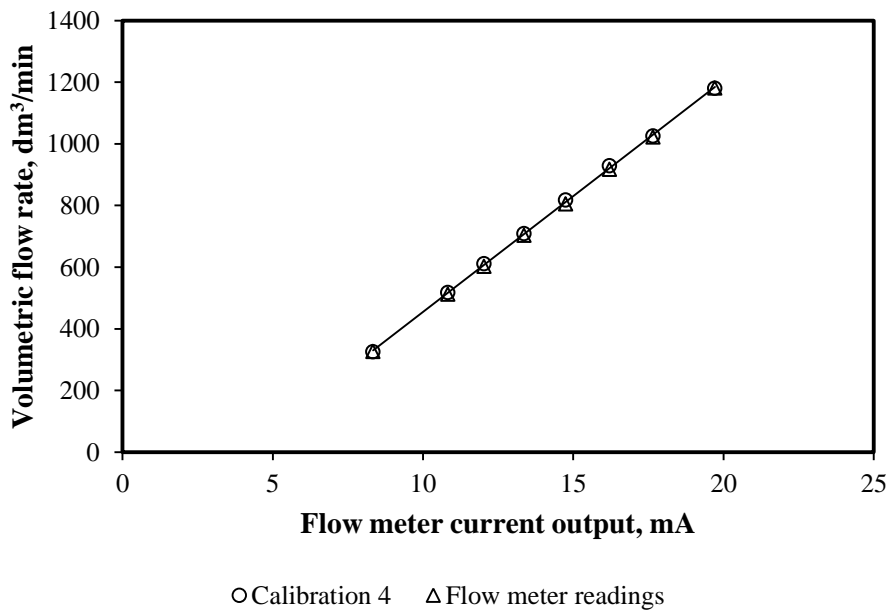


Figure C.8: Calibration results of the process water flow meter

The calculated flow rate and the meter display value are plotted against the current output as shown in Figure C.8. A linear curve is fitted to the calculated volumetric flow rate and the current output to express the calibration curve as,

$$V = 75.111I - 295.72$$